Feasibility Study on the Generalization of the Demise Observation Capsule

P. Fatemi Ghomi

DOC Mission Profile

~700 km

Wakeup Phase

Host Vehicle
Breakup

~100 km

Separation from
the Host Vehicle

Blackout

Re-Entry Phase

Host Vehicle
&
DOC Capsule

Launch
&
Ascent
Phase

Communication
Network Service

DOC
Capsule

~30 km

Breakup
Measurement data

Descent Phase

Launch
Preparation
&
Integration
Phase

Post Impact
Phase

~700 km

TU Delft
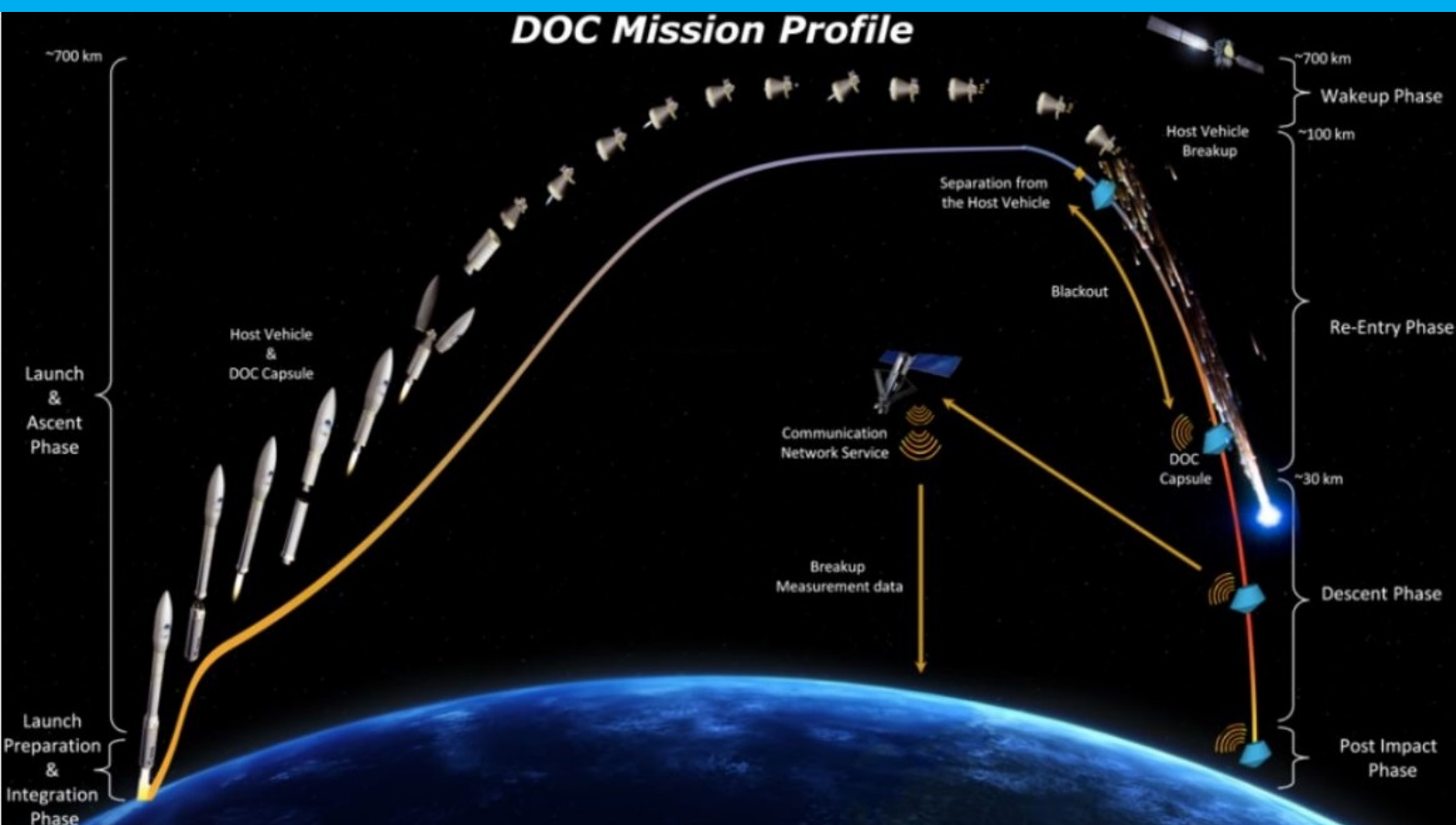
Feasibility Study on the Generalization of the Demise Observation Capsule

by

P. Fatemi Ghomi

to obtain the degree of
Master of Science
in Aerospace Engineering at the Delft University of Technology,
to be defended publicly on Friday May 4, 2018 at 13:30.

Student number:	4023277	
Supervisor:	ir. M. C. Naeije,	TU Delft
	Dr. ir. S. Shroff,	TU Delft
Thesis committee:	Prof. Dr. ir. P. N. A. M. Visser,	TU Delft
	Dr. ir. R. Gardi,	CIRA

This thesis is confidential and cannot be made public until December 31, 2024.

To my lovely sister, Pariveys, who has meant and continues to mean so much to me.

Hopefully, you will be aspired to a job in engineering.

Preface

First, I would like to offer my tremendous gratitude to my supervisor, ir. M. C. Naeije, for his invaluable guidance, feedback, and supervision throughout the course of my studies. I would also like to thank Dr. ir. S. Shroff for her advice and knowledge in the subject matter regarding structural modelling and optimization, for being on my research assessment committee, and in providing insightful comments and suggestions. In addition, many thanks go out to Dr. ir. R. Gardi from CIRA and T. Watts, ir. S. Lammens, and ir. S. van der Linden from S[&]T, for helping me throughout my thesis and for their advice along the way. I would also like to thank Prof. Visser for being a part of my thesis committee.

This thesis was supported and conducted at Science [&] Technology. In 2003, the program Future Launchers Preparatory Programme (FLPP) began by European Space Agency (ESA). Among others, this program aims to guarantee the safety of civilians, perform reusable launches and promote it, and to make space more accessible to everyone. Therefore, the Demise Observation Capsule (DOC) was developed and qualified for ESA by S[&]T as the prime contractor and seven other international partners. With the DOC, ESA will collect important information about the re-entry processes of launcher stages.

Currently, the first DOC is in its test phase has been designed for the worst-case environmental loads. The sequel DOC is the subject of this thesis report. The changes in the DOC configuration with respect to the host vehicle stage and launcher will be mapped and the results will be presented as to whether a generalized shape is or is not suitable for future missions.

Parandis Fatemi Ghomi
April 18, 2018

Summary

Satellites reach orbit by multi-stage launch vehicles. Adjacent stages re-enter or transfer into a graveyard orbit once their fuel runs out. In both cases, the stage must re-enter the Earth's atmosphere. Once the stage is re-entering the atmosphere, the low-melting-point materials melt and the inner parts of the stage will be exposed to excessive heat. With heat increasing, the parts will break into debris. Some of the fragments will burn in the atmosphere, others will crash into the Earth's surface. Since there is a lack of knowledge about the re-entering physics, the Demise Observation Capsule (DOC) project was started. The DOC collects information about re-entry progress of the launch vehicle stage where it is mounted upon. To obtain a broader knowledge of the re-entry progress, the DOC should be placed on several launchers and stages. Per location of the stage, different loads are applied on the DOC. It is preferred to mount the DOC, that is designed for that particular location. However, a generalized design concept that fits on several locations and stages, will reduce the cost and redesigning effort. Therefore, the thesis objective is to determine whether it is feasible to have a generalized DOC or an optimized DOC on a per-location basis. Additionally, the current DOC is designed for four locations. The second objective of this thesis is to optimize the current DOC and shift its center of gravity to the nose of the DOC to make it more aerodynamically stable.

The potential launchers and stages were investigated, and in total six locations were listed. The loads per location were computed. These loads were compared and the sizing loads per location were defined. Then, the DOC was modelled in ANSYS^{TM} by four load carrying bodies: the host vehicle interface (HVI), the back shell, the ballast, and the front shell. Additionally, the eight non-load carrying bodies modelled as lumped masses. Finite element analysis was implemented and the result of a mesh convergence analysis was a mesh size of 3 mm. Next, the model was analysed for modal, static structural, and random vibration analyses. The results of the current DOC analysis were investigated and compared with the optimized results. To optimize the DOC, the topology optimization model was selected using the Solid Isotropic Material with Penalization (SIMP) approach. This was implemented in ANSYS^{TM} to optimize the DOC model for all potential locations. The HVI and the front shell were selected as a *design* region with some surfaces excluded from optimization while the other two bodies were selected as a *non-design* regions. The results of the optimization required some changes in order to make the final model feasible. This was done in Catia, considering manufacturing and material constraints. The model was imported again back into ANSYS^{TM} to verify the optimization results.

The results show that the differences between the optimized DOC on a per-location basis was insignificant. In total, eight load cases were identified, where six of the load cases where the locations, one load case was the current loads defined for the DOC, and the other load case includes all six load cases combined. Having a generalized DOC is preferred, since the final masses and the visual results of the topology optimization is very close. Additionally, the sensitivity analysis shows that the connection between the HVI and the front shell are the largest weak points of the model. Furthermore, the analysis in the y-direction were neglected due to the stiff response of the DOC in that direction. The sensitivity analysis demonstrated that this will affect the final DOC configuration and therefore should be included in the analysis.

LIST OF SYMBOLS

Description	Symbol	Unit
Acceleration	a	$[\text{m/s}^2]$
Acceleration Spectral Density	ASD	$[(\text{m/s}^2)/\text{Hz}]$
Amplification factor	Q	[-]
Area	A	$[\text{m}^2]$
Axial force	F_a	[N]
Band width	Δf	[Hz]
Centre frequency	f_c	[Hz]
Constraints	G_i	[-]
Coordinates of the part	$\mathbf{r}_i$	[mm]
Density	ρ	$[\text{kg/mm}^3]$
Density per element	ρ_i	$[\text{kg/mm}^3]$
Design domain	Ω	[-]
Drag coefficient	C_D	[-]
Effective sectional area	A_s	$[\text{mm}^2]$
Element	E_i	[-]
Element density	ρ_e	$[\text{kg/mm}^3]$
Element volume	V_e	$[\text{mm}^3]$
Factor constant	β	[-]
Function	F	[-]
Mass	M	[kg]
Mass of part	m_i	[kg]
Maximum frequency	f_{max}	[Hz]
Minimum frequency	f_{min}	[Hz]
Natural frequency	f_n	[Hz]
Number	N	[-]
Penalization parameter	p	[-]
Power Spectral Density	PSD	$[\text{g}^2/\text{Hz}]$
Pressure	p	[Pa]
Pressure power spectral density	W_p	$[\text{Pa}^2/\text{Hz}]$
Reference pressure	p_{ref}	[Pa]
Root mean square acceleration	G_{rms}	$[\text{g}^2/\text{Hz}]$
Sound Pressure Levels	SPL	[dB]
Spring stiffness	k	[N/m]
State field	$\mathbf{u}$	[-]
Step size	h	[-]
Stress	σ	$[\text{N/mm}^2]$
Surface	S	$[\text{mm}^2]$
Tensile strength	σ_y	$[\text{N/mm}^2]$
Transmissibility factor	T	[-]
Volume	V	$[\text{mm}^3]$
Volume constraint	G_0	[-]
Weight	W	$[\text{kg}\,\text{m/s}^2]$
Yield stress	σ_Y	$[\text{N/mm}^2]$
Young's modulus	E	$[\text{N/mm}^2]$

LIST OF ABBREVIATIONS

Abbreviation	Description
ATV	Automated Transfer Vehicle
AVUM	Attitude and Vernier Upper Module
CAD	Computer-Aided Design
CoM	Center of Mass
CSG	Centre Spatial Guyanais
DOC	Demise Observation Capsule
ECI	Earth Centered Inertial
ESA	European Space Agency
ESO	Evolutionary Structural Optimization
FEA	Finite Element Analysis
FEM	Finite Element Method
FS	Front Shell
GTO	Geostationary Transfer Orbit
HMT	Highest Maximum Total
HV	Host Vehicle
ISS	International Space Station
LEO	Low Earth Orbit
MEO	Medium Earth Orbit
MPC	Multi-Point Constraint
PLA	Payload Adapter
QSL	Quasi-Static Load
RF	Reaction Force
SIMP	Solid Isotropic Material with Penalization
SRS	Shock Response Spectrum
SSO	Sun–Synchronous Orbit
TPS	Temperature Protection System
UC	Upper Composite
VEB	Vehicle Equipment Bay
VESPA	Vega Secondary Payload Adapter
Z23	Zefiro 23
Z9	Zefiro 9

List of Figures

List of Tables

Contents

1

Introduction

The aim of the thesis is to investigate the feasibility of generalizing the Demise Observation Capsule (DOC). This chapter presents the background information in Section 1.1. The problem will be defined in Section 1.2. Section 1.3 describes the main and sub-objectives of this thesis. A study has been conducted to select a proper software during the literature study, Section 1.4 summarizes this study. Finally, the layout of this thesis is described in Section 1.5.

1.1. Background

Satellites are brought to orbit by multi-stage launch vehicles. When a launcher stage uses all its fuel, it is separated from the upper stages. This empty stage is either dropped back into the atmosphere, as is the case with most stages, or is transferred into graveyard orbit. The stages that are transferred into graveyard orbit will slowly decay until they re-enter the Earth's atmosphere. In both cases, the stage must re-enter the atmosphere (Heinrich et al., 2015).

When the detached segment is re-entering the atmosphere, the aerodynamic heating and the aerodynamic load increase to the point where low-melting-point materials melt. Melted heating protection will leave the other inner objects to be exposed to excessive heat. With the heat increasing and with deceleration loads, the objects gradually break into parts and multiple pieces of debris. Although some fragments demise through aero-thermodynamic ablation, many still survive and crash into the Earth's surface. The collection of the impact points of all the surviving fragments is called the footprint of a stage.

The current understanding of the re-entry physics and the interactions between the object's parts and the atmosphere is essentially theoretical. Computer tools, which are used to estimate the ground hazard associated with re-entries, have been developed from physics-based first-principles models and have been marginally validated using very limited data derived from visual evidence and analyses of recovered hardware (Cicalo et al., 2017). The deviation between the actual footprint and the models has indicated that there are areas of research where the actual behaviour of the fragments may not be well understood.

With the growing number of operational satellites (e.g. constellations) and space debris objects, and with de-orbit requirements, a better understanding and mastering of atmospheric re-entry has now become of the utmost importance. Looking in terms of mission success, the on-orbit collision risks can be reduced and the returning spacecraft can be retrieved more successfully. In terms of public safety, the general population will have a lower chance of being hit by falling space objects and be exposed to toxic atmosphere. And finally, for technology enhancement reasons (Lammens et al., 2018).

In 2003, the program Future Launchers Preparatory Programme (FLPP) began by European Space Agency (ESA). Among others, this program aims to guarantee the safety of civilians, perform reusable launches and promote it, and make space more accessible (ESA, 2017). Consequently, de-orbitation of launcher's upper stages are mandatory for future launcher developments. In the frame of FLPP, it was decided to explore this topic by developing an observation capsule, collecting data relevant to upper stage break-up and demise,

visualizing the critical phenomena. The collection of specific data contributes to the validation of mathematical models of the prediction for re-entry in all phases, such as fragmentation, explosion, demise, and trajectories. It also enlarges the existing database addressing structural, aerothermo-dynamical, and materials behaviour.

Therefore, DOC is developed and qualified for ESA by S[&]T as the primary contractor and seven other international partners. With the DOC, ESA will collect information about the re-entry progress of launch vehicle stages. It basically records and collects important flight and environmental data that is needed to achieve a larger understanding in the physics and engineering as parts of the re-entry process. The analysis of the re-entry data will help in accurately predicting break-up altitudes, debris trajectories, and ground impact footprint. These analyses are therefore critical not only to mission success, but more importantly for improving public safety. To summarize, the DOC's objectives are:

- To study Low Earth Orbit of the stage by means of an independent capsule;

- To detach from the stage and observe demise of the stage using the camera mounted on the DOC's back;

- To collect flight data to validate the destructive re-entry trajectory of various stages.

The first DOC is in test phase at this moment and is planned to be placed on the Vega upper stage: Attitude and Vernier Upper Module (AVUM). When the upper stage separates, the DOC will wake up by sensing vibrations of the separation. It will start measuring while it is still attached on the host vehicle. At some point during the mission the capsule separates from the stage to not be destroyed along with the re-entry objects. After separation, the DOC will continue following a ballistic re-entry trajectory until it impacts the Earth. During re-entry, DOC performs in-situ measurements and short or long-range remote observations of the demise of the host vehicle stage. The mission profile of the DOC is illustrated in Figure 1.1.

During the re-entering the Earth, the capsule's nose should point into the Earth. The front part is qualified to protect the DOC against extreme re-entry heat. If the DOC re-enter the Earth pointing its back to the Earth, it will not resist the heat and therefore can not conduct its mission. Additionally, the HVI camera mounted on the back of the DOC should point in the direction of the host vehicle to screen the host vehicle behaviour. Considering these two reasons, it is crucial for DOC mission to re-enter the Earth pointing its noise towards the Earth. The first qualification flight for the DOC was expected to be in early 2018. However, during the last analysis, the DOC was found not to be in stable flight conditions. According to Morgan and Stewart (1998), the passive stability of flight re-entry vehicle is realized by placing the mass center to the noise of the re-entry vehicle. Hence, after separation the DOC's will point passively towards the Earth when the center of gravity of the DOC is shifted towards its nose. This problem can be solved by reducing the mass behind its center of gravity. Furthermore, there is demand from ESA to place the DOC on other launchers and at different stages to obtain broader environmental data. Therefore, to reduce the cost and effort, the DOC concept should be (re)-designed to fit on potential launchers.

1.2. Problem Definition

Some launch vehicles with a destructive re-entry trajectory, meaning that the several stages, inter-stages, and upper modules, are not designed to survive re-entry. They will break up in the atmosphere and impact the Earth's surface to comply with the international regulations (e.g. France/European space law) (Bonnal et al., 2009). This will reduce the risks of harm and damage on the ground. These fragments will imply a varying footprint which means the survived fragments will impact the Earth on an unpredictable and broad surface.

With the DOC, important data about the re-entry of the launcher stages can be collected. The DOC is able to gather flight and environmental data to get a better understanding of the re-entry process of the stages. This data will help to predict the break up altitudes, debris trajectories and ground impact footprint more accurately.

Engineers at S[&]T are already working on the conceptual design of the DOC system on the upper stage of the Vega flight, the AVUM. However, there is interest from the client to have the DOC on different stages and parts of the Vega launch vehicle and even on different launchers. That is because every mission needs a
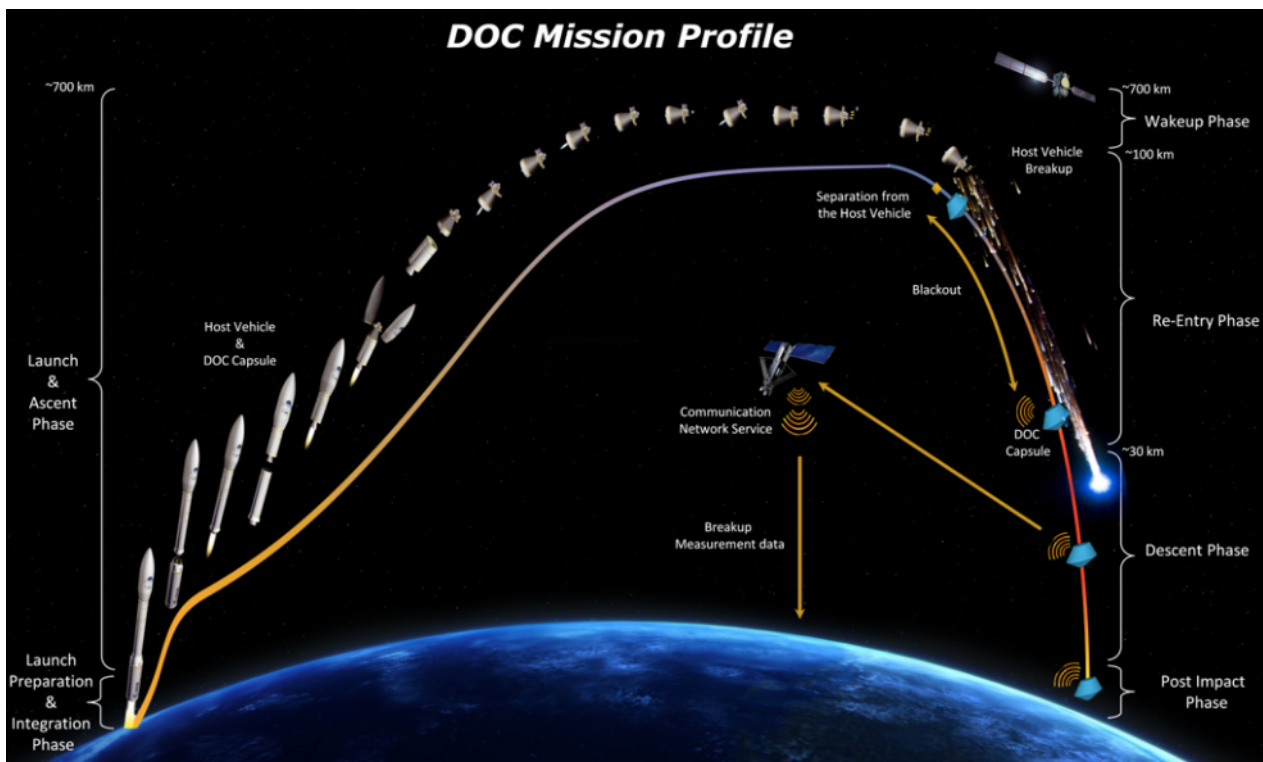
Figure 1.1: DOC Mission Profile (Science and Technology, 2017)

launcher and every launch stage has a different re-entry footprint. Several unknown variables are playing a role during their re-entry that the only way to validate the simulations is to launch several DOC's on different stages and different launchers and validate the simulations. These analyses are critical not only to mission success, but more importantly for improving public safety aspects of such re-entry scenarios.

To reduce the cost and effort, the DOC should be (re-)designed in such a way that it can be placed on all potential host vehicles. Hereby, one generalized DOC can be fit on every stage of every launcher and withstand the loads and perform its tasks. The feasibility analysis of this will be performed in this thesis research.

Furthermore, the current design of the DOC should be more stable, which means that the center of the gravity of the DOC excluding the host vehicle interface should be shifted to the front. Any movement to the DOCs nose improves the stability of the DOC.

Initial requirements and limitations imposed on the next generation and optimized DOC are explained here. The next DOC should be able to be located on several launchers/stages and not only on the AVUM. Furthermore, the main goal of this mission is to study the Low Earth Orbit (LEO) re-entry atmosphere. The Earth atmosphere can be divided into two phases, the atmospheric phase and the exo-atmospheric phase. Exo-atmosphere is beyond the 100 km (Suresh and Sivan, 2015) and host vehicle should be above this altitude during its re-entry phase. S[&]T stated in a technical report, *Mission design definition and justification file*[1], the relevant atmosphere will be present in case the launcher stage/part exceeds an altitude of 150 km and average nominal mission speed of almost 6 km/s. Therefore, the first requirements on the host vehicle are:

Launch-1 The potential stage/part shall exceed an altitude of 150 km;

Launch-2 The potential stage/part shall exceed an average nominal mission speed of 6 km/s;

Launch-3 The DOC dimensions should be less than the available space on launcher.

---

[1]Mission design definition and justification file, Issue date: March 15, 2016. This is a classified document and only available through S[&]T.

ESA stated in *System and subsystem technical requirement specification document*[2], the next requirements.

Design-Space-1 Capsule structure shall provide structural integrity and stiffness in all mission phases;

Design-Space-2 The host vehicle interface shall provide structural integrity and stiffness in all mission phases;

Design-Space-3 The maximum weight of the DOC should not exceed 10 kg;

Design-Space-4 The DOC shape should fulfilled the mission objective;

Design-Space-5 The internal volume should be able to offer space to avionics, sensors, equipment, etc. to perform its objective.

1.3. Research Objective

ESA is interested in mounting the DOC on different stages and launchers. Therefore, all the potential locations are limited to the launchers which have been built or are currently in use by ESA. This decision has been made in discussion with the head contractor of this project, S[&]T.

In an ideal situation, the DOC can be placed on all stages/parts of launch vehicles and at the same time it is optimized for that location. During the literature study, it was found that a generalized design concept that fits on every host vehicle with a destructive re-entry trajectory and on several locations and stages, will reduce the cost and re-designing process. On the other hand, a generalized model, which is designed for the worst case situation, may not be optimized for a situation with much lower environmental forces. In other words, an optimized DOC for all locations may not be an optimized DOC per location. This could make a generalized model not efficient.

For this reason, the main research question is as follows:

Is it feasible to generalize the DOC concept design so that it will fit on every ESA launcher and stage and meet the predefined requirements and will withstand environmental loads while general operability of the DOC is guaranteed?

Additionally, during a meeting on the 27th of September 2017 at ESA, the client expressed their concerns about the stability of the DOC. The stability of the vehicle is related to the location of the center of mass. Therefore, the next question was added.

How can the center of gravity be shifted on the DOC to its nose under the current designed loads such that the DOC can be made more stable?

To follow a structured path to answer these questions, some sub-questions were generated.

1. Where can the DOC be mounted?

    - Which launchers meet the requirements?
    - Which stages of the launchers meet the requirements?
    - Which parts of the stages meet the requirements?

2. Which loads are applied on the DOC?

    - Which phase, transfer, ascent or re-entry is the most critical phase for structural design?
    - Which loads are applied on the DOC per location?
    - Which load is critical per location?
    - What are the design loads of the current model?

3. How to model the system?

---

[2]System and subsystem technical requirement specification document, Issue date: October 30, 2016. This is a classified document and only available through S[&]T.

- How to simulate the host vehicle interface and the DOC?

- Which modelling method is the most suitable techniques?

- How accurate are the selected modelling methods?

- How sensitive is the system to the uncertainties of the modelling method?

- What is the DOC's response to uncertainties?

4. How to optimize the model?

  - Which optimization method is the best?

  - What are the optimization objectives?

  - What are the constraints and limitations on re-designing the model?

5. How does the optimized DOC model change per host vehicle?

  - What are the differences of optimized DOCs in the geometric aspects?

  - How does the mass of optimized DOCs change on different locations?

  - How are the location and the results related?

  - What are the differences of an optimized DOC per location compared to an optimized DOC for all loads applied at the same time?

6. How can the DOC design be generalized to fit on every host vehicle and per mounting location?

  - Does a generalization of the concept have any advantages?

7. How sensitive are the results?

  - How sensitive is the critical load to the uncertainties and assumptions?

  - How sensitive are the results to the load assumptions?

  - How sensitive are the results to the model assumptions?

  - How sensitive are the results to the input loads?

8. How can the current DOC design be made more stable?

  - Which parts of the DOC can be optimized?

  - How much can the mass be reduced in these parts?

1.4. Software Selection

The current DOC design is simulated in the ANSYS^{TM}. Furthermore, ANSYS, Abaqus, Nastran and Patran are available on the blackboard for free download and can be used for Finite Element Methods (FEM). Each has its own advantages and limitations when compared to the other. During the literature study, these software tools were studied and compared using the theory propounded in (Harris, 2015; Miller, 2010*a*; *ANSYS workbench user's guide*, 2009).

ANSYS
ANSYS is a general software which is used to simulate interactions of all disciplines of physics, structural, vibrations and dynamics for engineers. It gives the opportunity for taking only needed features. It can be integrated with other software by adding computer-aided design (CAD) and Finite Element Analysis (FEA) modules. This software is able to perform engineering analyses quickly, safely and practically. It has the ability to build a geometry with its preprocessing and after carrying analyses, the results can be illustrated as numerical and graphical (postprocessing).

Abaqus
Abaqus is an engineering software suited for FEA and CAD. It is used in aerospace and automotive industries. This software consists of three stages, preprocessing, processing and finally post-processing. In the first

phase, a model is created and that forms the input for the next phase. The second stage is a solver and executes FEA. The next stage can generate visual results by graphs or animations. Furthermore, Abaqus is able to only perform the second stage (solver) and allows the first and third stage be done by a compatible CAD software like Catia.

Nastran

Nastran is a multidisciplinary structural analysis used by engineers to perform static, dynamic, and buckling analyses across the linear domains. By applying forces and moments on the model, Nastran can ensure whether the structure has the necessary strength and stiffness. It has high performance computing capabilities enabling to solve the problem much faster. A disadvantage of this software tool is that it needs pre- and post-processing by another software like Patran and it can only handle linear models.

Patran

Patran is most widely used as pre- and post-processing software for FEA. It provides solid modelling, meshing and analysis set-up for solvers like Nastran, Abaqus and Ansys, etc. This tool is required in case Nastran is used.

Trade-off

A trade-off needs to be conducted between Nastran/Patran, ANSYS, Abaqus. The criteria will be:

1. User friendly;

2. Available tutorials and information;

3. Error;

4. Computation time.

According to S. Shroff, all four software are user friendly and strongly depends on personal preference. Therefore, the first criterion was eliminated. Nastran/Patran and Abaqus score higher on the second criterion, since there are significant knowledge and experience in working with these software within the author department. However, the current DOC is modelled in ANSYS and its model is available. There is a chance that current model will not be imported correctly to Nastran or Abaqus and this will lead to errors and thus extra effort. Therefore, ANSYS scores more on the third and fourth criteria and therefore it is decided to select ANSYS.

1.5. Thesis Layout

The purpose of this thesis is to study the feasibility of the DOC generalization. This thesis is divided into ten chapters and the layout is as follows. Chapter 2 analyses the potential launchers and stages to mount the DOC following the requirements **Launch-1** and **Launch-2**. Several stages of the launchers will be recognized here.

Chapter 3 determines the imposed loads by the launchers on the DOC. All loads will be converted to the same unit for comparison. The critical sizing loads per defined locations are computed here.

Chapter 4 describes the DOC model. First, the physical layout including the subsystems and its interface with the host vehicle are explained. Then, the simulation of the DOC in ANSYS is represented. Finite element method is selected for numerical approach.

Once the model is simulated into the software, the modal, static structural, and random vibration analyses are conducted to analyse the model. The findings are included in Chapter 5. Chapter 6 introduces the optimization methods and selects and underlines the topology optimization and its most common methods applied in structural topology optimization. The purpose of this chapter is to present the topology mass minimization of the DOC, subject to material failure constraints and volume constraint in multiple load cases.

Chapter 7 represents the results of the topology optimization. First, the results of the software are described. Then, a feasible model is designed to meet the manufacturing requirements. Finally, a solution was illustrated for the current DOC model.

The inputs and the results are verified and validated in Chapter 8. The input load codes and the input model in the software are verified and the optimized feasible model is validated. A sensitivity analysis has been conducted to explore the model in Chapter 9.

In chapter 10, conclusions are drawn about the significant findings in this thesis, and recommendations about what can be done in the future based on this work are presented. Appendix A illustrates and describes additional information and results. The literature study results are also included in this chapter.

<div align="right">

2

</div>

Launcher Selection Analysis

This chapter analyses the potential launchers for the Demise Observation Capsule (DOC). First, an analysis of the potential launchers on which the DOC can be placed is discussed in Section 2.1. Next, an introduction to the selected potential launchers and their performance information is discussed. The flight performance is critical information that helps in finding the suitable host vehicle locations and therefore the critical load on that location. Ariane 5, Vega and Soyuz are described in Sections 2.2, 2.3 and 2.4, respectively.

2.1. Potential Launchers and Stages

DOC mission is applicable to all launchers with a destructive re-entry trajectory, meaning that the stages are not designed to survive the re-entry. Many launchers and their stages belong to this group, this list will be narrowed down and the approach is explained in this section.

As explained in Section 1.3, since ESA is the client, the DOC needs to be implemented on the next European Space Agency (ESA) missions. Therefore, the potential launchers are restricted to the ones which have been built and are currently in use by ESA. A study has been done on the ESA future missions during the literature study and a portfolio of missions from 2018 has been listed and illustrated in Appendix A.1.

From this survey, it was clear that ESA planned to use the family launchers of Ariane, Vega and Soyuz as potential launchers for future missions. However, the launchers in development, like Ariane 6, Vega-C, and Vega-E are eliminated from the list since no detailed information about these launchers is available yet. Hence, the potential launchers are restricted to Ariane 5, Vega and Soyuz.

The main goal of the DOC mission is to study the Low Earth Orbit (LEO) re-entry atmosphere. S[&]T describes this in a technical report, *DOC technical description and safety dossier*[1], that the relevant atmosphere will be present in case the launcher stage/part exceeds an altitude of 150 km and average nominal mission speed of almost 6 km/s (**Launch-1** and **Launch-2** in Section 1.2). A list of potential launchers with their stages, height, and speed at separation are given in Table 2.1. These two requirements are used to eliminate the stages.

Ariane 5 consists of three stages: the solid propellant boosters (EPA), the main cryogenis stage (EPC), and the upper composite stage (UC). EPA of Ariane 5 are not suitable for DOC mission, because they do not reach the minimal altitude, nor they meet the minimum required velocity. However, the EPC and the UC meet these requirements and are potential stages for embarking the DOC. They are indicated in green in Table 2.1.

Vega consists of four stages: the P80, Zefiro 23, Zefiro 9, and Attitude and Vernier Upper Module (AVUM). First and second stage of the Vega launcher, the P80 and Zefiro 23, do not meet both Requirement **Launch-1** and **Launch-2**. The Zefiro 9 and AVUM stages however meet both requirements and thus are of interest for studying re-entering phenomena.

---

[1]DOC technical description and safety dossier, Issue date: Augustus 14, 2017. This is a classified document and only available through S[&]T.

Table 2.1: Overview of the Launchers (Lagier, 2016; Perez, 2014, 2012)

Launcher	Stage	Height at Separation [km]	Relative Speed [km/s]
Ariane 5	Solid propellant boosters (EAP)	59.2	1.98
	Main cryogenic stage (EPC)	152.1	6.73
	Upper composite (UC)	400	7.36
Vega	P80 (first stage)	52.0	1.83
	Zefiro 23 (second stage)	113	3.87
	Zefiro 9 (third stage)	179	7.51
	Attitude and vernier upper module	288	7.86
Soyuz	4 Boosters (first stage)	42.8	1.74
	Core stage	147.6	3.55
	Third stage	171.9	7.29
	Fregat	≈ 650	≈ 9.4

Soyuz consists of four boosters, a core stage, a third stage, and the Fregat. The first stage of Soyuz consists of four boosters and separates at an altitude lower than required and therefore, this stage is not considered. The core stage does not reach the required velocity and the minimum altitude, therefore, this stage is also eliminated. The next potential stages are the third stage and Fregat stage of the Soyuz launcher. Both exceed the required height and velocity at separation.

2.2. Ariane 5

This section provides the information necessary of the performance of the Ariane 5. The sequence of flight event will specify the loads applied on the DOC, therefore a brief explanation of the flight is discussed here. Furthermore, the Ariane 5 stacking configuration is illustrated in Figure 2.4. The information presented in this section are obtained from Lagier (2016); ESA (2018), unless noted differently.

General Description

Ariane 5 consists of two solid rocket boosters which provide 90% of Ariane 5's thrust at lift-off, burn for 130 seconds, and then are dropped into the ocean. A cryogenic core stage, called the EPC, is ignited on the ground and provides the remaining thrust for the first part of the flight until upper stage separation. When EPC stage's fuel is gone, it re-enters the Earth's atmosphere.

The upper composite stage (UC) is on top of the EPC and below the upper part. The UC and the EPC are connected via an inter-stage called InterStage Structure. The UC's ignition starts a few seconds after the EPC separation. The UC consists of a cryogenic upper stage, a vehicle equipment bay (VEB), and a lower adapter called LVA 3936. On top of the UC, the upper part stage is stacked and it consists of payload, fairing and upper adapter.

Flight Profile

Although the fairing parts are protecting the upper part of the Ariane 5, the fairing will be jettisoned at an altitude of 107 km and a velocity of 2.4 km/s. Before the fuel of the EPC stage runs out. The jettison of these parts happen at a lower altitude and velocity, hence their re-entry is not considered for study.

For standard missions, the EPC stage always re-enters the Earth and splashes down in the Atlantic Ocean. UC components will re-enter the Earth after separation and are attractive for study. Furthermore, ESA published in ESA (2018) that Ariane's upper stage will be left in a stable graveyard orbit and will not perform a re-entry burn. A typical flight sequence of Ariane 5 is illustrated in Figure 2.1.

Selection

The locations where the DOC can be placed on are listed by S[&]T. The following list of the Ariane 5's stages/parts meets requirements **Launch-1** to **Launch-3** of Section 1.2.

- Upper composite:

    - LVA 3936;
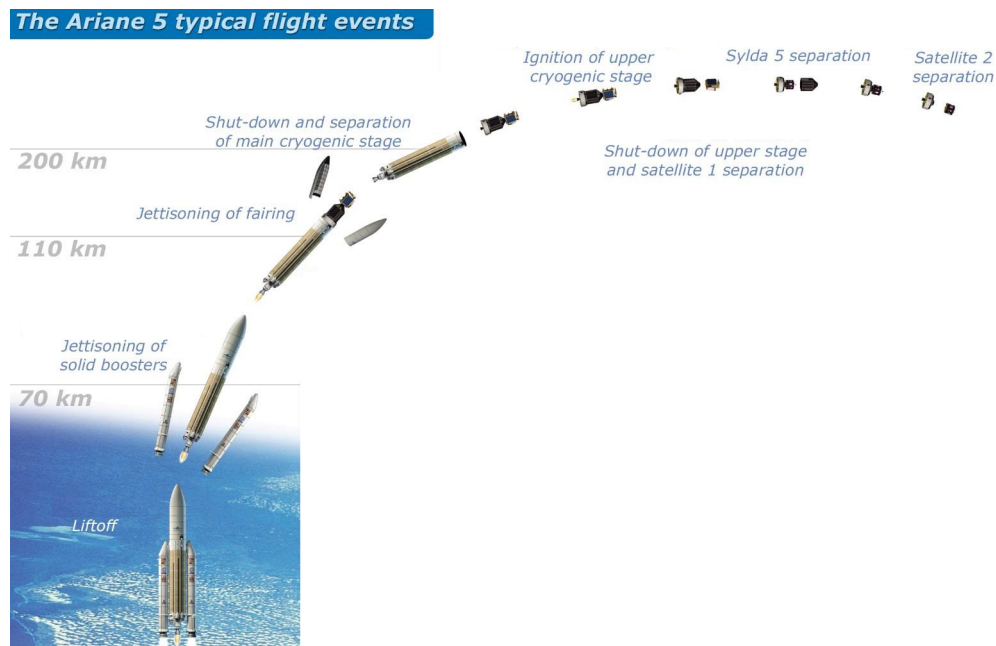
Figure 2.1: Typical Sequence of Events of Ariane 5 (Lagier, 2016)

  – VEB;

  – CU stage;

  – InterStage Structure.

• Crogenic main core stage.

2.3. Vega

This section focuses on the Vega launcher. First, a general description of the launcher is given. Then the flight profile with some important data to select the parts of the stages are defined. Finally, the final parts that meet the requirements **Launch-1** through **Launch-3** in Section 1.2 are listed. The information of this section is provided from Perez (2014).

General Description

Vega was developed by European Space Agency and compliments Ariane 5 and Soyuz by covering for the small to medium payloads, injecting satellites into Sun-Synchronous orbits (SSO), polar circular orbits and Low Earth (LEO) orbits. It consists of three solid propellant stages called *P80*, *Zefiro 23* (Z23) and *Zefiro 9* (Z9). On top of that, the AVUM, a re-ignitable upper stage, is located as illustrated in Figure 2.4.

As mentioned before, Z9 and AVUM stages are of interest to this study. The Z9 stage is 4.12 m long and is loaded with 10567 kg of solid propellant. Although the Z9 is the smallest solid rocket motor on the Vega launcher, it has the longest burn time of almost 120 seconds and provides maximum vacuum thrust of 317 kN.

The interface between the Z23 second stage and the Z9 stage are established by the 2/3 inter-stage, which is made by a thin aluminium skin cylinder and stiffened by internal stringers. On top of the Z9 stage, the interfaces with the AVUM upper stage and adjacent structures are assured by a 3/AVUM inter-stage.

On the other side, AVUM is connected to the Payload Adapters (PLA). Vega offers three different types of PLA: the PLA 937, PLA 1194, and Vega Secondary Payload Adapter (VESPA). The numbers of PLA 937 and PLA 1194 refer to the coupling diameter in millimetres to the payload. These two are proposed for single launches, while VESPA is recommended for multiple launches.
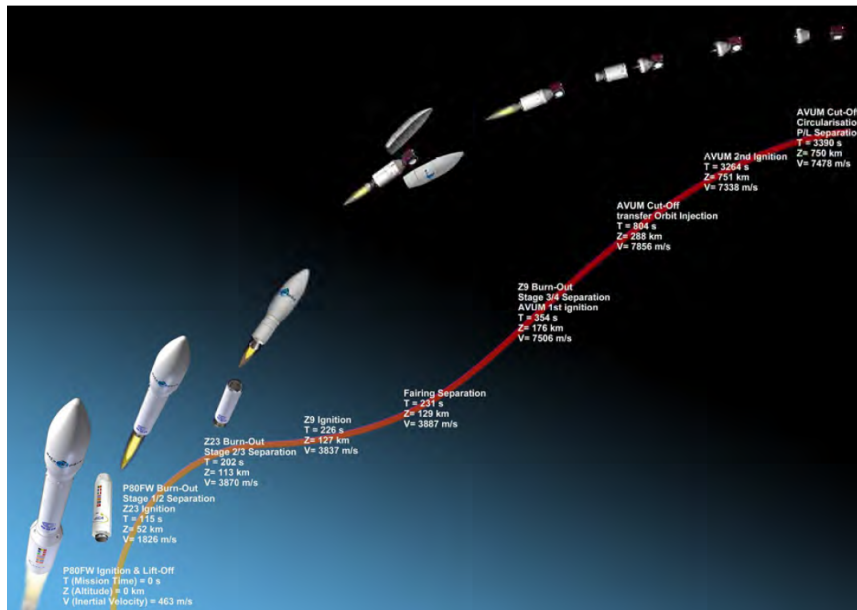
Figure 2.2: Ascent Profiles and Associated Sequence of Events of Vega (Perez, 2014)

Flight Profile

The fairing separation happens at an altitude of 129 km with a velocity of 3.8 km/s. Fairing parts do not meet the requirements and therefore they are of no interest.

The Z9 will passively re-enter in all Vega mission cases after separation and is in all cases of interest for this study. AVUM can be restarted up to 5 times depending on the mission. This stage can de-orbit either by natural decay or by initiating a de-orbit burn. The first option, de-orbiting will takes around 25 years and is not interesting for this study case. However, active de-orbiting is suitable of this study and the mission with this flight profile should be selected.

The VESPA upper part is only 100 kg and separates from the bottom part during the ascent phase. S[&]T stated in their technical report, *Launcher selection and analysis*[2], that this segment is too small and will break into insignificant segments that will burn very fast in the atmosphere and hence the VESPA upper part is of no interest to follow. However, the bottom part of VESPA performs de-orbiting and therefore it meets the aforementioned requirements and are of interest to study. This is also the case for both single launch adapters. A typical Vega ascent profiles and associated sequence of events are shown in Figure 2.2.

Selection

A location analysis is performed on the Vega launcher and is summarized as:

- AVUM stage:

    - AVUM;

    - PLA 937;

    - PLA 1194;

    - Bottom part of VESPA .

- Zefiro 9:

    - 3/AVUM interstage;

    - Zefiro 9.

---

[2]Launcher selection and analysis, Issue date: January 31, 2017. This is a classified document and only available through S[&]T.

2.4. Soyuz

This section summarises the information necessary to the performance of the Soyuz. The general description of the Soyuz launcher, the flight profile and the final parts that meet the requirements **Launch-1** through **Launch-3** in Section 1.2 are described in this section.

General Description

Soyuz was intended to compliment the Ariane 5 and Vega launchers by providing a way for medium-weight payloads to get into the LEO and to small satellites into Geostationary Transfer Orbits (GTO). Soyuz is developed and the new version is called Soyuz/ST, which has an enhanced payload volume. Soyuz and Soyuz/ST offer a restartable Fregat upper stage, which enhances the Soyuz to reach the missions extending the LEO.

Combining the Soyuz and the Soyuz/ST with the Fregat upper stage makes this launcher very flexible. This gives the opportunity to cover a wide range of missions from spacecraft delivery to GTO, to injection into the SSO and polar orbit, as well as low and high circular or elliptical orbits, and escape trajectories. Therefore, once the DOC will be placed on the Soyuz additional research has to be done on the mission profile to define a suitable location. This is beyond the purpose of this thesis and only a general location analysis is performed to define the loads.

Soyuz consists primarily of the following components: the first stage is a lower composite consisting of four liquid-fuelled boosters. The four boosters are aligned around the core stage, after burning for 118 seconds they are discarded. The core stage construction is similar to the boosters and burns for 290 seconds.

The third stage is on top of the second core stage. The interface between the third stage and the Fregat upper stage is guaranteed by an interstage. On top of the restartable Fregat upper stage, an adapter is located and the whole section is protected by two fairings.

Flight Profile

Fairing jettison happens at an altitude of 106 km with a velocity of 2.45 km/s. Fairing parts do not meet the requirements and therefore they are not of interest to study.

The four boosters and the core stage are ignited on the ground. The core stage continues to perform after boosters shut-down and separation. The third stage ignition starts approximately two minutes before shutdown of the second stage and assists with the separation of the second stage. This single main engine is jettisoned in three sections. After reaching the predetermined velocity, third stage will separate and perform de-orbiting.

At the end of the three phases, the Fregat is ignited. It consists of six spherical tanks, which consists of four for propellant tanks and two for avionics. The Fregat phase typically consists of one or two burns to reach the targeted orbit, depending upon the final orbit altitude, eccentricity and inclination.

Finally, Fregat will separate from the spacecraft and follow a required time delay to get a safe distance between the spacecraft and itself. Fregat upper stage will conduct a de-orbit burn or orbit disposal manoeuvre depending on the mission profile (Perez, 2012). A typical ascent profile of Soyuz is illustrated in Figure 2.3.

Selection

The location analysis indicates the following options:

- Third stage:
    - Third stage;
    - Interstage.

- Fregat upper stage:
    - Single payload adapter;
    - Multi payload adapter.

1	Lift-off (KP)	0.0
2	Max. dynamic pressure	72.0
3	Boosters intermediate thrust	112.0
4	Boosters vernier cut-off	117.7
5	I-II stage separation	118.1
6	Fairing jettisoning	208.4
7	II-III stage separation	287.6
8	III stage aft section jettisoning	300.4
9	III stage engine cut-off	558.6
10	Nose Module separation	561.9
11	ACS thrusters ignition	566.9
12	Fregat MPS firing	621.9
13	Fregat MPS cut-off	1685.0
14	S/C separation	~ 2000 (depending of S/C separation conditions)
15	Fregat deorbitation	As required by mission

Figure 2.3: Ascent Profiles and Associated Sequence of Events of Soyuz (Perez, 2012)
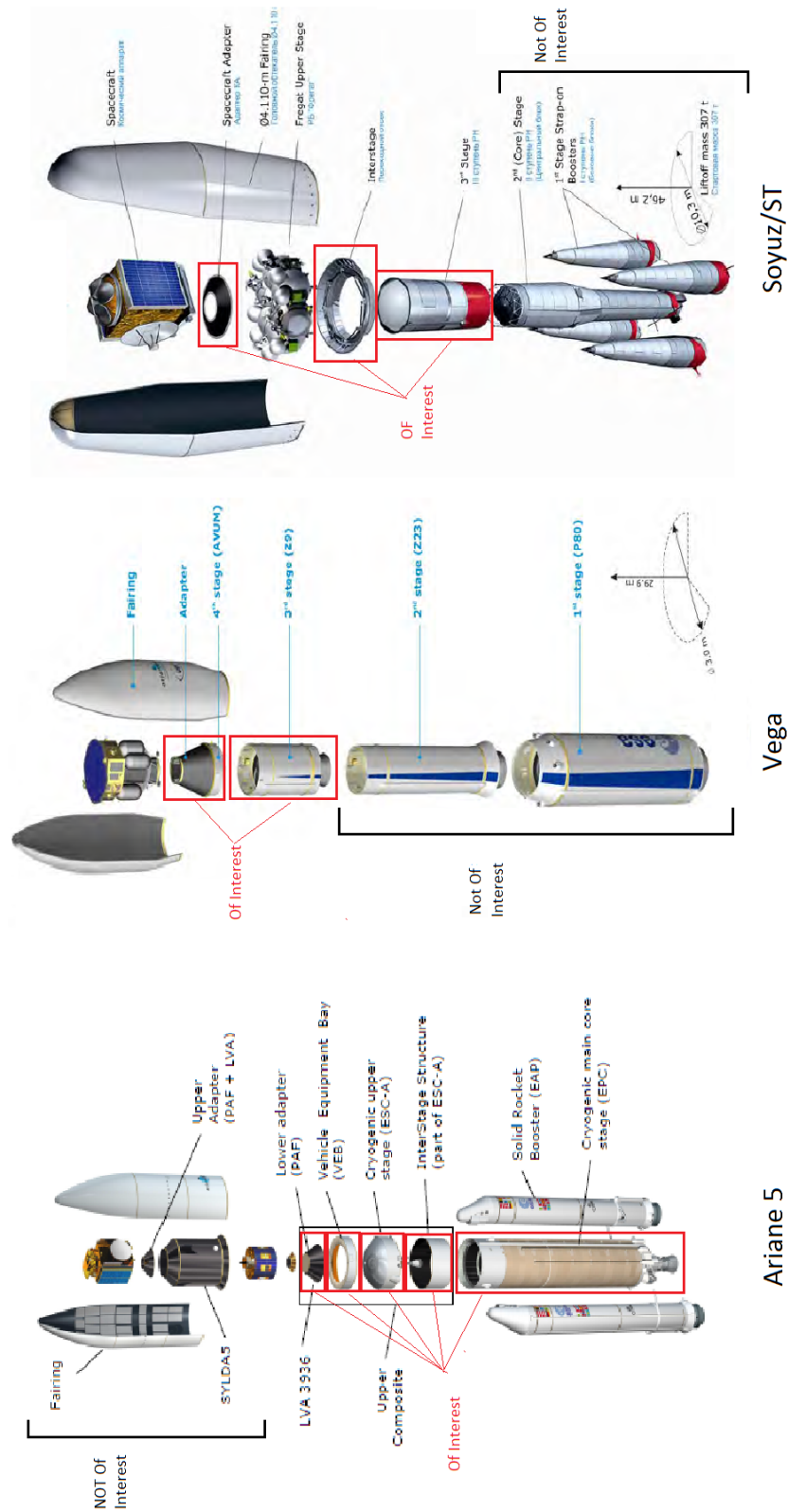
Figure 2.4: Ariane 5, Vega and Soyuz/ST Configurations (Perez, 2012, 2014; Lagier, 2016)

<div style="text-align: right; font-size: 4em;">3</div>

Environmental Loads

This chapter contains information on the launchers' environment and their loads imposed on the Demise Observation Capsule (DOC). The DOC's constraints and design are subjected to its location on the launch vehicle. In this chapter, an analysis has been done to define the sizing loads per location on the three launchers.

First, in Section 3.1, an introduction to the general aspect of the launch loads is explained as well as a basic definition of the present loads during the transfer, launch and re-entry. After that, in Section 3.2, the loads of the three launchers are defined. In Section 3.3, the methods used to convert the loads into static inertial loads are explained. Section 3.4 describes the converted loads of the launchers, which will be used as input for modelling.

3.1. Introduction to Environmental Loads

Various loads are applied on the DOC during the transfer, ascent and de-orbiting phase. The loads are not equally critical, their level of criticality depends on the type of their structure. In this section, an introduction to the possible loads is described.

S[&]T stated in, *DOC technical description and safety dossier*[1], that the loads during the transport from the factory to the launch platform are negligible in comparison with the imposed loads during the ascent phase. This is a valid statement, since the DOC has a maximum mass of 10 kg and a maximum dimension of 33×30 cm[2] and hence transporting such a small body with minimum exposing loads is not complicated.

The DOC is supposed to survive the re-entry to be able to transfer the data, although according to S[&]T surviving the impact is not required. S[&]T reported in, *Shape detailed design and detailed configuration*[2], that the loads during the ascent phase are much higher than the loads during the re-entry. This statement has been confirmed by several experts, Hammond (2001); Wertz and Larson (1999); Muylaert et al. (2001), reporting that loads are important parameters in ascent phase, whereas high temperature effects are dominant for re-entry phase. It can be concluded that the loads during the ascent phase are much higher than the loads during the transport and re-entry phase.

During the ascent phase, loads are driven by transient events, such as engine ignition, engine shut-down, wind gusts (aerodynamic sources), and separation of the stages, fairing or the DOC itself. The loads which can be encountered due to these events are listed below (Wijker, 2009, 2008).

Natural Frequencies
Natural frequency is the frequency at which a system without a damping force tends to oscillate. The natural frequency acts as a design requirement and is imposed in order to limit the dynamic coupling of the DOC

---

[1]DOC technical description and safety dossier, Issue date: Augustus 14, 2017. This is a classified document and only available through S[&]T.

[2]Shape detailed design and detailed configuration, Issue date: Augustus 1, 2017. This is a classified document and only available through S[&]T.

with the launcher. Section 5.2 explains this design requirement in detail.

Steady-State Loads
The maximum steady-state acceleration, which is a combination of static and dynamics loads, in the launch direction is expected to occur during the end of the propulsion phase of a rocket stage. At that point, the mass of the launcher is minimal while the thrust remains the same, therefore the acceleration increases. In general, the lateral steady-state accelerations are lower than the longitudinal steady-state accelerations. In the launcher user manuals, the steady-state loads are expressed as acceleration in g.

Sinusoidal Loads
This load arises as a result of the interaction between launch vehicle mode forms and loads occurring during either lift-off or combustion of the engines. During the lift-off the thrust will increase fast and cause a shock load that excites the low frequency. During combustion of the engines, sinusoidal vibrations occur both in and adjacent to the launch direction. Sinusoidal loads strength is expressed as sine amplitudes in g within a frequency bandwidth that is usually below 100 Hz.

Acoustic Loads
Acoustic load is generated either by the noise of the launch vehicle engines, separation of the airflow along the launcher, or aerodynamic noise and is usually expressed in a frequency spectrum between 20 and 10000 Hz. The strength of the noise field is indicated by sound pressure levels (SPL) and is expressed in dB, depending on the frequency. SPL indicates the strength of the noise source but not the direction. Generally, a reverberant noise field is assumed for the launcher, which means that the direction of the sound is insignificant and the sound is applied in all three directions.

Shock loads
Separation of stages, fairing, spacecraft or the DOC will produce very short duration loads in the internal structure of the DOC and is called shock loads. The response of the system to the shock loads is expressed in a shock response spectrum (SRS). SRS graphs an acceleration time history of the response and is expressed as acceleration in g versus frequency in dB.

Temperatures
Temperature variations usually cause high thermal stresses in structures. Thermal deformations are beyond the scope of this thesis and therefore their effects are not considered.

Random Loads
Random vibration is a motion, which is non-deterministic, meaning that future behaviours cannot be precisely predicted. This is due to the random characteristic of its excitation or input. In general, statistical or probabilistic approaches can be used to define the structural response to random vibration. In mathematical terms, random vibration is characterized as an ergodic and stationary process.

A measurement of the power spectral density (PSD) or the acceleration spectral density (ASD) is the way to specify random vibration. PSD is expressed in g^2/Hz and ASD is in $(m/s^2)^2/Hz$. The term PSD is used to specify a random vibration event, ASD is used in structural analysis. The loads are imposed in all three directions.

3.2. Load Analysis
User manuals of the three launchers and the S[&]T investigation on identification of suitable locations play the key role in defining the critical loads on each host stage. The imposed loads by the Ariane 5, Vega, and Soyuz are determined in Sections 3.2.1, 3.2.2, and 3.2.3, respectively.

3.2.1. Ariane 5
During the flight, the DOC is exposed to a variety of mechanical loads, which it should be able to withstand. In this section, the loads that are applied on the DOC once it is secured on each one of the locations of Ariane 5 launcher, selected in Section 2.2, is discussed.

Table 3.1: Longitudinal and Lateral Sine Excitation at Ariane 5 Base (Lagier, 2016)

Longitudinal		Lateral	
Frequency Band [Hz]	Sine Amplitude [g]	Frequency Band [Hz]	Sine Amplitude [g]
2 - 50	1.0	2 - 25	0.8
50 - 100	0.8	25 - 100	0.6

Due to aerodynamic forces and the propulsion system, the DOC experiences many static and dynamics loads. According to Lagier (2016), the highest longitudinal acceleration happens at the end of the solid rocket boost phase and does not exceed 4.55 g, while the highest lateral static acceleration experienced is up to 0.25 g. These numbers are applicable on all potential locations, since this event happens when all stages are still connected.

Additionally, up to a frequency of 100 Hz, the random environment is imposed by sine excitations. The maximum envelope of sinusoidal vibration levels at the Ariane 5 base in both, longitudinal and lateral directions are given in Table 3.1. This happens during the atmospheric power flight and therefore relevant for all locations.

Above a frequency of 100 Hz, the random environment excitation is produced by the acoustic loads. The DOC will experience the highest acoustic pressure fluctuations when firing the engines and while the launcher is experiencing aerodynamic force through the atmosphere. Since acoustic loads are produced once the main cryogenic stage and the upper composite are still connected to the bottom part of the launcher, these loads are applicable to both stages. The acoustic noise spectrum envelope of Ariane 5 is shown in Figure 3.1. The SPL in dB is plotted in frequency band between 25 to 2900 Hz.

Furthermore, Ariane 5 is subjected to a significant shock during the next events:

- UC stage separation from the EPC;

- The fairing jettisoning;

- The spacecraft separation.

In Ariane 5's user manual, it is reported that the shocks generated by the separation of the UC from the EPC and the fairing jettison are below the shock from the spacecraft separation. However, the DOC will not be placed on the upper stage for the reason discussed in Section 2.2 and hence the shock imposed by spacecraft separation will not be applied on the DOC. Furthermore, as explained in Section 2.2, before the fuel of the EPC stage runs out, the fairing will be jettisoned at an attitude of 107 km and a velocity of 2.4 km/s. Since, the DOC is still mounted on either the EPC or UC, the shocks imposed by this jettisoning will still be felt by the DOC . The shock spectrum envelope of fairing separation shock and launch vehicle stage separation shock are 0.2 times the frequency. The shock spectrum envelope is computed in a frequency bandwidth of 25-2500 Hz (Lagier, 2016).

3.2.2. Vega

The highest longitudinal acceleration occurs just before the third-stage cut-off and can be as much as 7 g. Since at that moment the Zefiro 9 and Attitude and Vernier Upper Module (AVUM) are still connected, this value is relevant for all selected locations listed in Section 2.3. The highest lateral static acceleration occurs at maximum dynamic pressure (at the beginning of the lift-off phase) and takes into account the effect of wind and gust encountered in this phase. This will reach 0.9 g (Perez, 2014).

According to Perez (2014), up to a frequency of 125 Hz, the random environment excitation is imposed by sine excitations. The maximum envelope of sinusoidal vibration levels of the Vega is given in Table 3.2. This table shows the sine amplitude versus four frequency bands in the longitudinal and lateral directions. This happens during the atmospheric power flight and therefore relevant for all locations.

Above a frequency of 125 Hz, the random environment excitation is produced by the acoustic loads. The DOC
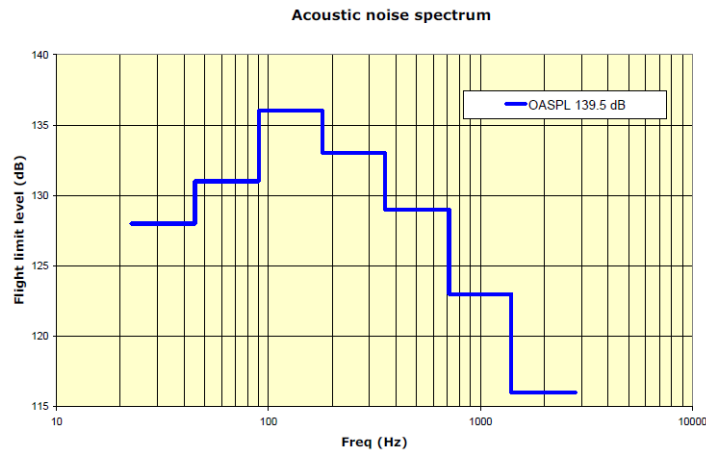
Figure 3.1: Acoustic Noise Spectrum of Ariane 5 (Lagier, 2016)

Table 3.2: Longitudinal and Lateral Sine Excitation of Vega (Perez, 2014)

Longitudinal		Lateral	
Frequency Band [Hz]	Sine Amplitude [g]	Frequency Band [Hz]	Sine Amplitude [g]
1 - 5	0.4	1 - 5	0.4
5 - 45	0.8	5 - 45	0.5
45 - 110	1.0	45 - 110	0.5
110 - 125	0.2	110 - 125	0.2

will experience the highest acoustic pressure fluctuations during lift-off while the launcher is going through the atmospheric phase. Since acoustic loads are produced while all stages are still connected, these loads are relevant for all locations in Section 2.3. The acoustic noise envelope spectrum is shown in Table 3.3 (Perez, 2014).

Furthermore, European Launch Vehicle (ELV) performed an analysis on acoustic loads to define the qualification loads on board of the Vega. ELV defines two new locations at AVUM stage, the AVUM part and bottom part of the Vega Secondary Payload Adapter (VESPA). ELV presented in a technical report, *VG-SG-1-C-040-SYS*[3], to S[&]T, the PSD of these two locations. Figure 3.2 illustrates the PSD graph of the bottom part of VESPA (from now refers only as the VESPA) versus frequency, and Figure 3.3 plots the PSD graph of the AVUM versus frequency. Note that these values are the qualification numbers and hence the required safety factor is included.

Additionally, ELV reported in the latter report that Zefiro 9 is exposed to high random vibrations. The source of the event is missing in the report, but it is emphasized that only Zefiro 9 is exposed to this load. The random vibration loads applied on the Zefiro 9 is plotted in Figure 3.4 in PSD versus frequency.

3.2.3. Soyuz
Like in the case of the other previous launchers, during the ascent phase, the DOC is subjected to static and dynamic loads. The highest longitudinal acceleration takes place just before the first stage cut-off and does not exceed 4.3 g. The highest lateral static acceleration can be reached up to 0.4 g at maximum dynamic pressure. The effects of the environment in this phase, like wind and gusts are included. Since the maximum occurs before the first stage cut-off, these values are applicable for the DOC regardless of its location on the stages (Perez, 2012).

The envelope of the sinusoidal vibrational levels at the DOC do not exceed the values in Table 3.4. Sinusoidal excitations affect the launch vehicle during its powered and atmospheric flight, therefore these values are applicable to the DOC regardless of its location (Perez, 2012).

---

[3]VG-SG-1-C-040-SYS, Iss. 5-Rev. 1. This is a classified document and only available through S[&]T.

Table 3.3: Acoustic Noise Spectrum at Vega (Perez, 2014)

Octave center frequency [Hz]	Flight limit level [dB]
31.5	112
63	123
125	126
250	135
500	138
1000	127
2000	120
OASPL (20-2828 [Hz])	140.3

Figure 3.2: Power Spectral Density of the Bottom Part of VESPA (*VG-SG-1-C-040-SYS* File)
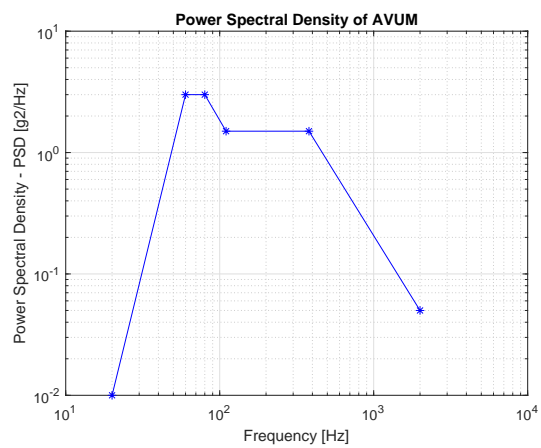
Figure 3.3: Power Spectral Density of AVUM (*VG-SG-1-C-040-SYS* File)
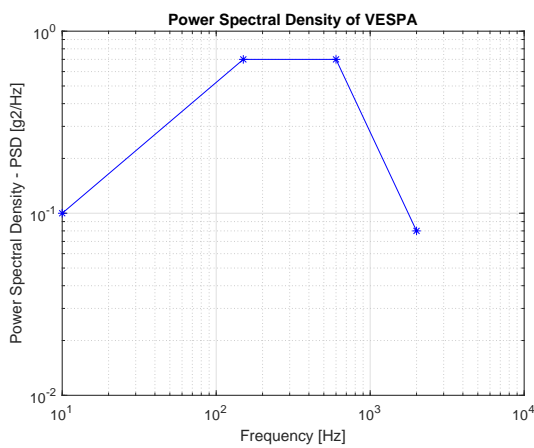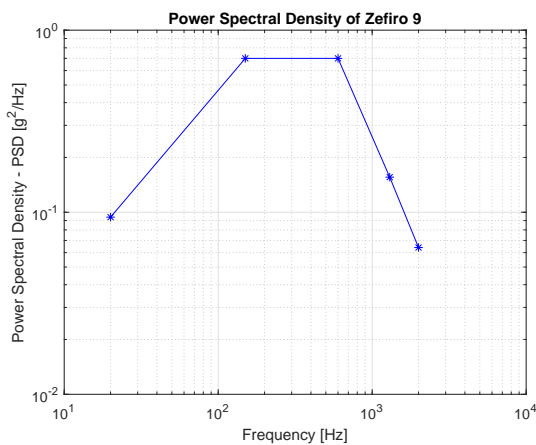

Figure 3.4: Power Spectral Density of the Zefiro 9
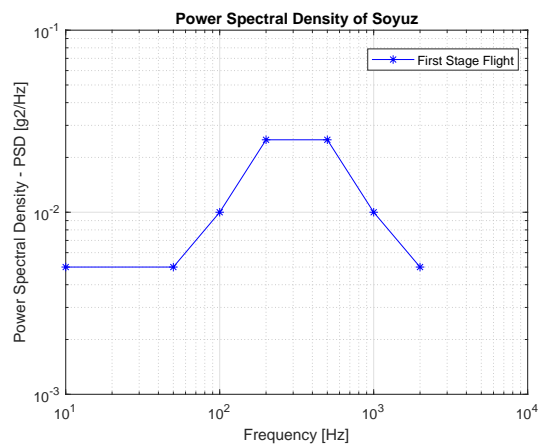
Figure 3.5: Random Vibration of Soyuz (Perez, 2012)

Table 3.4: Longitudinal and Lateral Sine Excitation at Soyuz Base

Longitudinal		Lateral	
Frequency Band [Hz]	Sine Amplitude [g]	Frequency Band [Hz]	Sine Amplitude [g]
1 - 5	0.4	1 - 5	0.4
5 - 10	0.5	5 - 10	0.6
10 - 20	0.8	10 - 20	0.6
20 - 30	0.8	20 - 30	0.4
30 - 40	0.5	30 - 40	0.4
40 - 60	0.5	40 - 60	0.3
60 - 100	0.3	60 - 100	0.3

Additionally, during the first stage phase, vibration will be excited by the propulsion system and by the adjacent structure's vibro-acoustic response of Soyuz. Random vibration of Soyuz is illustrated in Figure 3.5 in the PSD versus frequency (Perez, 2012).

3.3. Load Computation

As it was shown in previous sections, the unit of the loads were different. To be able to compare the loads to identify the sizing load per location, the loads should be converted into the same unit. As will be explained in Chapter 6, the loads need to be converted into a static inertial load, in this section the methods that are used are explained. In Section 3.3.1, the Spann method, which derives the vibration for structures subjected to an acoustic load is discussed. Then, in Section 3.3.2, Miles' equation is defined, which converts random vibration response into a static load. Finally, converting PSD into ASD or vice versa and converting G_{rms} into acceleration or vice versa is explained in Section 3.3.3.

Acoustic loads can be converted into the random vibration using the Spann method and subsequently be converted into a static inertial load using the Miles' equation method. For random loads, only Miles' equation is needed to convert them into static inertial loads.

3.3.1. Spann Method

Four methods are proposed by ESA-ESTEC (2013): 1) specifications derived from random and vibro-acoustic test data developed by Girard et al. (1989); 2) the VibroSpec method reported by Kasper et al. (1989); 3) the test/analysis extrapolation method, and 4) the Spann method described by Spann and Patt (1984); Schaefer (1997).

The first method is based on a statistics analysis performed on test data of nine European satellites: METEOSAT, MARECS, ISPM, ECS, GIOTTO, TELECOM-I, SPOT, HIPPARCOS, and OLYMPUS. The results of this method are frequency response curves relating the mass to the PSD response of Ariane 4 and Ariane 5 launchers. The second method, VibroSpec method, reviewed and improved the first method by collecting data from in total 37 spacecraft missions. This method can be used in the early stage of a project, and relates the mass to the PSD. The third method is based on mounting the satellite on the launchers and determining the in-flight random responses. The fourth method can provide a sufficient estimation of the vibration response, when the areas exposed to the acoustic environment and the mass of the satellite are known.

The third method is eliminated, since testing is not possible. The second method is more accurate than the first approach since more data is used, therefore, the first method is eliminated too. Finally, the Spann method provides a better estimation than the second method. The mass and the DOC's dimensions are known, hence the Spann method can be used. Due to these two reasons, the Spann method is selected and the steps required in the Spann method to derive the vibration for a typical spacecraft structure subjected to an acoustic environment is described using ESA-ESTEC (2013) manual.

Acoustic environment is defined as sound pressure levels (SPL) in dB and will be converted to PSD by this

method. The SPL is defined as:

$$SPL = 10\log\left(\frac{p}{p_{\text{ref}}}\right)^2 \tag{3.1}$$

where p is the mean square pressure in a certain frequency band with a frequency bandwidth of Δf, usually one-octave or one-third-octave band. p_{ref} is the reference pressure in Pa.

The x-th octave band of two subsequence frequencies f_{min} and f_{max} is:

$$\frac{f_{\text{max}}}{f_{\text{min}}} = 2^x \tag{3.2}$$

where x defines the octave number band, x=1 for one-octave and x=1/3 for the one-third-octave band. f_{min} and f_{max} are the minimum and maximum frequency, respectively.

Furthermore, the centre frequency can be defined as:

$$f_c = \sqrt{f_{\text{min}} f_{\text{max}}} \tag{3.3}$$

where f_c is the centre frequency in Hz.

The frequency bandwidth Δf is given:

$$\Delta f = f_{\text{max}} - f_{\text{min}} \tag{3.4}$$

Expressing the frequency bandwidth Δf in terms of the centre frequency by substituting the Equations 3.2 and 3.3 into Equation 3.4:

$$\Delta f = \left(2^{\frac{x}{2}} - 2^{\frac{-x}{2}}\right) f_c \tag{3.5}$$

for

- one-octave band width, x=1, thus: $\Delta f = 0.7071\, f_c$;

- one-third-octave width, x=1/3, thus: $\Delta f = 0.2316\, f_c$.

The pressure power spectral density field defined as $W_P(f_c)$ (in Pa^2/Hz) in the frequency band with centre frequency f_c, bandwidth $\Delta f(f_c)$ and pressure p(f_c) is defined as:

$$W_p(f_c) = \frac{p^2(f_c)}{\Delta f(f_c)} \tag{3.6}$$

where the root mean square pressure p_{rms}^2 is given as:

$$p_{rms}^2 = \int_0^\infty W_p(f_c)\,df = \sum_{i=1}^k W_{p,i}(f_c)\Delta f = \sum_{i=1}^k p_i^2(f_c) \tag{3.7}$$

where k stands for the number of octave bands.

Substituting Equations 3.1 and 3.7 into Equation 3.6, the SPL can be converted to W_p by:

$$W_P(f_c) = \frac{p_{rms}^2(f_c)}{\Delta f_c} = p_{ref}^2 \frac{10^{\frac{SPL(f_c)}{10}}}{\Delta f_c} \tag{3.8}$$

The equivalent response PSD is:

$$PSD = \beta^2 Q^2 \left(\frac{A}{gM}\right)^2 W_p(f_c) \tag{3.9}$$

where g is the gravitational acceleration and is equal to 9.8 m/s^2, A stands for the area of the support structure, M is the total mass of the DOC, ESA-ESTEC (2013) reported a β factor of 2.5, and an amplification factor (Q) of 4.5 based on experimental tests.

Table 3.5: CSG Safety Regulations (Lagier, 2016; Perez, 2014, 2012)

Load	Qualification Factor
Steady-state loads	1.25
Sine vibration	1.25
Acoustics	+3 dB
Shock	+3 dB

3.3.2. Miles' Equation

To find an approximated solution of the random vibration response, the Miles' equation is used to convert the PSD into a static load. This method assumes a single degree of freedom behaviour of a structure. This means that this method limits the elastic behaviour (ESA-ESTEC, 2013).

The root mean square acceleration (G_{rms}) is equivalent to the square root of the area under the curve of the PSD response curve with the unit g^2/Hz. Therefore:

$$G_{rms} = \sqrt{\int [\text{PSD}_{input}] T^2 df} \tag{3.10}$$

For a band limited spectrum, Equation 3.10 can be simplified to:

$$G_{rms} = \sqrt{\frac{\pi}{2} f_n T [\text{PSD}(f_n)]} \tag{3.11}$$

where, f_n is the natural frequency of the DOC, T is the transmissibility at f_n and is defined as $T = \frac{1}{2\zeta}$, $\text{PSD}(f_n)$ is the value of the input acceleration PSD at frequency f_n, and G_{rms} is in g load unit (Miles, 1954). S[&]T reported a value $\zeta = 0.010$ based on previous tests.

3.3.3. Converting PSD to ASD and G_{rms} into Acceleration

PSD can be converted into ASD by:

$$ASD = PSD \times 9.81^2 \tag{3.12}$$

The maximum root mean stress provides a criterion for reliability and therefore ESA-ESTEC (2013) states that a 3-σ rule should be used for safety factor. Additionally, G_{rms} is in g-load unit and to compute the acceleration a in m/s^2 including the safety factor:

$$a = 3 \times 9.81 \times G_{rms} \tag{3.13}$$

3.4. Implementing Loads

The loads imposed by the launcher and the methods to convert them to the static loads have been discussed in the previous sections. In this section, the critical and sizing loads per location are investigated for all three launchers and their stages. First, the safety factor for the loads is explained in Section 3.4.1. After that, all loads are converted to acceleration and the critical load per section is selected. Ariane 5, Vega, and Soyuz loads per part is discussed in Sections 3.4.2 to 3.4.4, respectively.

3.4.1. Safety Factor

To meet the DOC qualifications, the design limit load factors needs to be increased. This means the loads given in Sections 3.2.1 to 3.2.3 needs to be increased by a safety factor. All three launchers require the same safety regulation of ESA called the Centre Spatial Guyanais (CSG). Therefore, the DOC should also be in conformity with these safety regulations. The safety factors of CSG are given in Table 3.5 for steady-state loads, sine vibration, acoustic, and shock excitations.

3.4.2. Ariane 5

The loads given in Section 3.2.1 are further increased by using the the safety regulations from Table 3.5. Comparing the loads shows that the steady-state loads and sine vibration are much lower than acoustic vibration and shock. Therefore, steady-state loads and sine vibration are eliminated from further investigation.
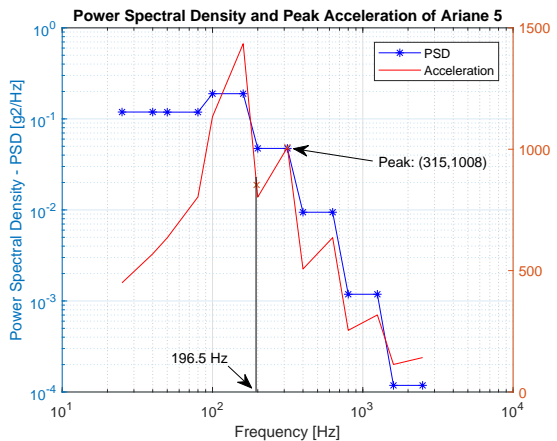
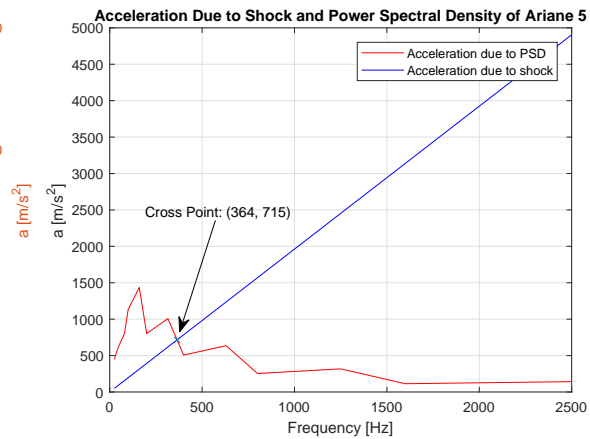Figure 3.6: Results of Converting SPL to PSD and Acceleration of Ariane 5

Figure 3.7: Comparing the Acceleration Due to Shock Load and SPL of Ariane 5

In the Ariane 5 user manual is stated that the SPL values of Ariane 5 are defined in the one-octave band. The acoustic loads including a 3 dB safety factor is converted into PSD and then acceleration using methods in Section 3.3.1 and Section 3.3.2, respectively. The results are plotted in Figure 3.6. On the left side of the plot, the PSD is plotted against frequency and on the right side the acceleration versus frequency. Note that in all plots of the PSD and peak acceleration, the first natural frequency of the DOC is indicated and crossed the acceleration line. Furthermore, the next peak acceleration after the first DOC's natural frequency is pointed out by a cross-shape.

Furthermore, the acceleration of the shock load and the SPL are compared in Figure 3.7. The results show that the acceleration due to the SPL is higher till the frequency of 364 Hz. As will be explained in Section 5.2, the first natural frequency will occur at 196.5 Hz. Since acceleration of SPL in the first four modes is higher than the acceleration due to the shock, hence, it could be concluded that the acceleration imposed by SPL is higher than the shock load and thus SPL becomes the sizing acceleration.

3.4.3. Vega
The loads identified in Section 3.2.2 are increased by using the safety regulations from Table 3.5 and converted into accelerations. After comparing the loads, it is concluded that the steady-state loads and sine vibration are much lower than random vibration loads.

In the Vega user manual is stated that the SPL values of Vega are defined in the one-octave band. The acoustic load of Vega including the safety factor is converted into PSD and then acceleration using the methods described in Section 3.3.1 and Section 3.3.2, respectively. The results are shown in Figure 3.8. On the left side of the graph, the PSD is sketched versus the frequency and on the right side the acceleration versus the frequency bandwidth.

Additionally, for the Zefiro 9, VESPA, and AVUM, their PSD's are converted into accelerations and the plots are illustrated in Figure 3.9, Figure 3.10, and Figure 3.11, respectively. For all locations in Section 2.3, the results of acoustic pressure fluctuations (results from Figure 3.8) are valid. Except for the three latter locations, the PSD's are much higher and therefore are defined as sizing loads for those locations.

3.4.4. Soyuz
Again, the same method has been used to identify the most critical load. The PSD of Soyuz from Figure 3.5 is converted into acceleration. Comparing the results of all applied loads, it has been found that the PSD is highest and therefore it is selected as the sizing load for both locations. The plot is shown in Figure 3.12.
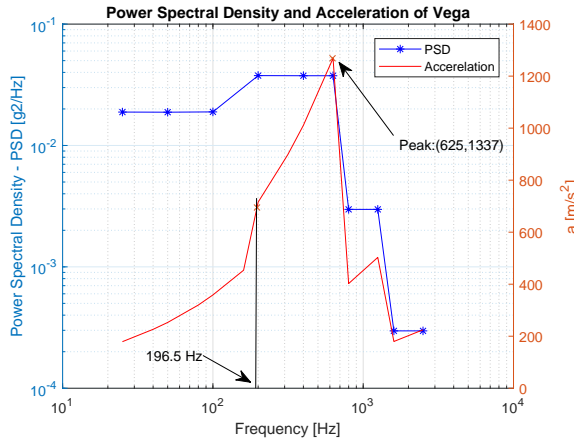
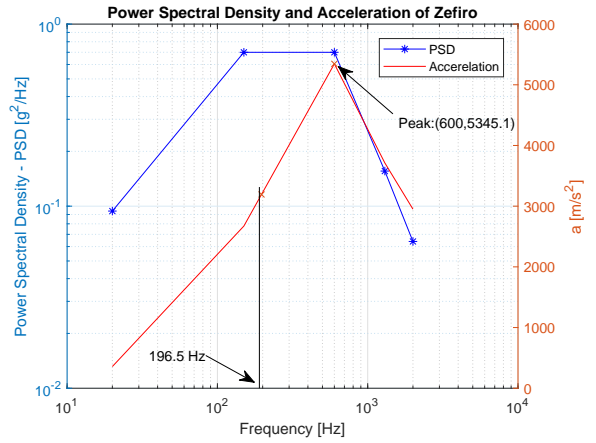Figure 3.8: SPL to PSD and Acceleration of Vega

Figure 3.9: PSD into Acceleration of Zefiro 9
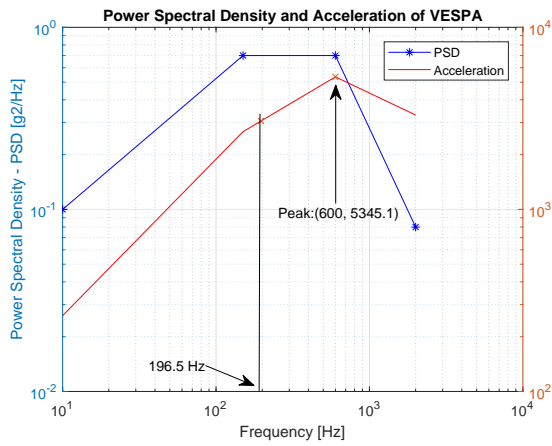
Figure 3.10: PSD into Acceleration of the Bottom Part of VESPA
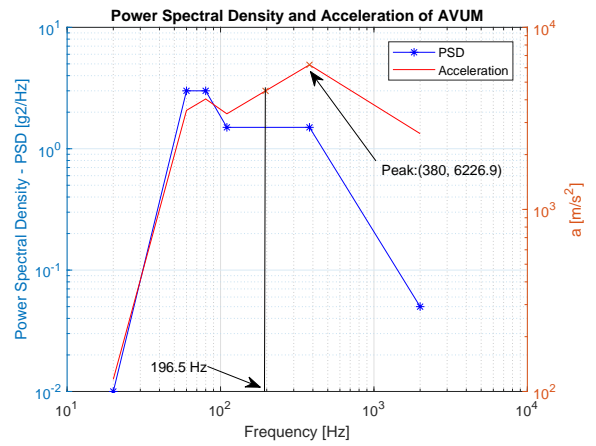
Figure 3.11: PSD into Acceleration of the AVUM
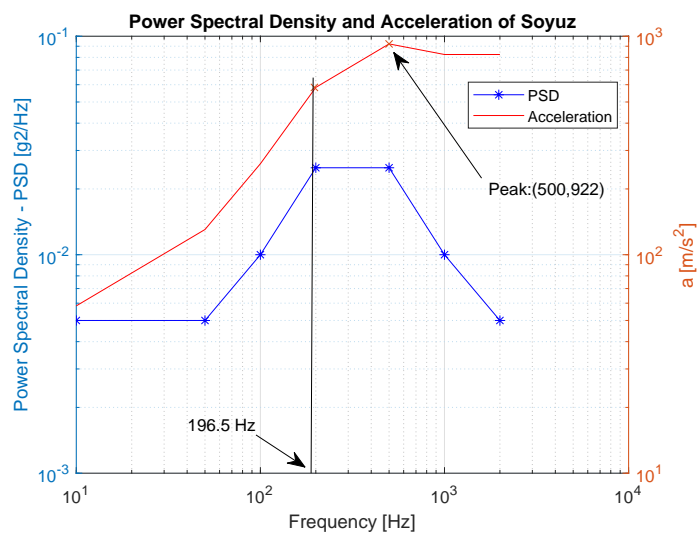
Figure 3.12: Results of Converting SPL to PSD and Acceleration of Soyuz

4

DOC Model

This chapter contains the description of the Demise Observation Capsule (DOC) layout including the subsystems and interface with the host vehicle. First, Section 4.1 will explain reference frames and the implementation of the DOC. Then, the physical layout of DOC will be described in Section 4.2. Finally, the model of DOC is explained in Section 4.3.

4.1. Reference Frames

The position and the orientation of the DOC needs be identified with respect to a reference frame. All reference frames in this section are presented by three orthogonal right-hand ruled axis through the origin of its reference frame. Here, the theory of all reference frames will be defined using the theory propounded in Mulder et al. (2013).

A geometric reference frame on the launcher is defined by the launcher authorities in the user manual of the launchers. These reference frames are used to express the launcher's position and velocity in its orbit with respect to the Earth Centered Inertial (ECI) reference frame. The loads imposed on the launchers are defined with respect to the launcher geometric reference frame. More details are explained in Appendix A.2. Additionally, two geometric reference frames that are selected for this thesis will be remain fixed to the body in case of any perturbation.

The DOC geometric-fixed reference frame is fixed to the DOC vehicle and is illustrated in Figure 4.1. This reference frame serves as a main reference frame of DOC model and the DOC's subsystems will be described with respect to this frame. This reference frame is defined below.

- The origin is located on the symmetrical axis of the capsule on top of the front shell;

- The z_{DOC}-axis is pointing inside of the capsule and along the symmetry axis of the DOC;

- The x_{DOC}-axis is pointing to the direction of communication antenna and also in the same direction as the x-axis of the launcher.

- The y_{DOC}-axis is aligned with the separation nuts.

The host vehicle interface (HVI) geometric-fixed reference frame is fixed to the HVI and is shown in Figure 4.2. This will be used to define the position of the HVI with respect to the capsule shape. Its coordinate system is defined as follows:

- Its origin is located on the interface between the host vehicle and the HVI;

- Its z_{HVI}-axis is along the symmetry axis of the HVI oriented towards the host vehicle;

- Its x_{HVI}- and y_{HVI}-axis are completing the frame.
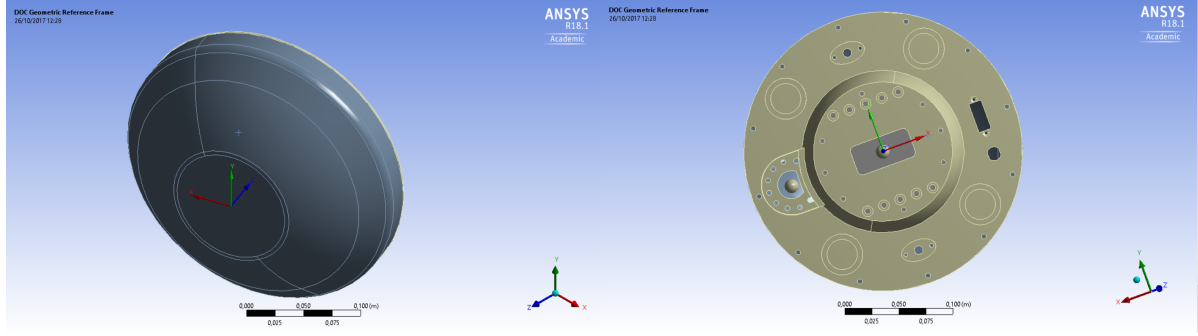
Figure 4.1: DOC Geometric Reference Frame
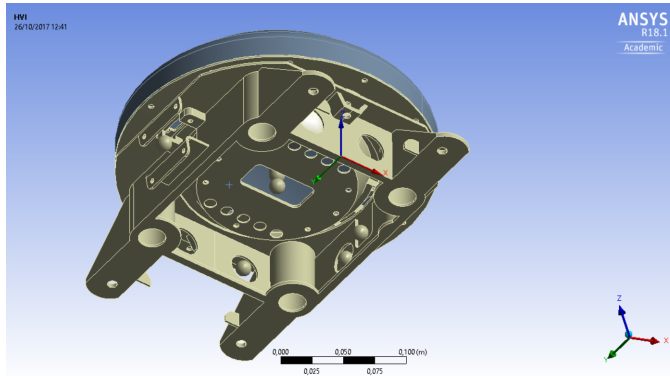
Figure 4.2: Host Vehicle Interface Geometric Reference Frame

To transform the HVI geometric-fixed reference frame to the DOC geometric-fixed reference frame, two rotations and a transformation are required. First, by rotating about the z_{HVI}-axis by 180° and then by the same amount about its x_{HVI}-axis. Then transformation of the coordinates [73.584; -8.9; 74.712] cm into their new coordinates.

$$\begin{bmatrix} x_{DOC} \\ y_{DOC} \\ z_{DOC} \end{bmatrix} = T_z(\pi) T_x(\pi) \begin{bmatrix} x_{HVI} \\ y_{HVI} \\ z_{HVI} \end{bmatrix} = \begin{bmatrix} 1 & 0 & 0 \\ 0 & \cos(\pi) & \sin(\pi) \\ 0 & -\sin(\pi) & \cos(\pi) \end{bmatrix} \begin{bmatrix} \cos(\pi) & \sin(\pi) & 0 \\ -\sin(\pi) & \cos(\pi) & 0 \\ 0 & 0 & 1 \end{bmatrix} \begin{bmatrix} x_{HVI} \\ y_{HVI} \\ z_{HVI} \end{bmatrix} = \begin{bmatrix} -1 & 0 & 0 \\ 0 & 1 & 0 \\ 0 & 0 & -1 \end{bmatrix} \begin{bmatrix} x_{HVI} \\ y_{HVI} \\ z_{HVI} \end{bmatrix}$$

(4.1)

4.2. Layout of DOC Configuration

DOC prototype is already built for a worst-case load scenario of some selected locations (Section 1). S[&]T and its subcontractors reported the layout of the DOC in several internal reports, among others: *Aerothermodynamics, thermal and structural design, definition and justification file*, *Concept design definition and justification*, and *Shape detailed design and detailed configuration*[1]. In this section, the DOC configuration will be summarized.

DOC is a small capsule with a diameter of 325 mm and a mass limit of 10 kg including the HVI part, and the separation mechanisms. This capsule is designed for aerodynamic stability issues and thermally qualified to re-enter the Earth. A thermal protection system (TPS) is designed to protect the DOC capsule as well as the HVI part. The HVI-TPS consists of two pieces, while DOC-TPS consists one piece.

The DOC will be mated to the host vehicle through its back part in order to have the front heat shield free from interfaces and make the DOC possible to perform re-entry. Due to the agreement with the launch vehicle providers, the host vehicle interface will be bolted to an aluminium flat adapter by four M5 steel screws.

---

[1]These are three classified documents and only available through S[&]T.

The aluminium adapter will directly be bolted to the host vehicle.

The DOC system is illustrated in Figure 4.3 with its parts and their functions explained.

Internal TPS: The internal TPS is made of materials with convenient thermal properties. This part houses and protects the avionic.

Ballast: The ballast is a disk of tungsten, which allows the center of gravity point to be in the foremost possible position to meet the aerodynamic requirements.

Back Shell: This part connects the host vehicle to the front shield and avionics. The avionic system is bolted by ten screws to the back shell. The material used to produce this part is titanium alloy.

Front Shell: The front shell will be mated to the back shell by twelve screws and will accommodate the ballast mass and sensors. Like the back shell, this part is made of titanium alloy.

Front and Back Shield: The front and back shield are to protect the DOC from high temperatures and make it aerodynamically suitable for re-entry. The front shield is glued to the front shell and the back shield to the back shell.

Host Vehicle Interface: The HVI is connected to the back part of the main body and on the other side is affixed to an aluminium shell, which is mounted on the host vehicle. The HVI will be fastened to the host vehicle by means of a number of screws, which is implied by the launcher authorities. The HVI provides structural stiffness and accommodates all the needed elements like separation springs, HVI camera, and electrical connectors, etc.

The HVI accommodates the screws of the separation mechanism and equips four springs inserted in cylindrical cavities, required for the separation of the capsule. The size of the springs is already computed for the release phase and therefore cannot be changed. Hence, the size including the diameter and length of the cavities is fixed during the optimization process. The HVI shall be protected by a dedicated TPS mounted on the HVI itself.

Avionics: Avionics and instruments form the brain of the DOC. Due to the harsh environment at space, this sensitive part of the payload will be protected by locating them in the internal TPS. In addition to that, avionics have a camera and an antenna attached to various places within the DOC.

4.3. Describing the DOC Model

Structural analysis is a process to analyse a structural system to predict its responses and behaviours by using physical laws and mathematical equations. The model of DOC should be close to the actual structure to validate the physical DOC model. Considering the complexity of DOC structures, the response behaviour can not solely be done analytically. Therefore, Finite Element Method (FEM) is used to compute an approximate result.

Section 4.3.1 describes this FEM approach briefly. Then Section 4.3.2 describes the model of DOC. The contacts between the parts are described in Section 4.3.3, which defines whether the body is somewhere fixed or can freely vibrate. The material properties that are usually used for an elastic analysis are explained in Section 4.3.4. Finally, Section 4.3.5 defines a proper mesh size by performing a mesh convergent analysis.

4.3.1. Finite Element Method

Modelling is based on a variety of numerical methods, such as FEM, Finite Difference Method, and Boundary Element Method, etc. among which FEM is the most popular numerical approach, which reduces the degree of freedom from infinite to finite by discretization. The domain Ω is divided into a number of N 3-dimensional simple elements E_i in the shape of either tetrahedrons or cubes depending on the domain shape. The elements are placed in such a manner that they do not overlap nor there is empty space between
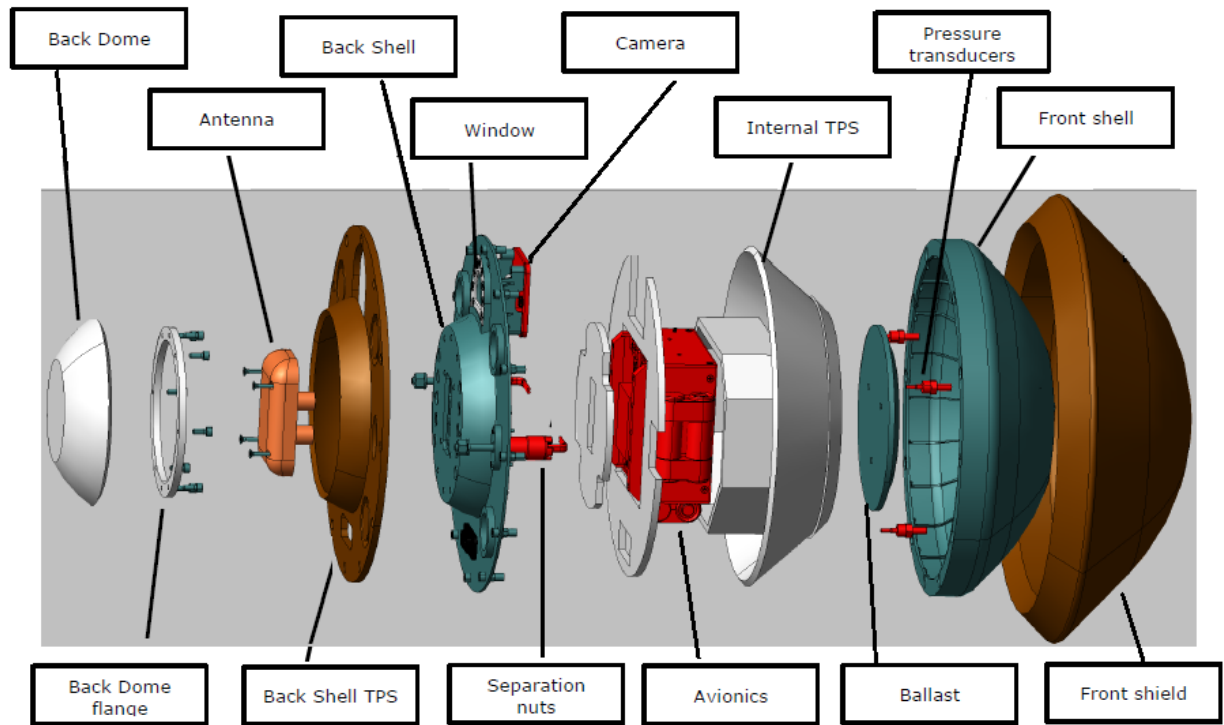
Figure 4.3: DOC Configuration Including Its Subsystems (S[&]T Internal Report)

them (Hollauer, 2007).

$$\Omega = \bigcup_{i=1}^{N} E_i \qquad \forall i \neq j \quad ; \quad Int(E_i) \cap Int(E_j) = 0 \tag{4.2}$$

where i varies between 1 to N; Int(E_i) defines the set of all points in the element E_i, exclusive those are on the surface. E_i are connected to each other at nodal points forming a mesh. The FEM reduces all the relevant material properties, such as elasticity and shear moduli, to values assigned to the nodes of the mesh and the results of the model are the displacement of the nodes and the forces acting between them. Figure 4.4 shows the DOC in FEM environment.

4.3.2. Describing the Model in the Software

The physical DOC configuration can be divided into two categories, the load carrying structures, which determine its strength and stiffness, and the non-load carrying structures. The load carrying elements of the DOC will be represented by a discrete model. While, the elements which do not contribute to the stiffness of the structure are treated as non-structural mass (Ley et al., 2009). Modelling as non-structural mass will simplify the model, however it can cause a lower natural frequency than the actual frequency due to the fact that the software does not take the non-structural rigidness into account.

The DOC is modelled in ANSYS^{TM} as following. The next four parts are modelled as discretized volumes:

- Front shell;

- Back shell;

- Host vehicle interface;

- Ballast.

These parts are taking all the loads applied on the DOC and define DOC's strength. The rest of the DOC subsystems are modelled as non-structural lumped masses, since they do not contribute to the stiffness. As already explained in Section 4.2, they are located in the DOC to either protect DOC against heat, or they are instruments and are required to perform the mission.

Figure 4.4: Meshed DOC in ANSYS^{TM} Environment

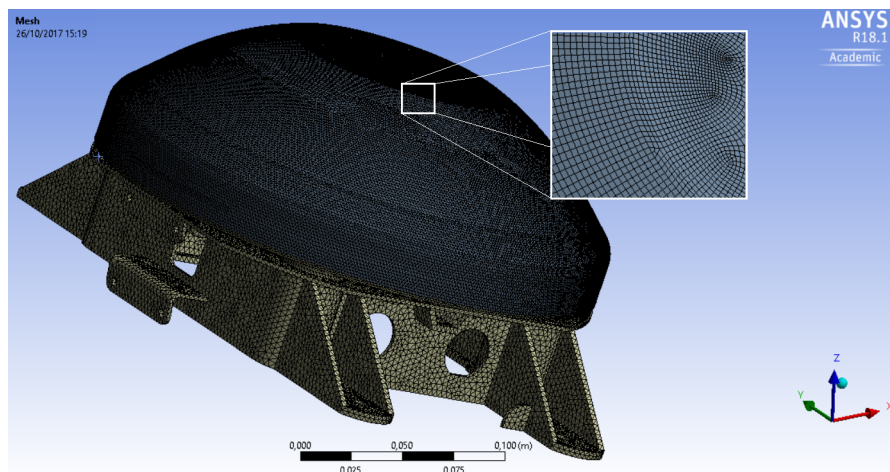Table 4.1: List of Lumped Masses, Their Characteristics, and Their Location on the DOC

Item	Subsystem	Mass [kg]	Contact		Coordinates [mm]		
			Body	Edge	X	Y	Z
1	Antenna	0.140	Back Shell	4	746.67	1.35e-8	778.40
2	Camera	0.072	Back Shell	4	847.63	-1.29e-2	792.80
3	Avionics	1.400	Back Shell	10	751.90	2.53e-8	793.50
4	HVI Camera	0.072	HVI	4	638.80	-7.13e-3	804.00
5	Front Shield	0.890	Front Shell	4	767.10	4.87e-7	837.40
6	Back Shield and Dome	0.220	HVI	4	750.45	2.30e-6	789.33
7	HVI TPS 1	0.810	HVI	2	667.55	2.98e-5	796.69
	HVI TPS 2	0.810	HVI	2	820.16	1.30e-6	743.84
8	DBAS 1	0.090	HVI	2	771.85	89.0	762.03
	DBAS 2	0.090	HVI2	2	823.37	28.0	737.87

The centre of gravity of the on-structural lumped masses are not directly located on the discretized volumes, therefore these eight non-structural lumped masses are modelled as remotely attached lump masses. In order to define the lumped masses in ANSYS^{TM}, their mass, location in x-, y-, and z-axis with respect to the DOC geometric-fixed reference frame, their contact body, and their edge contact regions should be defined in the model. Table 4.1 lists these inputs and they are illustrated in Figures 4.5 to 4.12. All subsystems are already described in Section 4.2, except the electrical cables, DBAS 1 and 2.

4.3.3. Connections
The type of connections define the translational and rotational component of the displacement. In this section, the connections are divided by internal and external conditions. The internal contacts define the constrains between the subsystems of the DOC. External boundary conditions define the constrains between the DOC and host vehicle.
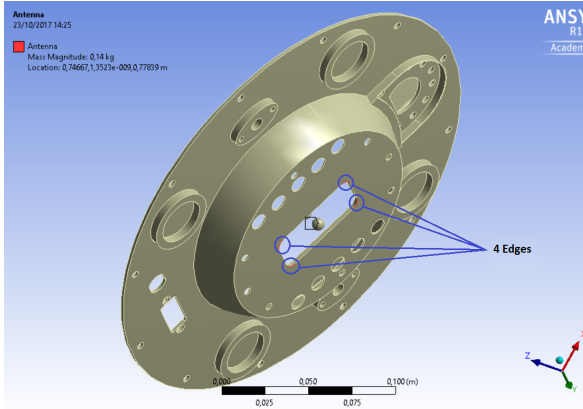
Figure 4.5: Antenna Point Mass and 4 Edges Connection Regions
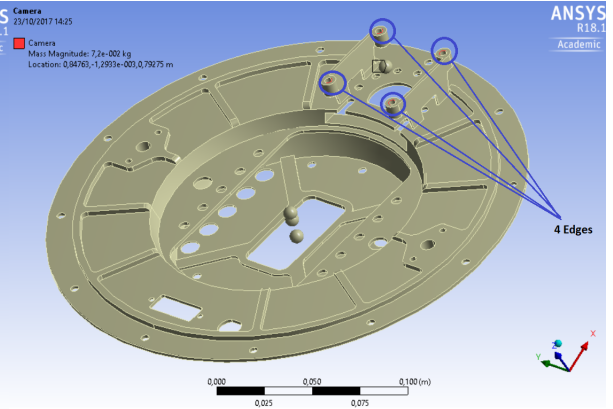
Figure 4.6: Camera Point Mass and 4 Edges Connection Regions
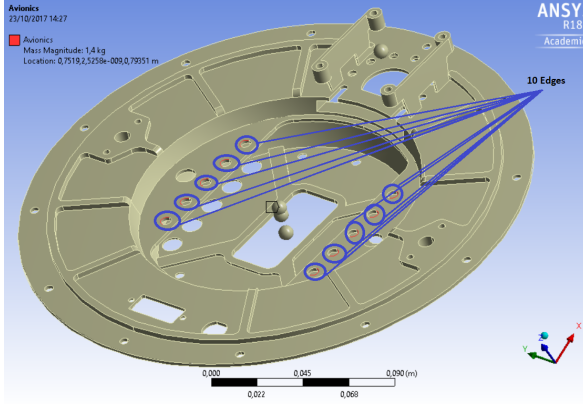
Figure 4.7: Avionics Point Mass and 10 Edges Connection Regions
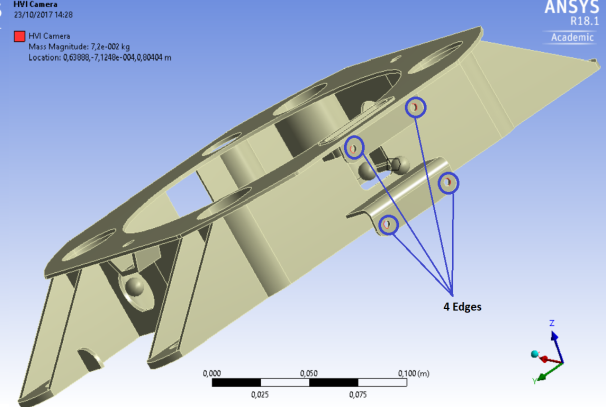
Figure 4.8: HVI Camera Point Mass and 4 Edge Connection Regions
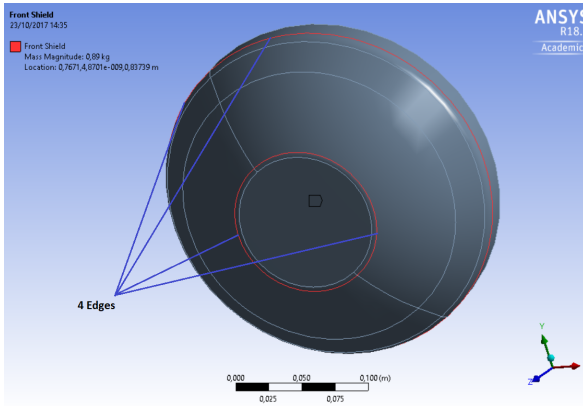
Figure 4.9: Front Shield Point Mass and 4 Edges Connection Regions

Figure 4.10: Back Shield and Dome Point Mass and 4 Edges Connection Regions

(a) HVI TPS 1 Point Mass and 2 Edges Connection Regions
(b) HVI TPS 2 Point Mass and 2 Edges Connection Regions

Figure 4.11: HVI TPS 1 and 2 and Their Connection Regions

(a) DBAS 1 Point Mass and 2 Edge Connection Regions
(b) DBAS 2 Point Mass and 2 Edge Connection Regions

Figure 4.12: DBAS 1 and 2 and Their Connection Regions

Internal

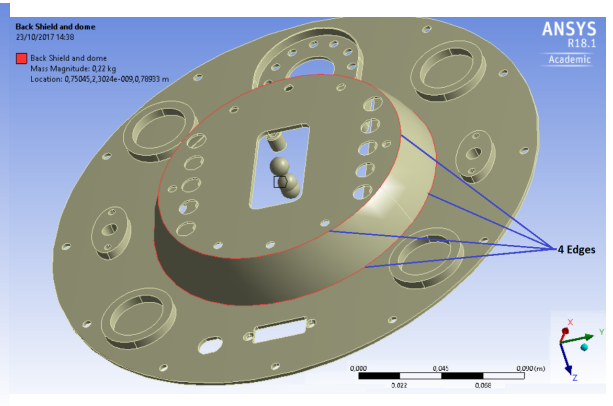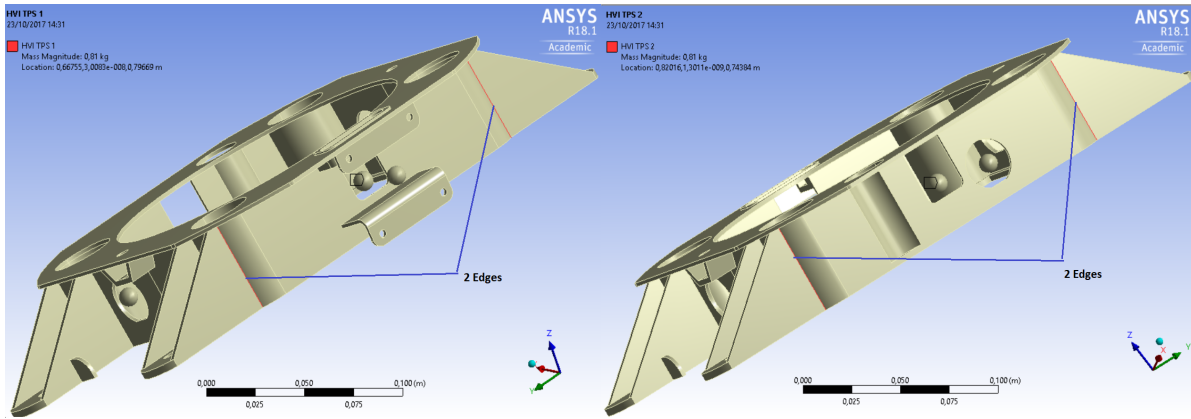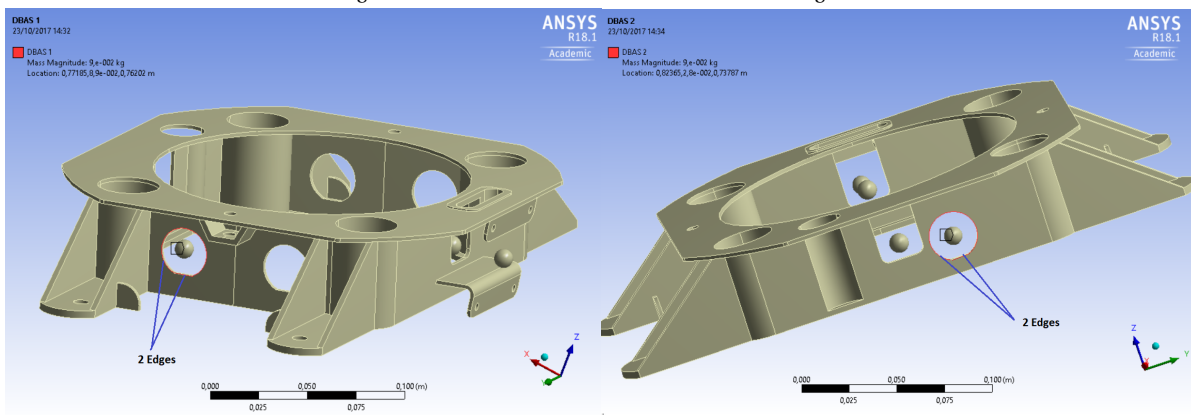In order to model the internal connections, a study was conducted to define what the software has to offer. In ANSYS^{TM}, the connection is defined by a pair called contact and target area. There are several contacts (ANSYS, 2010):

- Bonded;

- No separation;

- Frictionless;

- Rough;

- Frictional.

In the modelling of DOC, bonded and frictionless contacts are selected according to the physical properties of the connections and will be explained more in details.

Bounded contact: This is a special case of contact analysis and can be applied to all contact regions. Once no sliding or separation between faces or edges is allowed, the contact regions can be modelled as bonded. This is the result of gluing the contact regions. This type of contact allows for a linear solution since the contact area will not change during the application of the load.

Frictionless contact: This setting models standard unilateral contact, this means the normal pressure is equal to zero if separation occurs. Thus gaps can form in the model between bodies depending on the loading. This solution is non-linear because the area of contact may change as the load is applied. Here, a free sliding is allowed meaning that the coefficient of friction, μ, in Coulomb's Law is assumed to be zero (Popov, 2010).

The DOC part contacts are as follows:

1. The ballast is glued on the internal surface of the front shell;

2. The front shell is fixed to the back shell along the contact circular surface by twelve screws;

3. The back shell is glued to the HVI in by the two contact surfaces around the separation nuts;

4. The back shell is connected to the HVI in by four contact regions around the four separation springs. These bodies can slide relative to one another without any resistance.

In ANSYS^{TM} the first three contacts are selected as bonded contacts since the contact areas are either glued or fixed by screws. The last contact is selected as a frictionless contact region, since it allows gaps between the two bodies. Figure 4.13 illustrates the contact regions 1 to 4 from left to right, respectively.

Physical connecting bodies do not interpenetrate, therefore ANSYS^{TM} offers several mathematical approaches to compute the contact pair to prevent them from passing through each other. These connection formulations are (ANSYS, 2010):

- Augmented Lagrange;

- Pure penalty;

- Multi-Point Constraint (MPC);

- Normal Lagrange;

- Program Controlled.

The augmented Lagrange and the pure penalty methods are suitable for solid body contact surfaces; however the augmented Lagrange method is less sensitive to the magnitude of the contact stiffness. The MPC formulation adds a constraint equation to the displacement of the connecting surface bodies and solving it by holding it together. The normal Lagrange method uses a Lagrange multiplier to add an extra degree of freedom to satisfy the contact compatibility. Finally, the last connection formulation, program controlled,
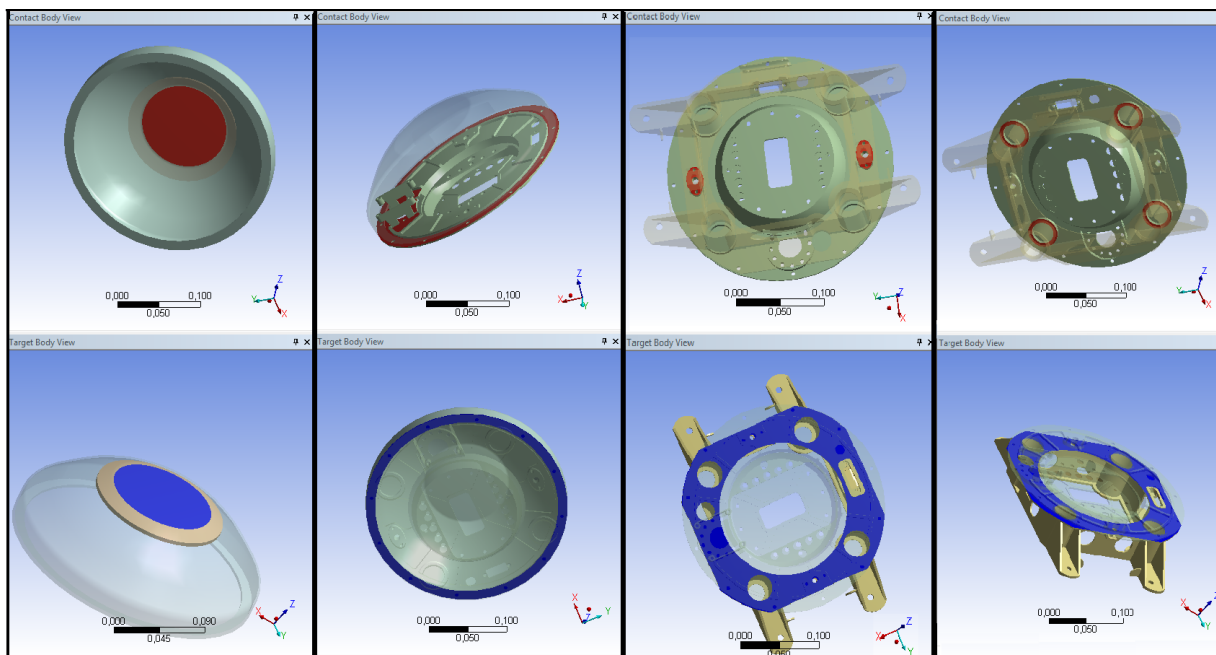
Figure 4.13: DOC's Connections Between Its Four Discretized Bodies

uses pure penalty and augmented Lagrange methods, depending on the contact situations.

Two contact regions, bounded and frictionless contacts are used to connect the bodies of the DOC together. ANSYS (2010) recommended to use pure penalty method for bonded contact regions since the contact stiffness is very high and the penetration is neglectable. For frictionless contact, augmented Lagrange is recommended because of its flexibility. Finally, program controlled is selected in ANSYS^{TM} since this approach automatically use the best method depending on the connection.

External
There are four types of connection which join the structure to its foundation; simple support, roller, pinned and fixed. As explained in Section 4.2, the host vehicle interface is bolted to the aluminium by means of four screws. The bolts resist against the vertical and horizontal forces as well as the moment. Therefore, the HVI is constrained only in the edges of the four holes of the screws that connect the HVI to the launch vehicle by selecting fixed support. Figure A.3 in Appendix A.3 illustrates the location of the four fix supports.

4.3.4. Material
Structural material used for the HVI and front and back shell are titanium alloy and tungsten used for the ballast. S[&]T reported in, *Aerothermodynamics, thermal and structural design, definition and justification file*, that the material used for the analyses is titanium alloy Ti6Al4V produced by of Electron Beam Manufacturing. The material characteristics including the manufacturing influences is tested by the subcontractor CIRA. The results of the investigation are shown in Table 4.2.

Depending to the ability of material, the material can be ductile of brittle. When the material undergoes plastic deformation before fracture, it is defined as ductile and when the material undergoes relatively little plastic deformation, it is characterized as brittle. Ductile materials absorb energy before failure while brittle materials are opposite to that. Based on different experimental tests and numerical simulations, Giglio et al. (2012) stated that the titanium alloy Ti6Al4V follows ductile failure criterion. This material property will be used in Section 5.4.

4.3.5. Mesh Convergence Analysis
The accuracy that can be obtained by the finite element method model depends strongly on the finite element mesh size. Smaller elements will compute a solution closer to the true solution but requires a larger

Table 4.2: Mechanical Properties of the Titanium Alloy and Tungsten

Properties	Titanium Alloy (Ti6Al4V)	Tungsten
Density [Kg/m^3]	4620	19300
Young Modulus [GPa]	96	400
Poisson Ratio [-]	0.36	0.28
Ultimate Strength [MPa]	764.21	980
Bulk Modulus [GPa]	117.861	303.03
Shear Modulus [GPa]	36.397	156.25
Tensile Yield Strength [MPa]	853	
Compressive Yield Strength [MPa]	930	
Tensile Ultimate Strength [MPa]	915	

Table 4.3: Results of Mesh Convergence Analysis of Natural Frequency

Mesh Size [mm]	Element Number	1st Mode [Hz]	2nd Mode [Hz]	3rd Mode[Hz]	4th Mode[Hz]
10	28164	202.10	280.42	292.59	316.81
5	82636	201.38	276.06	287.78	313.94
4	130692	199.34	271.59	283.44	306.5
3	235454	196.51	266.88	279.62	302.74
2	667882	194.13	263.33	276.25	299.67

computation time. A mesh size convergence analysis is performed to ensure that the influence of the size of the mesh in the FEM results is neglectable.

To perform a mesh convergence study:

- An element size of 10 mm is selected and the model is analysed;

- The model is re-meshed with a smaller element size, re-analysed and the new results are compared with the results from the previous step.

- The element size is decreased and the process continues until the results are within 4% of each other.

S[&]T stated in, *Aerothermodynamics, thermal and structural design, definition and justification file*, that if the results are within 4%, the mesh size is qualified for DOC.

In the first round, the mesh size was selected to be 10 mm. The analysis shows that this mesh size was too large and for some elements more solutions were available. Therefore, a mesh size of 5 mm is selected. From then, the mesh size is reduced in step sizes of 1 mm and the process continues.

Modal analysis has been conducted and the results of the first four modes of the natural frequency of DOC are shown in Table 4.3 and in Figure 4.14. Additionally, the accelerations will be defined in Section 5.3 are applied on the DOC in a static structural analysis. The maximum deformation of Ariane 5 is illustrated Figure 4.15. Table A.2 in Appendix A.4 shows the maximum deformation of Ariane 5. The rest of the locations/stages are also analysed and they are shown in Appendix A.4.

The aforementioned plots of the mesh convergence analysis of all locations show that a mesh size of 3 mm with 235454 elements gives results within 4% of the results obtained with more than twice the elements. Therefore, a 3 mm mesh size is a qualified mesh size for DOC model analysis.
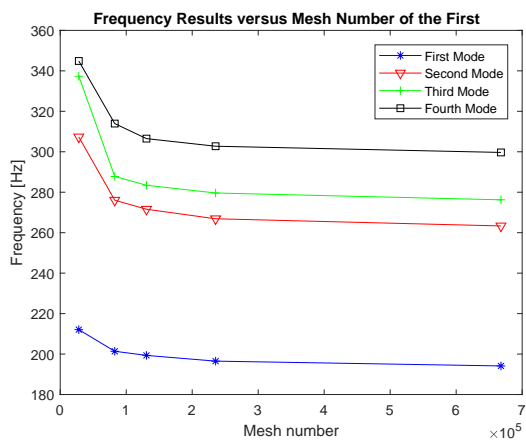
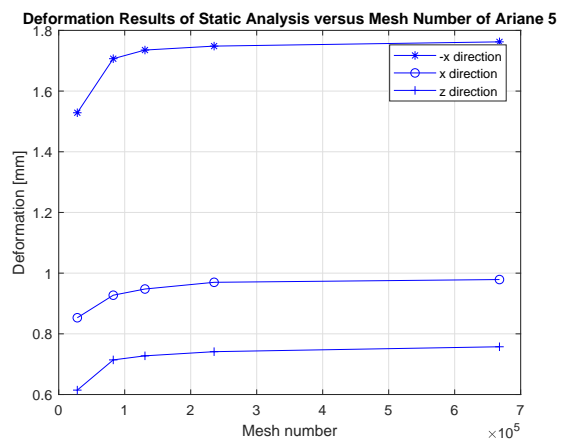Figure 4.14: Mesh Convergence Analysis of Natural Frequency Results

Figure 4.15: Mesh Convergence Analysis of Ariane 5 in Static Analysis

5

Results of Analysis

In this chapter, the results of the analyses will be presented. The model of Demise Observation Capsule (DOC) was already described in the previous chapter. Implementation of the model in the software is described in Section 5.1. Static, modal, and random vibration analyses have been conducted to obtain information about the model. Modal analysis is used to obtain information about the characteristics of the DOC's structure by determining the natural frequency and mode shape of the structure and its results are described in Section 5.2. To summarize the loads applied on the DOC, the natural frequency result was required. Therefore, Section 5.3 finalizes the loads explained in Section 3.4 per potential launcher location. These loads will be used in Section 5.4 to conduct static structural analysis. Static structural analysis is implemented at the sizing equivalent acceleration level, calculated with Miles' formulation, and the stresses and displacement under static loads can be determined. A more accurate structural investigation is performed by using the random vibration analysis and is described in 5.5. Finally, this chapter will be summarized in Section 5.6.

5.1. Numerical Set Up

ANSYS^{TM} version 18.1 is the software used for the simulations. ANSYS^{TM} is an user friendly finite element analysis tool that can open computer-aided design (CAD) systems. ANSYS^{TM} is a software environment for performing structural analysis. In the software, the geometries can be drawn, the existed geometries can be connected, the finite element model can be set up, the analysis can be solved, and the results can easily be reviewed. In other words, ANSYS^{TM} is able to execute preprocessing, processing, and post-processing (*ANSYS workbench user's guide*, 2009).

For this thesis, the Catia model was given by S[&]T in a (.CATPart) format. The model was imported in ANSYS^{TM} in the ANSYS DesignModeler (.agdb) format. Static, modal, and random vibration analyses have been conducted on the DOC. Each analysis is added to the project from the Toolbox as a system. Each system consists of seven individual cells. In Appendix A.5, the set up of Ariane 5 is shown. The other five locations have the same set up with different input loads. The first cell indicates the name of the analysis like Static Structural, Modal, or Random Vibration. In the second cell, Engineering Data, the material properties from Table 4.2 are filled in. The third cell, Geometry, is linked to the imported geometry model of the DOC. The link allows the geometry to be transferred from the Geometry system to other Geometry cell.

The Model cell has branches in the mechanical application and affects the geometry, coordinate systems, connections and mesh. In the branch Geometry, the bodies are linked to materials properties in the Engineering Data cell. Additionally, the lumped masses defined in Table 4.1 are added to the model in this branch. In the Coordinate System branch, the DOC and host vehicle interface (HVI) geometric reference frames are inserted, which were described in Section 4.1. The internal connections described in Section 4.3.3 and illustrated in Figure 4.13 are the input of the Connections branch. Finally, the Mesh branch consists of an element size of 3 mm , that comes from the result of the mesh convergence analysis in the Section 4.3.5.

The Setup cell is used to define the loads and the boundary conditions. The loads will differ per location and per analysis and will be defined in the following sections. The boundary conditions are the external con-

nections described in Section 4.3.3 and illustrated in Figure A.3.

From the Solution cell, the Solution branch can be accessed. For static analysis the equivalent stress, total deformation, and force reactions at the four boundary conditions and at the contact regions between the HVI and the back shell is selected. For modal analysis, total deformation at the first six modes, and for random vibration analysis, the equivalent stress is selected. Finally, the Result cell indicates the status of the analysis results.

In total, there are five systems for analysis and one system which include the imported geometry. The geometry of the first analysis system is linked to the geometry system. The Engineering Data, Geometry, and Model cells are linked to the their previous system, so the data does not need to be implemented every time. Finally, from the Solution cell of the modal analysis system a link is connected to the Set-up cell of the random vibration system, because to perform the random vibration the natural frequency of the DOC is required.

5.2. Modal Analysis

A modal analysis has been carried out to investigate the interaction between the launcher and the DOC, and to investigate the stiffness of the DOC. In this section, the modal analysis results are presented.

The launch vehicle has natural frequencies in all three directions. When the natural frequency of the DOC and the host launcher are close, DOC's natural frequency excited an additional load to the launcher. To uncouple the natural frequency of DOC from the host launcher, the DOC's first natural frequency mode should be larger than the launcher natural frequency in all directions. As a result of this difference in natural frequencies, DOC can be dynamically uncoupled from the launcher. DOC will behave as a rigid body at the natural frequencies of the host launcher. Table 5.1 presents the natural frequencies of the launchers on the lateral and longitudinal directions. Modal analysis shall comply with the requirements **Analysis-1-a** to **Analysis-1-c**.

Furthermore, the results of modal analysis can show a global mode or local mode. The mode can be identified as global if a substantial portion of the modal mass is involved in the vibration. and can be characterized as local if only a few percent of the modal mass participate in a vibration mode. Global mode indicates the global damage of the structure while the local mode expresses the local damage. Since, the finite element method can only predict the natural frequency mode and the actual value can be differ, requirement **Analysis-2** was considered to minimize this shift.

If the first global mode is lower than the local mode, the shift of the frequency is smaller due to the fact that the change is less relative to the whole DOC (Bolton, 2000). Additionally, according to Shenyan et al. (2018), the global natural frequencies are sensitive to the local natural frequencies. Therefore, if the local natural frequency occurs that a higher frequency than the global natural frequency, the local natural frequency is rigid when the global natural frequency occurs.

The requirements imposed from the above explanations are stated here.

- **Analysis-1** DOC shall have at least a minimum first mode above:

    - **Analysis-1-a** 31 Hz when it is placed on Ariane 5;
    - **Analysis-1-b** 60 Hz when it is placed on Vega;
    - **Analysis-1-c** 35 Hz when it is placed on Soyuz.

- **Analysis-2** First global mode of DOC shall be a lower than its first local mode.

Table 5.2 illustrates the frequencies of the first six natural modes. The first mode occurs at 196.49 Hz and therefore DOC meets requirements **Analysis-1-a** to **Analysis-1-c**.

Figure 5.1 illustrates the first mode, which occurs at 196.49 Hz and is a global mode. It is a result of quasi-rigid rotation of the capsule about the x-direction. The second, third, and fourth mode are local modes and occur at 231.84, 271.74, and 302.71 Hz at supporting plates of avionics, antenna, and camera, along the z-, z-, y-directions, respectively. The first global mode is lower than the first local mode and therefore requirement **Analysis-2** is met. The fifth mode is a global mode with a small translation of the capsule along the

Table 5.1: Natural Frequencies of Launchers (Lagier, 2016; Perez, 2014, 2012)

Launcher	Lateral Frequency [Hz]	Longitudinal Frequency [Hz]
Ariane 5	10	31
Vega	15	60
Soyuz	15	35

Table 5.2: Frequencies of the DOC at the First 6 Modes

Mode	1st	2nd	3rd	4th	5th	6th
Frequency [Hz]	196.49	231.84	271.74	302.71	344.6	404.05

y-direction with respect to the HVI that stays almost not deformed. The sixth mode is global mode with a large quasi-rigid translation of the capsule body along the z-direction.

The natural Frequency is described by Wijker (2009) as follows:

$$f_n = \frac{1}{2\pi}\sqrt{\frac{\mathbf{k}}{\mathbf{m}}} \tag{5.1}$$

where f_n is the natural frequency, $\mathbf{k}$ is the spring stiffness matrix, $\mathbf{m}$ is the mass matrix. Keeping the mass matrix constant, mode of the natural frequency is related to the stiffness of the model. A stiffer model has a higher frequency of the mode. As previously mentioned, the frequency mode appears in lowest frequency in the x-direction and then in frequency modes two and three in z-direction. In frequency mode five, deformation appears for first time in the structure of DOC in y-direction. It can be concluded that the DOC is much stiffer in the y-direction than in the other two directions.

5.3. Summarizing the Loads

As mentioned in Chapter 1, the first prototype of DOC was built for mounting the DOC on the Ariane 5, Vega, and Soyuz. In total four locations on these three launchers were identified and the DOC was designed for the worst case scenario. Furthermore, this research includes two additional locations on the Vega. This section will summarize the loads of both, thesis design loads, which refers to the six locations defined in this thesis and the current designed loads, which refers to the S[&]T defined four locations.

Research Design Loads

The loads were elaborated in Chapter 3. The imposed loads per launcher and per part summarized is shown in Table 5.3. The first modal frequency of DOC is at 196.5 Hz, as it was explained in previous section. The table illustrates the acceleration at a frequency of 196.5 Hz, acceleration peak after 196.5 Hz, and the frequency at which the peak occurs. These results are obtained from plots of Figures 3.6 to 3.12.

For Ariane 5, the acceleration at the frequency of 196.5 Hz is 800 m/s^2. S[&]T stated in, *Aerothermodynamics, thermal and structural design, definition and justification file*[1], that since the numerical models are never fully representative of the real DOC, designing DOC for an acceleration of 800 m/s^2 would for sure be unsafe. Additionally, in the same file, S[&]T noted that the results of the natural frequency of the numerical model expected to be lower than the actual model. Therefore, in consultation with S[&]T, it was decided to design for the acceleration peak, since the frequency of the acceleration at peak is relatively close to the first mode. Therefore, for Ariane 5, the sizing acceleration for the numerical simulation becomes 1008 m/s^2.

The same logic has been used to define the sizing load of the Attitude and Vernier Upper Module (AVUM), since the acceleration peak is relatively close to the first mode, S[&]T recommended to design for acceleration of 6226.9 m/s^2. For the other cases, the frequency at acceleration peak is much higher than the first mode and therefore, the acceleration at the 196.5 Hz is selected for design. Hence, 700, 3058.9, 3193.1, and 583 m/s^2 are sizing accelerations for Payload Adapter (PLA), Vega Secondary Payload Adapter (VESPA), Zefiro

---

[1]Aerothermodynamics, thermal and structural design, definition and justification file, Issue date: Augustus 8, 2017. This is a classified document and only available through S[&]T.
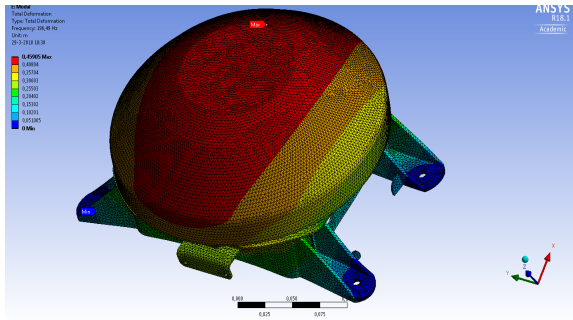
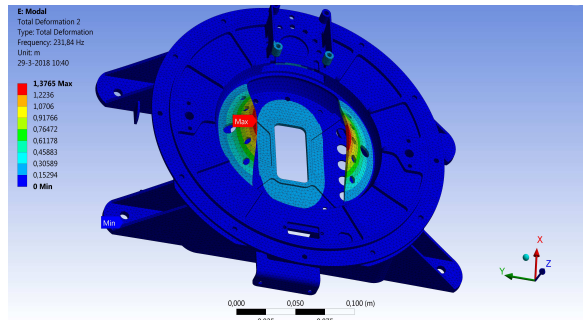Figure 5.1: Modal Analysis Results, First Mode of the DOC

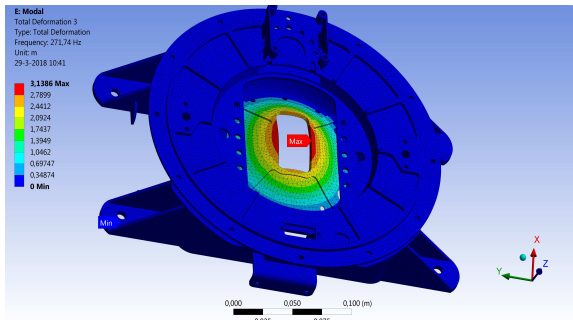Figure 5.2: Modal Analysis Results, Second Mode of the DOC

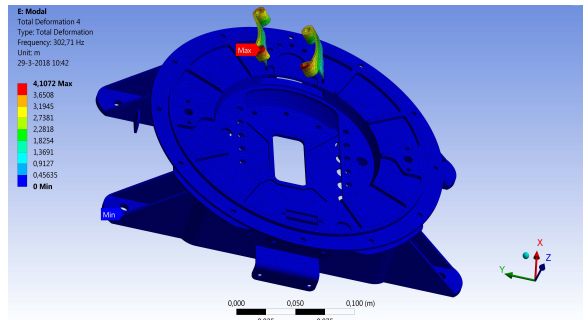Figure 5.3: Modal Analysis Results, Third Mode of the DOC

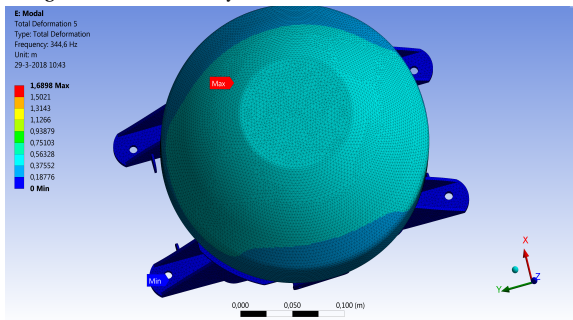Figure 5.4: Modal Analysis Results, Fourth Mode of the DOC

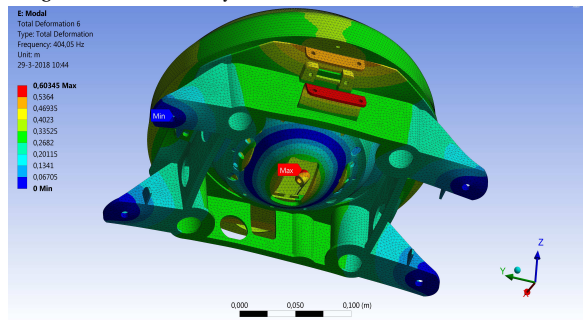Figure 5.5: Modal Analysis Results, Fifth Mode of the DOC

Figure 5.6: Modal Analysis Results, Sixth Mode of the DOC

Table 5.3: Computed Loads per Location

	Location	Acceleration at 196.5 [Hz]	Acceleration Peak [m/s^2]	Frequency at Acceleration Peak [Hz]
Ariane 5	UC	800	1008	315
	EPC	800	1008	315
Vega	AVUM	4477.8	6226.9	380
	PLA	700	1337	625
	VESPA	3058.9	5345.1	600
	Zefiro 9	3193.1	5345.1	600
Soyuz	3rd stage	583	922	500
	Fregat	583	922	500

Table 5.4: List of Current Load Design by S[&]T

	Acceleration at 196.5 [Hz]	Acceleration Peak [m/s^2]	Frequency at Acceleration Peak [Hz]
Ariane 5	800	1008	315
Vega	700	1337	625
Soyuz	583	922	500

9, and Soyuz, respectively.

Furthermore, all launcher manuals report that the acoustic and PSD loads should be applied in all 3 directions (Lagier, 2016; Perez, 2014, 2012). However, as it was explained in Section 5.2, during the modal analysis, DOC shows a much higher stiffness in the y-direction than in the x- and z-directions. The loads in the y-direction is neglected to simplify the analysis. Hence, the loads will be applied only on the x- and z-directions. Additionally, since the x-direction is the direction of the acceleration of the launchers, a severe load is expected in this direction. For safety reasons, the sizing load per location is also applied on the negative x-direction (-x-direction).

Current Design Loads

As mentioned in Chapter 1, the first prototype of DOC was built for the worst case scenario. Here, the approach for defining the sizing load is explained. Table 5.4 shows the three locations considered, followed by their acceleration at a frequency of 196.5 Hz, the acceleration peak after 196.5 Hz and the frequency at which the peak occurs. Comparing the three launchers, the Ariane 5 has the highest acceleration at 196.5 Hz and is therefore the sizing launcher. The acceleration peak of Ariane 5 occurs at 315 Hz, and since this is close to the first mode of the natural frequency, the 1008 m/s^2 value is used for the numerical simulations.

The Zefiro 9 random vibration has been considered without converting by Miles' equation into acceleration. Figure 5.13 shows the ASD input of Zefiro 9 for the random vibration analysis. To summarize, current design of the DOC is qualified for loads imposed by the Ariane 5, Vega, Zefiro 9, and Soyuz. The Ariane 5 and Zefiro 9 considered to impose the highest loads on the DOC. The Ariane 5 load is converted to acceleration, while the Zefiro 9 ASD was included in the analyses.

5.4. Static Analysis

This section describes the results of the static structural analyses of all six locations carried out at the sizing equivalent acceleration level, which was calculated by the Miles' equation. Section 5.3 summarized the loads, which will be applied in - x-, x-, and z-direction. Static analysis can determine the stresses and displacements under the static loading conditions. In this section, first the stress results will be covered followed by the results from the deformation.

To ensure that the stress results are within an acceptable range, a stress analysis is conducted. Von Mises stress is used for isotropic and ductile metal and shows whether the metal will yield when it is subjected to loads. Von Mises criterion defines a material yield when its critical distortial energy reaches a critical value. The Von Mises stress, in all six components, is expressed in Equation 5.2 and is compared to material's yield

stress, σ_Y (Varnes, 1962).

$$\sigma_Y = \sqrt{0.5[(\sigma_x - \sigma_y)^2 + (\sigma_y - \sigma_z)^2 + (\sigma_z - \sigma_x)^2] + 3(\tau_{xy}^2 + \tau_{yz}^2 + \tau_{zx}^2)} \qquad (5.2)$$

where σ_x, σ_y, and σ_z are the normal stresses and the subscript indicates the direction of stress; τ_{xy}, τ_{yz}, and τ_{zx} are the shear stresses. The first subscript indicates that the shear operates in a plane that is normal to that axis ; while the second subscript indicates that, within this plane, the line of action is parallel with that axis.

Table 5.5 shows the maximum equivalent stress and its location in the - x-, x-, and z-directions of all six potential DOC locations with respect to the DOC geometric reference frame. The plots of the stress results of the static structural analyses of all six locations are illustrated in Appendix A.6. Equivalent stress distribution maps show that the whole structure is well below the ultimate strength of the titanium alloy, which is 0.764 GPa. The allowable stress is exceeded only in correspondence of the four holes of the screws that connect the HVI to the launch vehicle. This overstress is due to numerical singularity. Considering the stress results of the static structural analyses, it is concluded that the DOC can be mounted on all six locations.

As explained in Section 4.3.3, the DOC is connected by four M5 steel screws via HVI to the launcher called external points and additionally back shell and HVI are connected by two M5 steel screws called internal points. Table 5.6 illustrates per location and per load direction (- x-, x-, and z-directions), the maximum deformation with respect to the DOC geometric reference frame. The highest maximum total reaction force (HMT RF) of the four fixation points is noted with its corresponding axial component with respect to the HVI geometric reference frame. Then, the HMT RF of the two internal points is stated with its corresponding axial component in the HVI geometric reference frame. The plots of the deformation results of the static structural analyses of all six locations are illustrated in Appendix A.6.

Screws used are made of steel and have a diameter of 5 mm. Steel has a tensile strength, σ_y, of 500 N/mm^2. Proper axial force, F$_a$, for a M5 steel screw is (Simon, 2010):

$$F_a = 0.7 \times \sigma_y \times A_s \qquad (5.3)$$

where, A$_s$ is the effective sectional area of the screw. For safety reasons, only 70% of the strength is included. Therefore, the axial loads are limited to 9817.5 N.

Table 5.6 indicates the axial reaction forces above the screws allowable axial force by red. When DOC is decided to be located on the AVUM, VESPA, and Zefiro 9, additional fixations points are required. This means that when the DOC is located on these three stages, the DOC will be detached from the host vehicle and is not able to perform its mission. Moreover, when the DOC is mounted on the AVUM, the contact area between the back shell and HVI will be detached since the screw tensile strength is lower than the applied axial load on the screw. As the thesis research is not about to improve the initial model, and S[&]T concluded that the current DOC can be mounted on the Ariane 5, Vega, and Soyuz, it was decided to only recommend to strengthen the model by adding additional fixations between the HVI and the host vehicle as well as between the HVI and the back shell.

Furthermore, an electrical connector is placed between the HVI and the back shell, called Harwin M90-6061645 connector. File, *Shape detailed design and detailed configuration*[2], shows the location where Harwin M90-6061645 connector is mounted on. It is placed next to the HVI camera as is illustrated in Figure 5.7. In the Harwin M90-6061645 connector technical report, the configuration of this connector is discussed (see Figure 5.8) (Miller, 2010*b*). If the vibration moves the two parts too far away, the connector could experience temporary disconnection. To avoid this, the maximum disconnection distance between the HVI and the back shell at the two closest frictionless contacts to the Harwin M90-6061645 connector should be less than its cable strip length of 8 mm.

Additional analyses have been conducted on the model to indicate the maximum deformation over time of the capsule with respect to the connector. When the DOC is located on the AVUM, it is imposed to the largest loads comparing with the other five locations, therefore, the DOC is only analysed when it is mounted on the

---

[2]Shape detailed design and detailed configuration, Issue date: Augustus 1, 2017. This is a classified document and only available through S[&]T
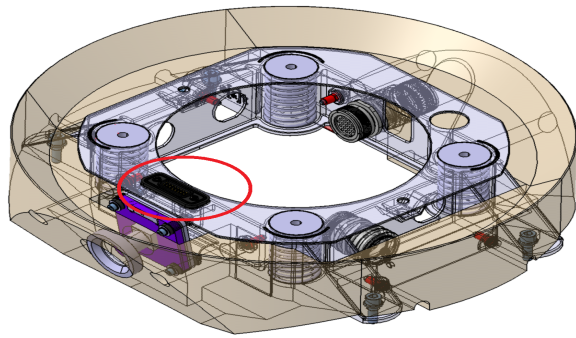
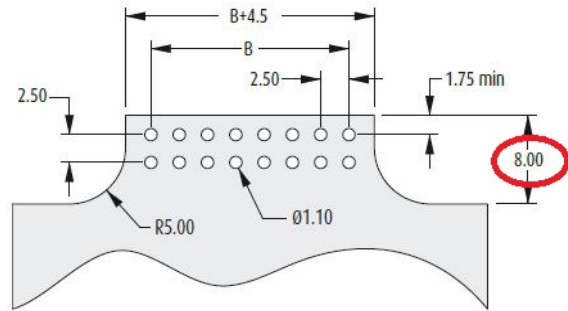Figure 5.7: Location of Harwin M90-6061645 Connector on the HVI

Figure 5.8: Harwin M90-6061645 Connector Configuration (Miller, 2010*b*)

Table 5.5: Equivalent Stress Results of Static Structural Analysis

Location	- x-direction		x-direction		z-direction	
	Max Stress [Gpa]	Location	Max Stress [Gpa]	Location	Max Stress [Gpa]	Location
Ariane 5	1.8712	HVI	1.746	HVI	0.71833	HVI
AVUM	10.0601	HVI	9.8963	HVI	4.3106	HVI
PLA	1.3008	HVI	1.2131	HVI	0.4989	HVI
VESPA	5.6517	HVI	5.2787	HVI	2.178	HVI
Zefiro 9	5.45	HVI	5.0913	HVI	2.2148	HVI
Soyuz	1.0014	HVI	0.9337	HVI	0.4048	HVI

AVUM. The deformations are with respect to the HVI reference frame and showed that in the - x-direction the maximum deformation over time is 7.57 mm, while in the x-direction is 3.85 mm. In the z-direction, this deformation was 1.85 mm. Since, the maximum deformation over time is lower than the strip length, it means that the Harwin M90-6061645 connector will be connected all the time.

5.5. Random Vibration Analysis

This section presents the results of the random vibration analyses, thus when Miles' equation is not in use. The power spectrum density (PSD) of Figures 3.6 and 3.8 to 3.12 is converted into acceleration spectrum density (ASD) by using Equation 3.12. The ASD input data are illustrated in the graphs 5.9 to 5.14 for Ariane 5, AVUM, PLA, VESPA, Zefiro 9, and Soyuz, respectively. The ASD data are obtained from the qualification data of the loads, which means that the safety factors from Table 3.5 are included.

The finite element solver uses ASD directly and produces a stress distribution. The results from the solver show a 1-σ stress distribution, following a Gaussian distribution. This means 68.3% of the time the response will be less than the standard deviation value. Usually, a 3-σ stress distribution is required, which means 99.73% of the time. However, the input data includes the safety factor, which counts for a 2-σ. Therefore, a 1-σ stress distribution is considered sufficient according to S[&]T's report, *Aerothermodynamics, thermal and structural design, definition and justification file.*[3]

Finally, it was decided to analyse both the 1-σ and 3-σ stress distribution to compare the results and define the sensitivity of this decision. Note that, the 1-σ stress distribution is still the sizing stress distribution.

Equivalent stress distribution maps show that the whole structure is well below the ultimate strength of titanium alloy, 0.764 GPa. The allowable stress is exceeded only in correspondence of the four holes of the screws that connect the HVI to the launch vehicle. The stress distribution of the random vibration results on all six locations are illustrated in Appendix A.7.

---

[3]Aerothermodynamics, thermal and structural design, definition and justification file, Issue date: Augustus 8, 2017. This is a classified document and only available through S[&]T

Table 5.6: Total Deformation and Force Reactions Results of Static Structural Analysis

Location	Direction	Deformation [mm]	External Points		Internal Points	
			HMT RF [N]	Axial RF [N]	HMT RF [N]	Axial RF [N]
Ariane 5	- x-	1.749	4079.7	3304.3	3924.8	2243.4
	x-	0.9657	4279.7	3309.2	3241	320.1
	z-	0.8863	4067.4	3171.5	1693.3	145.7
AVUM	- x-	10.67	25239	20419	34340	20419
	x-	5.9011	26487	20451	20046	2022.7
	z-	5.4678	25110	19590	10492	847.85
PLA	- x-	1.2158	2832.3	2294.5	2726.0	1558.0
	x-	0.67048	2971.8	2298.0	2250.5	220.78
	z-	0.61552	2824.9	2202.4	1175.9	101.37
VESPA	- x-	5.272	12393	10030	11904	6799
	x-	2.9155	13000	10045	9839.1	977.2
	z-	2.6882	12338	9623.8	5142.9	433.49
Zefiro 9	- x-	5.4947	12930	10466	12426	7048
	x-	3.0466	13565	10483	10276	1015
	z-	2.3495	12883	10044	5392.6	484.55
Soyuz	- x-	1.013	2358.6	1911	2270.6	1297.5
	x-	5.585	2475.1	1913.9	1874.4	183.86
	z-	0.5127	2352.8	1834.3	979.41	84.48

Table 5.7: Equivalent Stress Distribution Using Random Vibration Analysis

Location	1-σ		3-σ	
	Max Stress [Gpa]	Occurs on	Max Stress [Gpa]	Occurs on
Ariane 5	0.43344	HVI	1.3003	HVI
AVUM	2.2173	HVI	6.6518	HVI
PLA	0.33962	HVI	1.0189	HVI
VESPA	1.5212	HVI	4.5636	HVI
Zefiro 9	1.4124	HVI	4.5601	HVI
Soyuz	0.28185	HVI	0.84555	HVI

The maximum stresses of all potential stages are illustrated in Table 5.7 for both the 1-σ and 3-σ stress distribution curves. When the ultimate strength of titanium alloy, is exceeded, the value is indicated by the red color. Only in AVUM, VESPA, and Zefiro 9 locations the allowable stress in exceeded in the 1-σ stress distribution. While, in the 3-σ all locations exceed the allowable stress.

The result of static structural analysis in the - x-, x-, and z-directions and the 1-σ stress distribution of random vibration analysis of the Ariane 5 are illustrated in Figures 5.15 to 5.18, respectively. According to Bolognese and Simmons (2009), the Miles' equation can be conservative, however the software is unable to perform optimization on random vibration (this will be explained in more details in Section 6.3.2). Hence, the results of this two methods should be compared to find out whether the results of static analysis is a suitable representative of the random vibration results. Comparing the equivalent stress distribution from Miles' equation with random vibration using ASD, it was concluded that the results of the whole structure are similar to each other. However, when the fixation holes of HVI are analysed, Miles' equation results from Table 5.5 are higher than even the 3-σ stress distribution. Therefore, the results from Miles' equation can be representative in optimization process since they are higher.
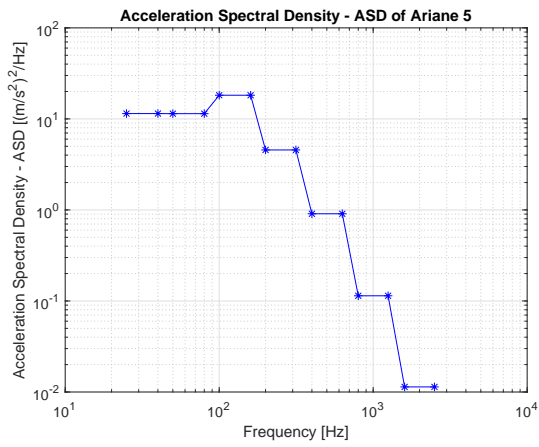
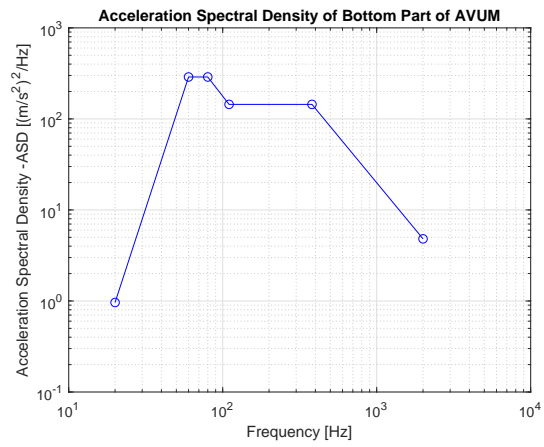Figure 5.9: Acceleration Spectral Density of Ariane 5
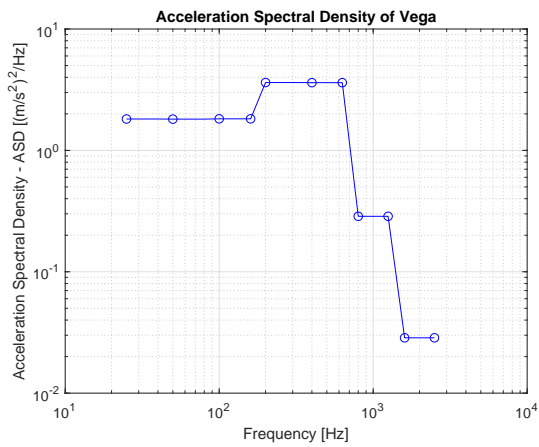

Figure 5.10: Acceleration Spectral Density of AVUM

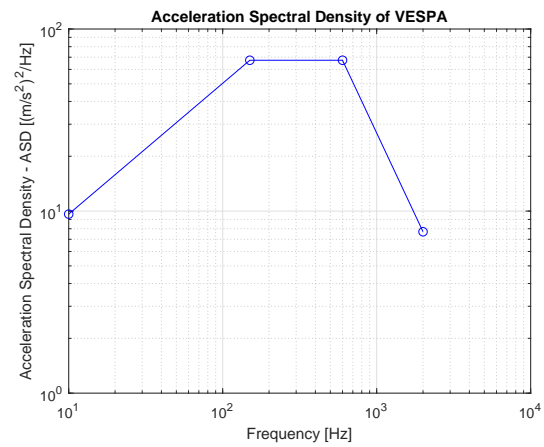Figure 5.11: Acceleration Spectral Density of PLA

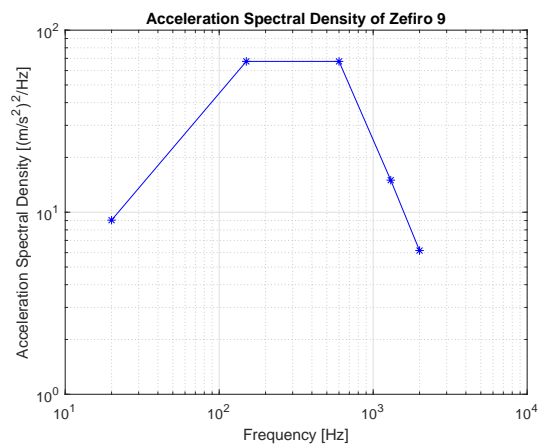Figure 5.12: Acceleration Spectral Density of VESPA
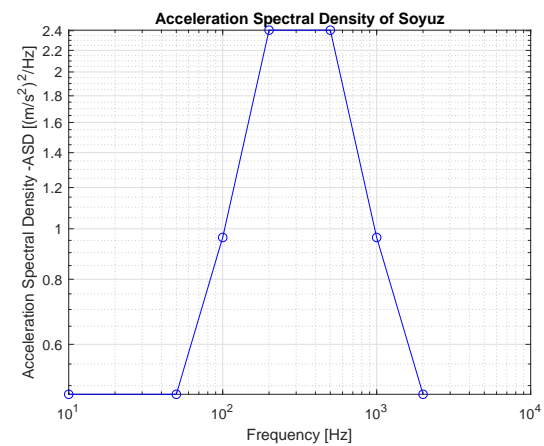

Figure 5.13: Acceleration Spectral Density of Zefiro 9

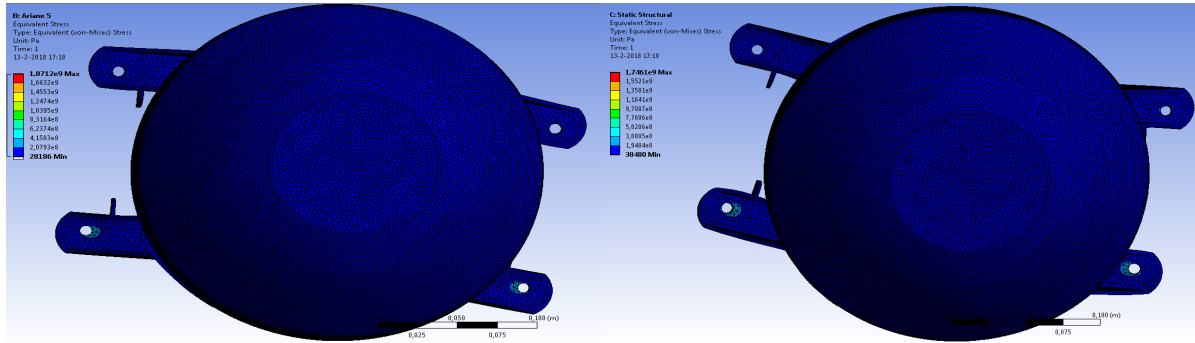Figure 5.14: Acceleration Spectral Density of Soyuz

Figure 5.15: DOC Stress Results of the Static Analysis on Ariane 5, Acceleration -x = 1008 m/s^2

Figure 5.16: DOC Stress Results of the Static Analysis on Ariane 5, Acceleration x = 1008 m/s^2
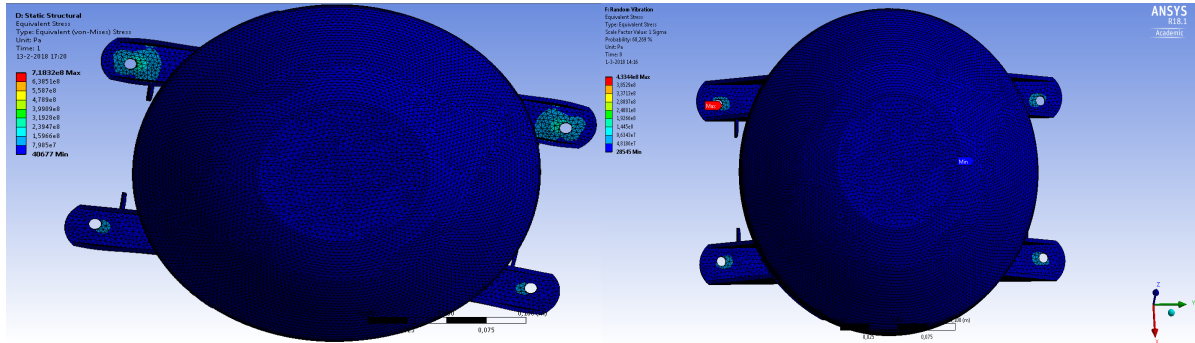
Figure 5.17: DOC Stress Results of the Static Analysis on Ariane 5, Acceleration z = 1008 m/s^2

Figure 5.18: The 1-σ Stress Distribution Results of Random Vibration Analysis on Ariane 5

5.6. Conclusion

In this section, the results of the analyses are concluded briefly. The configuration was imported in ANSYS^{TM} and modal, static structural, and random vibration analyses were conducted on the model. The results of these analyses will indicate whether or not the DOC can be locate on the six predefined locations.

Modal analysis shows that the DOC meets the requirements **Analysis-1-a** to **Analysis-2** and that the DOC is much stiffer in the y-direction than in the other two directions. Therefore, the loads will be applied only in x- and z-direction. Additionally, for the safety reasons, the sizing load per location is also applied on the - x-direction.

Static structural analyses conclude that the DOC needs additional fixations between the HVI and the host vehicle when it is mounted on the AVUM, VESPA, and Zefiro 9. Furthermore, the HVI and the back shell should be connected by an additional fixation when DOC is located on the AVUM. The plots of the deformation results of the static structural analyses shows that in all six cases, the frictionless connection is disconnected in the - x-, and x-directions. Figure 5.19 shows the disconnection of the frictionless contacts when the DOC is mounted on the AVUM. This problem was already recognized by S[&]T. As the thesis research is not about to improve the initial model, it is only recommended to strengthen the model by adding additional fixations between the HVI and the host vehicle as well as between the HVI and the back shell. After adding this fixations, the initial DOC model can be mounted on these six locations.
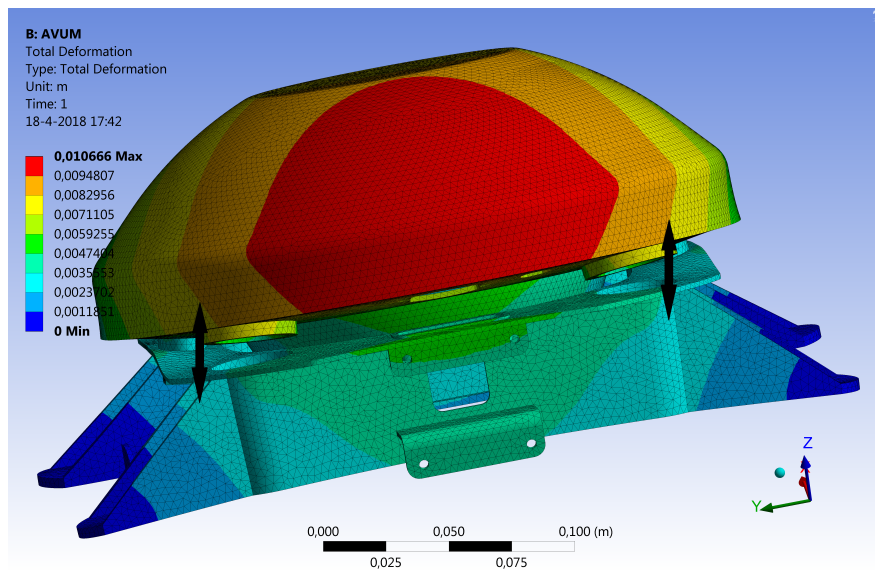
Figure 5.19: The DOC Deformation Results of the Static Structural Analysis on the AVUM

<div align="right">

6

</div>

<div align="right">

Optimization

</div>

This chapter introduces the optimization methods, selects, and underlines the topology optimization and the most common methods applied in structural topology optimization. The purpose of this chapter is to present the topology mass minimization of the Demise Observation Capsule (DOC) subject to material failure constraints and volume constraint in multiple load cases. Section 6.1 presents the optimization methods. Section 6.2 explains the topology optimization approaches and selects the most suitable method after a trade-off. Section 6.3 applies the topology optimization method on the DOC to minimize its mass.

6.1. Optimization Methods

Optimization is a process where structural and design parameters are modified until a certain objective is met. A wide variety of optimization methods is available. In structural applications three types of optimization are frequently used, i.e. size, shape, and topology optimization (Bendsøe and Sigmund, 2003). These methods are distinguished based on the design variables used during the optimization and their optimizer freedom. This section provides a brief description of these methods. Figure 6.1 illustrates these three methods. The initial structure is given on the left with the optimized result on the right.

In size optimization, the design variables are the variables relating to the thickness of the plates or the cross-section of trusses. Only these parameters are allowed to be modified during the optimization routine. This approach is the easiest and earliest approach to optimizing the structural performance.

In a typical shape optimization, the objective is to determine the optimum shape. It is mainly performed on continuum structures by modifying the predetermined boundaries such as hole size and the cross-sectional areas as design variables to obtain the optimal structure. The shape optimization compared to the size optimization has a larger design freedom.

Topology optimization gives a much larger freedom to its optimizer. In this method, the optimal layout of the structure within a specified region is defined. The density of each element in the finite element discretization is defined as a design variable. During the optimization, the element densities are scaled to represent either solid or void material and thereby generates a new topology to optimizing the structural performance for the objective of interest.

Topology optimization is a powerful method and by far the most challenging and most rewarding method of all. This approach can generate complicated and free-form designs with optimized performance for a certain objective. The current model of the DOC is already optimized by using the size optimization method. This thesis is conducted during the detail design phase of the DOC and the DOC can have a complicated and free-form configuration due to it being manufactured using a 3-D printer. Furthermore, using the topology approach reduces optimization time while its design performance is improved. Hence, the topology optimization approach will be applied for the optimization of the DOC. Topology optimization has been studied for several years by researchers, and different formulations and implementations of topology optimization routines have been established. Providing a complete literature overview on the available approaches is be-
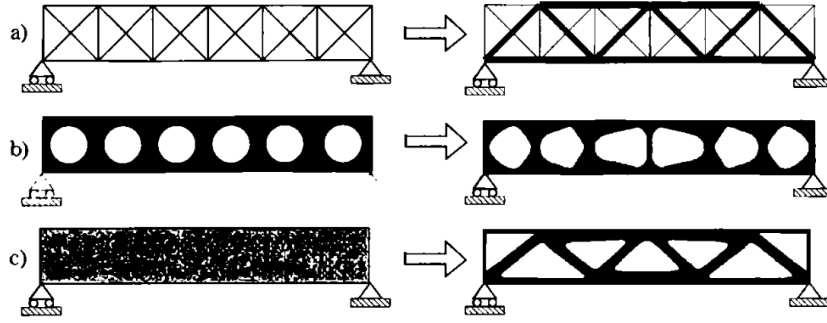
Figure 6.1: From Top to Bottom, a) Size, b) Shape, and c) Topology Optimization (Bendsøe and Sigmund, 2003)

yond the scope of this thesis. However, the following section summarized a few of the most popular methods suitable for structural optimization.

6.2. Topology Optimization

Topology optimization aims to acquire an optimal structural configuration within a given design domain for predefined objective while it is subjected to constraints, loads and boundary conditions. Topology allows the optimizer to determine the shape and the size of each design feature, in other words this method finds the best distribution of material given an optimization goal and a set of constraints (Bendsøe and Kikuchi, 1988).

Consider a general topology optimization problem where the material distribution that minimizes an objective function F subject to a volume constraint $G_0 \leq 0$ and possibly M other constraints $G_i \leq 0$, $i = 1, 2, ..., M$. The material distribution is defined by the density variable $\boldsymbol{\rho}(\mathbf{x})$ that can take either the value 0 (void) or 1 (solid material) at any point in the design domain Ω. The mathematical description of this optimization problem can be formulated as follows (Sigmund and Maute, 2013):

$$\text{min} : \qquad F = F(\mathbf{u}(\boldsymbol{\rho}), \boldsymbol{\rho}) = \int_{\Omega} f(\mathbf{u}(\boldsymbol{\rho}), \boldsymbol{\rho}) dV \tag{6.1a}$$

$$\text{subjected} \quad \text{to} : \qquad G_0(\boldsymbol{\rho}) = \int_{\Omega} \boldsymbol{\rho}(\mathbf{x}) dV - V_0 \leq 0 \tag{6.1b}$$

$$G_i(\mathbf{u}(\boldsymbol{\rho}), \boldsymbol{\rho}) \leq 0, \quad j = 1, \cdots, M \tag{6.1c}$$

$$\boldsymbol{\rho}(\mathbf{x}) = 0 \quad or \quad 1, \quad \forall \quad \mathbf{x} \in \Omega \tag{6.1d}$$

note that $\mathbf{u}$ is a state field that satisfies a linear or non-linear state equation and for simplicity reasons, it is assumed that the objective function can be computed as the integral over a local function $f(\mathbf{u}(\boldsymbol{\rho}), \boldsymbol{\rho})$.

This section introduces three topology optimization approaches. First, a density base method is explained in Section 6.2.1. Second, the Evolutionary Structural Optimization method (a branch of the discrete approach) is discussed in Section 6.2.2. Third, the level set topology optimization method is defined in Section 6.2.3. Finally, all three methods are briefly compared and one approach is selected in Section 6.2.4.

6.2.1. Density Based

The most widely used methodology in structural topology optimization is the density based method, which includes the Solid Isotropic Material with Penalization (SIMP) method. This method was introduced by Bendsøe (1989) and later by Zhou and Rozvany (1991); Mlejnek (1992). In this approach, each element within the finite element discretized is considered homogeneous and isotropic. A density value is assigned to each element. These density values are the design variables to the optimizer. The density of each element is scaled between a solid and void material ([0 1] solution space). From a manufacturing aspect, an intermediate material in final designs is undesirable. A penalization is applied to force the design towards solid and void elements. This is realized by defining how the relation between the density design variable and the material property of each element are related. They are related as follows.

$$E(\rho_i) = \rho_i^p E_0, \qquad 0 \leq \rho_i \leq 1, \qquad p > 1 \tag{6.2}$$

where E_0 defines the Young's modulus of solid material corresponding to point **x** in the design domain Ω, ρ_i is the local density of the material for the element located at **x**. A penalization parameter of p = 3 is applied to obtain designs with minimal intermediate materials. This value assures an acceptable convergence to almost 0-1 solutions (Sigmund and Maute, 2013).

The SIMP method is combined with gradient-based algorithm optimization to find the optimal topology for the specified objective within a reasonable number of iterations from 10 to 1000 (Sigmund and Maute, 2013). The topology optimization problem from Equation 6.1 can be rewritten as:

$$\min: \qquad F = F(\mathbf{u}(\boldsymbol{\rho}), \boldsymbol{\rho}) = \sum_i \int_{\Omega_i} f(\mathbf{u}(\rho_i), \rho_i) dV \tag{6.3a}$$

$$\text{subjected to:} \qquad G_0(\boldsymbol{\rho}) = \sum_i v_i \rho_i - V_0 \leq 0 \tag{6.3b}$$

$$G_j(\mathbf{u}(\boldsymbol{\rho}), \boldsymbol{\rho}) \leq 0, \quad j = 1, \cdots, M \tag{6.3c}$$

$$0 \leq \rho_i \leq 1, \quad i = 1, \cdots, N \tag{6.3d}$$

where $\boldsymbol{\rho}$ indicates the design variable vector of the length N. The sensitivities with respect to the objective function are determined on an element level. During each iteration the element densities are modified using the sensitivity information to achieve an updated topology with improved performance.

6.2.2. Evolutionary Structural Optimization
The Evolutionary Structural Optimization (ESO) approach is very similar to the SIMP method. The ESO is a discrete version of SIMP (Sigmund and Maute, 2013). This method was published by Xie and Steven (1993) and each element is either a solid or a void. To overcome difficulties regarding discrete optimization, a heuristic updating step is used to update the topology in each step. The topology optimization problem from Equation 6.1 can be rewritten as:

$$\min: \qquad F = F(\mathbf{u}(\boldsymbol{\rho}), \boldsymbol{\rho}) = \sum_i \int_{\Omega_i} f(\mathbf{u}(\rho_i), \rho_i) dV \tag{6.4a}$$

$$\text{subjected to:} \qquad G_0(\boldsymbol{\rho}) = \sum_i v_i \rho_i - V_0 \leq 0 \tag{6.4b}$$

$$G_j(\mathbf{u}(\boldsymbol{\rho}), \boldsymbol{\rho}) \leq 0, \quad j = 1, \cdots, M \tag{6.4c}$$

$$\rho_i = 0 \quad or \quad 1, \quad i = 1, \cdots, N \tag{6.4d}$$

A downside of the ESO method is the ability to only remove elements from the structure, regardless if the sensitivities would indicate otherwise.

6.2.3. Level Set Topology Optimization
The level set method goes about a different approach to describe and modify the topology than the aforementioned topology optimization methods. The level set method's root lies in shape optimization. This method was developed by Osher and Sethian (1988) for other applications and recently was used by Allaire et al. (2002); Wang et al. (2003) in structural and topology optimization. This method is based on implicit functions that define the structural boundaries rather than scaling element densities. Figure 6.2a displays when the domain, Ω, explicit parameterization of variables x, is between 0 and 1. The structural boundary, $d\Omega$, can vary at the interface of region 0 and 1. Figure 6.2b shows when the structural boundary is implicitly defined as a contour line of the field ϕ.

In the level set approach, the boundaries of the design are characterized by the zero level contour of the field, $\phi(x)$. The structure is presented by the domain where the level set function becomes positive.

$$\rho = \begin{cases} 0 & : \quad \forall \quad \mathbf{x} \in \Omega \quad : \quad \phi < 0 \\ 1 & : \quad \forall \quad \mathbf{x} \in \Omega \quad : \quad \phi \geq 0 \end{cases} \tag{6.5}$$

The level set function is updated by using Hamilton-Jacobi equation (Sigmund and Maute, 2013):

$$\frac{\delta \phi}{\delta t} = -V \mathbf{n}.\nabla \phi \tag{6.6}$$

where t is a pseudo-time and shows the progress of the model in the optimization technique, and V indicates the speed function in the normal direction **n** (**n**= $\nabla \phi$/ $|\nabla \phi|$).
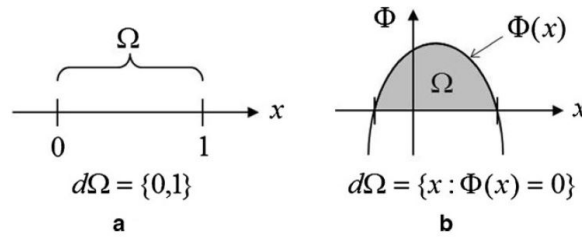
Figure 6.2: a) Explicit vs b) Implicit visualization of the Design Domain and Boundaries in the Level Set Topology Optimization
(Bendsøe and Sigmund, 2003)

6.2.4. Comparison of Topology Optimization Methods

In previous sections, the three most common approaches in the implementation of topology optimization were discussed. These presented methods are all applicable to a structural topology optimization problem. As the thesis research is not about studying different topology optimization methods, the one that performances sufficiently, as well as can easily be implemented numerically, is selected.

During the study of the three aforementioned approaches, it became clear that these methods are not so different from each other. They use the same sensitivity information and a filtering approach to obtain a smooth convergence. The only differences noticed are their type of update scheme, the gradient-based, heuristic, and Hamilton-Jacobi is used for the SIMP, ESO, and level set approaches, respectively. Deaton and Grandhi (2014) compared the three methods and stated that the results of the three approaches are very close. Therefore, their performance is close to each other and will be not considered during the trade-off. Furthermore, several commercial software packages such as ANSYS^{TM} can perform topology optimization. Bankoti et al. (2015) stated that the SIMP method is implemented in ANSYS^{TM} and therefore selecting the SIMP method will ease the numerical implementation. Additionally, several sources, such as Atani et al. (2016), compared the results achieved by ANSYS^{TM} and MATLAB. The SIMP approach was applied to simple academic structures, such as a Messerschmitt Bolkow Bolhm beam and a Cantilever beam using ANSYS^{TM} and MATLAB. The results were almost the same, especially in the last iterations. Atani et al. (2016) concluded that the topology optimization in ANSYS^{TM} is suitable to apply on the industrial and real world structures. Hence, the SIMP approach was selected to perform topology optimization process.

6.3. Optimization Description

Topology optimization option is a built-in feature within ANSYS^{TM}. The formulation and the numerical set up of the DOC topology optimization in ANSYS^{TM} is explained in this section. To formulate the structural optimization problem, the objective function, design variables, and constraints need to be introduced as described by Christensen and Klarbring (2009b). Section 6.3.1 explains the limitations of this research subject. Section 6.3.2 describes some simplifications required to implements the model into the software. Section 6.3.3 defines briefly the objective. Section 6.3.4 specifies the design and non-design regions and the constraints. Finally, Section 6.3.5 defines the load case and implements the model into the software.

6.3.1. Limitations

Optimizing is a time consuming process and to stay within the time limitation, it was decided that some aspects are beyond the scope of this thesis. These limitations reduce the number of design variables and they are explained in this section.

The design and analysis of a spacecraft comprises of multiple discipline areas. The first model of the DOC is designed for structural, aerodynamic and thermal protection. For this research, it was decided that thermal control design is not part of it. Whether the front or back thermal protection shields are optimized for different ascent and re-entry trajectories, depending on the new locations, are not considered in this thesis. Despite the exclusion, the first DOC is qualified for the worst case scenario and it is an applicable assumption that the heat protection shield is still valid for other locations on the launcher stage. In other words, the DOC thermal protecting can be over-designed for new locations and hence, the mass of the thermal shield can only be reduced in weight for not as extreme cases. Additionally, the aerodynamic discipline is also beyond the scope of this thesis.

6.3.2. Simplification

ANSYS^{TM} offers a built-in topology optimization feature. During a brief study of the software, it was found that the topology optimization feature is able to take multiple static structural and modal analyses into account. Therefore, the load cases were simplified by converting the random vibrations into the static structural loads using Miles' equation from Section 3.3.2.

Furthermore, the built-in topology optimization feature has some limitations, it cannot handle non-linearity. For example it could only support contact type bonded and not a frictionless contact and it does not support a static structural analysis with inertial loads. Therefore, to be able to use topology optimization feature in ANSYS^{TM}, the model is simplified and these two simplifications are:

1. The frictionless connection between the back shell and the host vehicle interface (HVI) is simplified by either removing this connection or by replacing it by a bonded connection;

2. The acceleration load in static structural analysis is converted to the force applied on the center of gravity of the DOC.

The HVI and the back shell are connected by two bonded contacts and four frictionless contact areas. Since the topology optimization feature cannot support the frictionless contacts, the four contacts are simplified. There are two options: either remove the frictionless contacts or replace it by a bonded contact. The initial DOC model was remodelled by either of the two options and deformation results in static structural analysis and the natural frequency in the modal analysis were computed. The results of static structural analysis and the modal analysis of both simplification options and the results of the initial model under the Ariane 5 loads are shown in Figures 6.3 and 6.4, respectively. Only one load case, Ariane 5 load, is applied for the simplification analysis, since it is expected that the results are independent of the load case.

Figure 6.3 shows the maximum deflection in the static structural analysis in the - x-, x-, and z-direction for the three models, the initial model, the model in which the frictionless contacts are removed, and the model in which the frictionless contacts are replaced by the bonded contacts. This plot shows that the maximum deformation of removing the frictionless contact is much higher than the maximum deformation of the initial model. The maximum deformation of replacing frictionless by a bonded contact is very close when the acceleration is applied in x- and z-direction. Figure 6.4 plots the natural frequency versus the mode number for all three aforementioned models. This plot shows that the natural frequency of the model that its frictionless contacts are replaced by bonded contacts is closer to the initial model than the model which its frictionless contacts are removed. Therefore, in discussion with S[&]T experts, it was decided to replace the frictionless contacts with bonded contacts, since the results of the static structural and modal analysis are closer to the results of initial model.

The second simplification requires converting the acceleration to force by the second law of Newton, $F = m \times a$, where F is the force in N, m is the total mass of the DOC and approximately equal to 10 kg, and a stands for the acceleration. The force should be applied on the center of mass of the DOC, however selecting a remote point is not possible and a discretized body needs to be selected. Therefore, the closest point to the center of mass was selected to apply the force. The bottom face of the ballast was the closest to the DOC's center of mass (see Section 7.2.2) and therefore that surface is selected to apply the force. The results are illustrated in Figure 6.5. Four different cases illustrated are as follow.

- Initial model: The HVI and the back shell have two frictionless connections, and acceleration is applied during the static analysis;

- Case 1: The two frictionless contacts are replaced by bonded contacts, and the acceleration is applied during the static analysis;

- Case 2: The HVI and the back shell have two frictionless connections, and force is applied on the ballast in the static analysis;

- Case 3: The two frictionless contacts are replaced by bonded contacts, and the force is applied on the ballast in the static analysis.
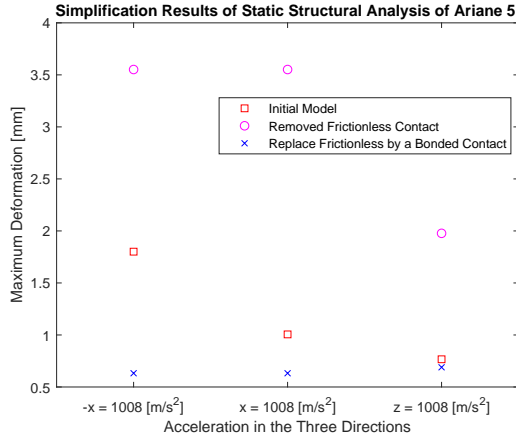
Figure 6.3: Static Structural Analyses Results of the First Simplification of Ariane 5
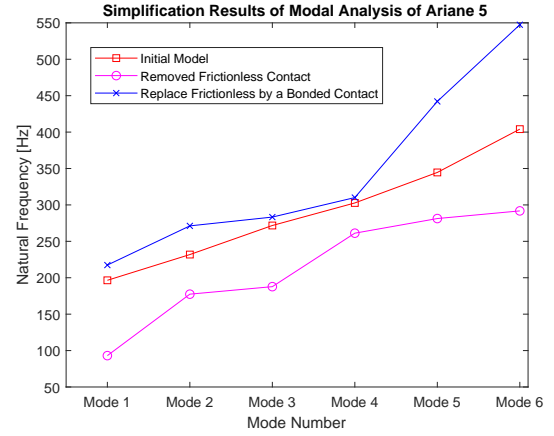
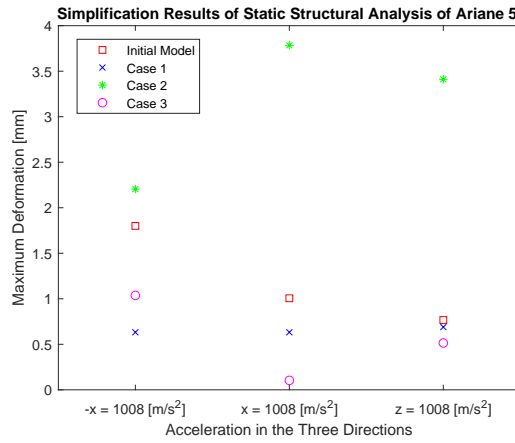Figure 6.4: Modal Analyses Results of the First Simplification of Ariane 5

Figure 6.5: Static Structural Analyses Results of Simplification of Ariane 5

Case 1 and 2 are the separate simplifications, while case 3 is the final model and an combination of both. While the second simplification causes a larger deformation than the initial model, the first simplification causes a smaller deformation than the initial model. Therefore, the adjoint simplification will be closer to the initial deformation results. However, the deformation of the initial model is higher than the deformation in case 3 and therefore the mass reduction is expected to be lower in the software topology optimization result. This will be taken into account during the redesigning of the DOC model.

6.3.3. Objective

The optimization targets the minimization of the objective function, limited by a set of constraints. The optimization can target different aspects. In this section this objective will be explained.

The objective of the DOC optimization is to minimize the mass:

$$\min \quad M(\mathbf{x}) = \sum_{e=1}^{235454} \rho_e \times V_e \qquad 1 \le e \le 235454 \tag{6.7}$$

where $\mathbf{x}$ are the design variables, M is the mass and a function of the design variables, ρ_e stands for density of the element, e stands for number of elements and in mesh convergence analysis in Section 4.3.5 an amount of 235454 elements was qualified, and V_e for volume of the element.
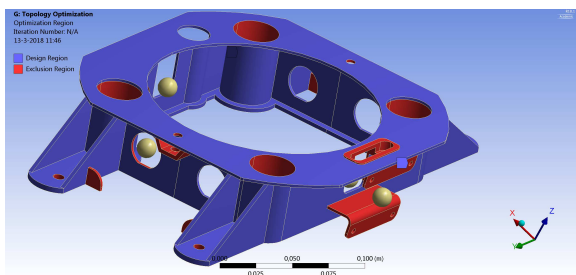
Figure 6.6: *Design* and *Non-Design* Regions of the HVI
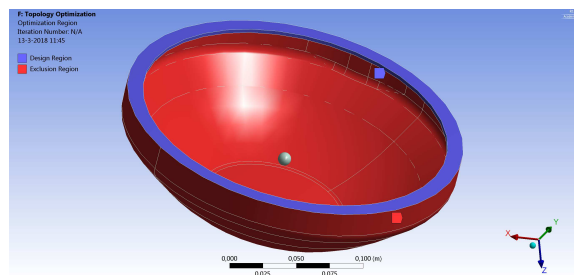
Figure 6.7: *Design* and *Non-Design* Regions of the Front Shell

6.3.4. Design Variables and Constraints

The design variables describe the DOC's shape, define what is allowed to vary in the topology optimization, and the constraints are responsible for keeping the optimized model under feasible limits. In the present study, the design variables are divided into *design* and *non-design* regions. The *design* region property was selected to vary.

The DOC model consists of four bodies, the front shell, the back shell, the ballast, and the HVI. The back shell is considered as a *non-design* region since this part also functions as thermal protection. The ballast is also considered as a *non-design* region, since its function is only to shift the center of gravity towards the nose of the DOC. The two bodies that are left, the HVI and the front shell, are considered as a *design* regions.

The HVI *design* region is constrained by some *non-design* areas. The red areas in Figure 6.6 are the excluded surfaces and the blue color indicates the *design* areas. In total, 122 surfaces are excluded. The HVI has four springs, each mounted in a cylindrical leg of the interface. The length and the diameter of the springs are fixed, which makes the diameter of the holes in the HVI constant. Furthermore, the HVI camera and the electrical connectors opening circles are fixed for the fitting reasons to allow those systems to do their task. Additionally, holes to fix the thermal protection system to the HVI and holes to fix the HVI to the host vehicle are designed as *non-design* areas.

The front shell body was considered as a *design* region. However, as in the case of the back shell, the front part of the front shell also functions as a thermal protection and therefore, the front part is considered as a *non-design* area. In total, 41 surface are excluded from the optimization process. The front shell edge, where the front shell was fixed to the back shell, was designed as a *design* region and is illustrated in Figure 6.7 by the blue trim.

The *non-design* regions are the manufacturing/functioning constraints. In addition to these regions, the model is subjected to a volume constraint as defined in Equation 6.3b.

6.3.5. Numerical Implementation

The simplified DOC model (the DOC model including the simplifications explained in Section 6.3.2) is implemented in ANSYS^{TM} and the DOC's volume is discretized in cube elements with a size of 3 mm. To describe the load case, a brief summary of the previous chapters is described here. ANSYS^{TM} topology optimization feature has some shortcomings: this software cannot perform topology optimization on random vibration analysis and therefore random vibration analysis will be used to validate the results of the optimization in Chapter 8. The power spectrum density (PSD) is converted to acceleration and the acceleration is applied in the - x-, x-, and z-directions. The topology optimization is applied on the three static structural analyses combined with optimizing for natural frequencies (modal analysis). In total, six potential mounting locations were defined for the DOC, as explained in Section 5.3. For each location, a topology optimization is carried out. Additionally, for the current design (see Table 5.4), and for a combination of all the load cases, the optimization is executed. The eight load cases are as follows.

- Load case one: Three static structural analyses, and one modal analysis for the Ariane 5 load;

- Load case two: Three static structural analyses, and one modal analysis for the Attitude and Vernier Upper Module (AVUM) load;

- Load case three: Three static structural analyses, and one modal analysis for the Payload Adapter (PLA) load;

- Load case four: Three static structural analyses, and one modal analysis for the Vega Secondary Payload Adapter (VESPA) load;

- Load case five: Three static structural analyses, and one modal analysis for the Zefiro 9 load;

- Load case six: Three static structural analyses, and one modal analysis for the Soyuz load;

- Load case seven: Twelve static structural analyses, and one modal analysis for the current DOC worst case scenario; The static structural analysis loads are imposed by the Ariane 5, the PLA, the Soyuz, and the Zefiro 9;

- Load case eight: Eighteen static structural analyses, and one modal analysis for a combined load case. The static structural analyses loads are imposed by the all six locations.

In the topology optimization system, the mass is selected as the optimization objective. To compare the results between optimizing only the HVI or a combination of the HVI and the front shell, per load case two topology optimizations are conducted. First, the HVI is selected as a *design* region where 122 surfaces are excluded and the front shell is selected as a *non-design* region. Second, the HVI and the front shell are selected as a *design* regions where 163 surfaces are excluded. In the analysis settings cell, the convergence criterion for the optimization process is assumed to be 0.1%, which in consultation with S[&]T experts, was found to be a reasonable value. Additionally, a maximum of 500 iterations were set up. Once, the optimization process reaches either the maximum iteration or converge to 0.1%, it will stop proceeding and the optimized configuration is obtained. In total, sixteen topology optimization cases were executed. In Appendix A.8, the topology optimization set up of Ariane 5 is shown.

<div style="text-align: right; font-size: 3em;">7</div>

Optimization Results

In the previous chapters, several steps were conducted to optimize the Demise Observation Capsule (DOC). First, a list of potential locations to mount the DOC was established. Then, the most critical load applied per location was defined. After that, the DOC model was described and the static structural, modal, and random vibration analyses results were explained. Finally, topology optimization method was conducted on the DOC model. This all led to this chapter where the results of the topology optimization will be described. Section 7.1 indicates the results of the topology optimization for the eight load cases. The results obtained from the topology optimization require post-processing effort to obtain feasible designs and will be outlined in Section 7.2.

7.1. Topology Optimization

This section describes the results of the topology optimization analysis before post-processing. As explained before, the host vehicle interface (HVI) and the front shell (FS) can both be optimized. The HVI has a lower volume percent in the *non-design* region compared to the FS. Since it was not clear whether including the FS in the *design* region would reduce the total mass, the *design* region of the optimization was divided into two separate analyses. In the first analysis, the HVI and the FS were selected as a *design* region and the final results are shown in Table 7.1. In the second analysis, only the HVI was selected as a *design* region and the topology optimization results are illustrated in Table 7.2. Let us call them case A and case B, respectively. Tables 7.1 and 7.2 indicate for all eight load cases the final mass after optimization, the mass reduction of the related parts in percent, and the total structural mass reduction in percent for case A and case B. It is decided to round the mass results to four decimal places, since the results differ in the third digit.

In case A, the most promising finding is that the mass of the HVI and the FS can be reduced by 20.89% to 20.95% of their initial masses and 7.76% to 7.78% of the total structural mass. Furthermore, the results demonstrated that the final masses are very close to each other; specially, in the first seven cases. They are similar to their second rounded decimal place. Additionally, the results between cases seven and eight were compared to cases one through six. It was concluded that their final masses are very close to each other and the differences are insignificant.

In case B, the same approach was used to establish the findings. The mass of the HVI can be reduced by 33.63% to 34.88% of its initial mass. A similar conclusion was reached, as in case A, the final optimized masses were very close and the difference between cases seven and eight compared to cases one through six were less than 1%.

Comparing case A and case B, it was found that when optimizing the HVI only, the HVI mass reduction is higher than the HVI final mass in case A. However, when comparing the results from the fourth column of the Tables 7.1 and 7.2, it can be concluded that case A reduces the total structural mass more. Case A, the HVI and the FS both as a *design* region, clearly gives better results than case B, therefore, it is decided to proceed with case A.

Table 7.1: Topology Optimization Results of the HVI and the FS *Design* Regions

Load case	Optimized Mass of HVI and FS [kg]	Reduced Mass [%]	Total Mass Reduced by [%]
One	1.4196	20.9366%	7.7836%
Two	1.4195	20.9421%	7.7856%
Three	1.4195	20.9421%	7.7856%
Four	1.4196	20.9366%	7.7836%
Five	1.4196	20.9366%	7.7836%
Six	1.4193	20.9533%	7.7898%
Seven	1.4196	20.9366%	7.7836%
Eight	1.4204	20.8920%	7.7670%

In addition to the final numbers, the visual results were compared. The plots are illustrated in Appendix A.9 for all eight load cases (see Figures A.57 to A.72). The visual results are directly in line with previous findings. The results from the visual plots are very similar to each other. Some major similarities and differences are explained below.

Looking at case A, the optimized front shells of all eight cases are compared. The comparison clearly shows that the optimized front shells of all cases are the same. Figure 7.1 shows the optimization results of the Ariane 5. Four edges remain in the design at the locations where the four cylindrical legs of the HVI would be present. These edges are indicated in red. Comparing the HVI shows that the side view is very similar in all cases. Figure 7.2 shows the side view of Ariane 5 and the red circles indicate its similarities with the other seven cases.

The major differences are found in the side where the HVI camera and the HVI thermal protection system (TPS) are mounted to the HVI. Figures 7.3 to 7.10 show the differences indicated in red. Looking at the bottom part, in load cases one, four, five, seven, and eight only a thin and long part is removed while in the remaining cases, halve an oval is removed from the bottom part. Looking at the top part in the first seven load cases, the HVI camera and the HVI TPS are supported with the bar shape at the left side. In load cases two, three, and six this bar is broader and can even be categorized as a thin beam. In load case eight, when it is optimized for all load cases at the same time, the HVI camera and the HVI TPS are supported by two bars from left and right. Additionally, a similarity is noted in the support legs of the HVI. A trapezoidal form can be removed from these legs in all eight cases showed in green.

The visual results of case A and case B are consistent with what has been found in Tables 7.1 and 7.2. Figures 7.11 and 7.12 illustrates the topology optimization results of Ariane 5 case A and B, respectively. The figures provide evidence that the HVI mass reduction in case B is higher than the HVI final mass in case A. The differences are indicated in red. Clearly, case A result have some additional part in the HVI to compensate for the reduced mass in the FS.

The results revealed by the topology optimization approach is summarized as follows. The final masses and the visual results found clear support that having a generalized model is possible, since the differences between the results of the eight load cases are insignificant. Producing the optimized DOC per location will cost a lot of time and effort while generalized DOC will allow for mass production. Mass production ultimately results in lower labor cost, test, and production costs. Therefore, load case eight was selected as the final configuration, since this model was optimized for all load cases at the same time. Additionally, the results show that an optimized generalized model is not the same as the result of an optimized worst case scenario with the largest load (thus load case two, when the DOC is mounted on the Attitude and Vernier Upper Module (AVUM)). Finally, the similarities of the topology optimization results found evidence that the DOC structure is not so sensitive to the load cases after all. While, the optimized configuration is sensitive to the connection between the back shell and the HVI. This will be investigated in more details in Sections 9.1 and 9.3.

7.2. Feasible Design

In this section, the topology optimization model of case eight is the input. Depending on the machining process and the materials selected, some requirements are imposed on the model. Therefore, the optimized
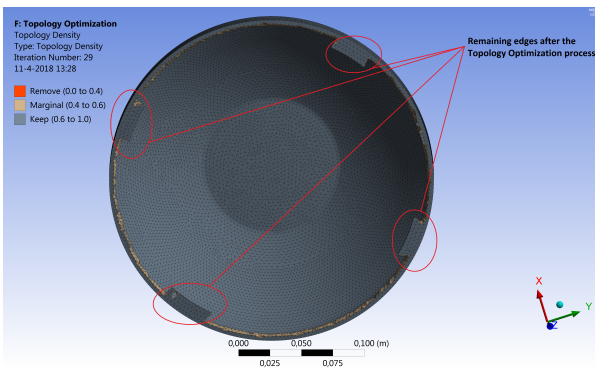
Figure 7.1: Front Shell Topology Optimization of all Eight Cases
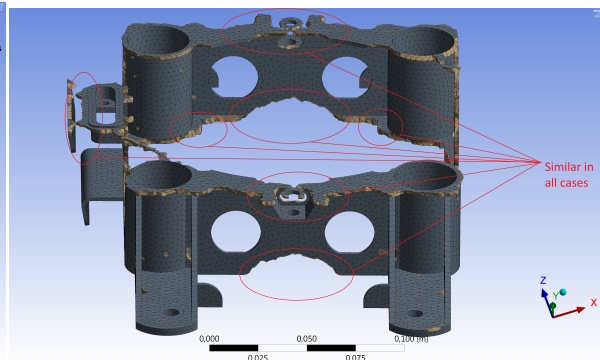
Figure 7.2: Side View of the HVI of all Eight Cases, Case A
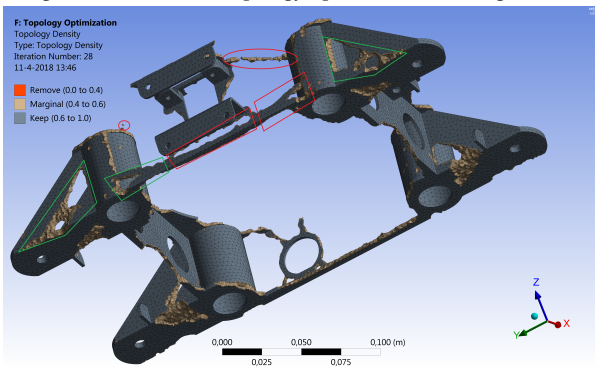
Figure 7.3: Topology Optimization Result of the Load Case One
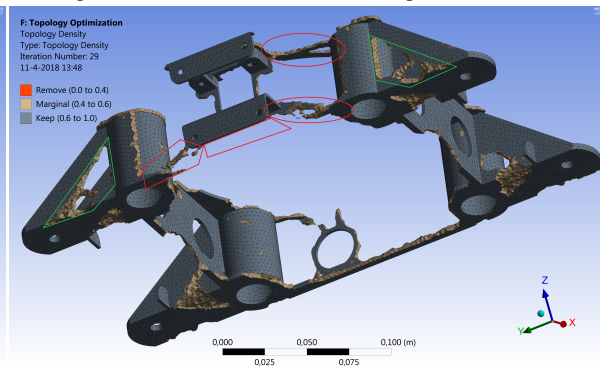
Figure 7.4: Topology Optimization Result of the Load Case Two
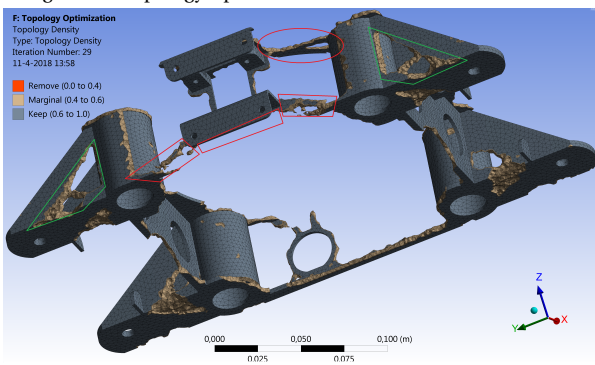
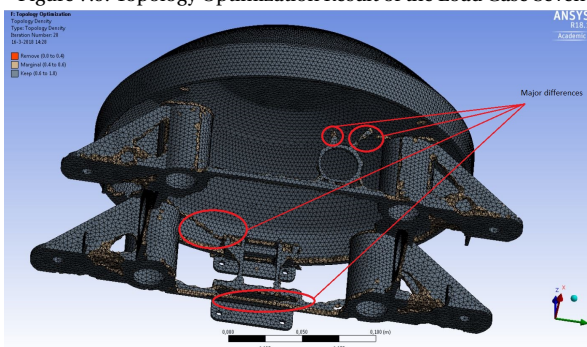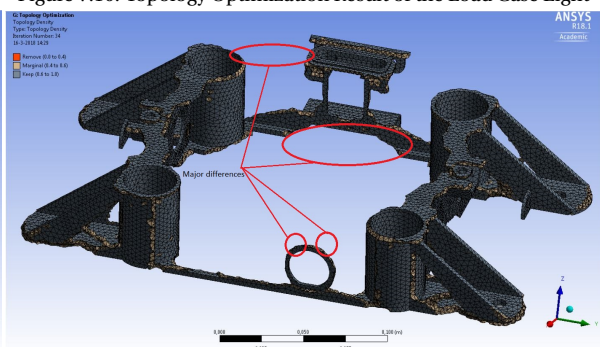Figure 7.5: Topology Optimization Result of the Load Case Three
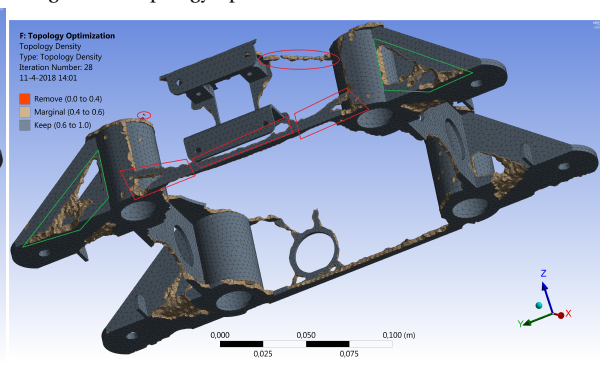
Figure 7.6: Topology Optimization Result of the Load Case Four
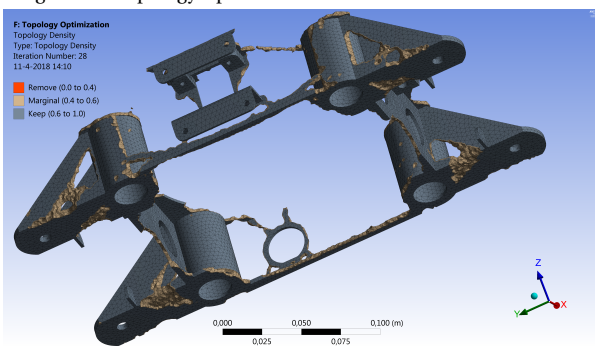
Figure 7.7: Topology Optimization Result of the Load Case Five
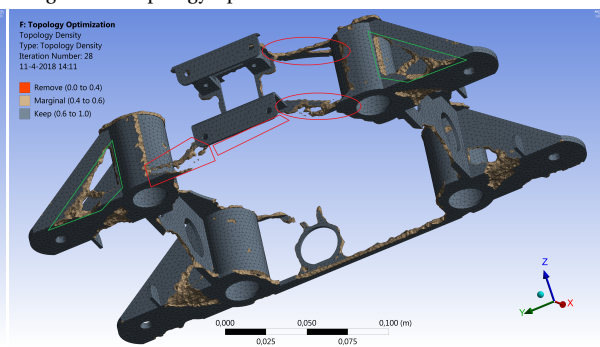
Figure 7.8: Topology Optimization Result of the Load Case Six

Table 7.2: Topology Optimization Results of the HVI *Design* Region

Load case	Optimized HVI	Reduced Mass [%]	Total Mass Reduced by [%]
1	0.62568	34.7802%	6.9086%
2	0.62568	34.7802%	6.9086%
3	0.62463	34.8896%	6.9303%
4	0.62568	34.7802%	6.9086%
5	0.62568	34.7802%	6.9086%
6	0.62463	34.8896%	6.9303%
7	0.62568	34.7802%	6.9086%
8	0.63666	33.6356%	6.6812%
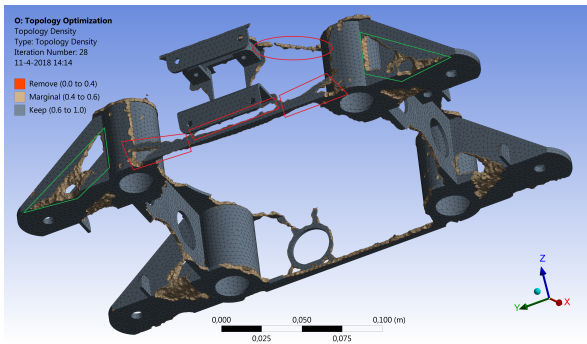
Figure 7.9: Topology Optimization Result of the Load Case Seven
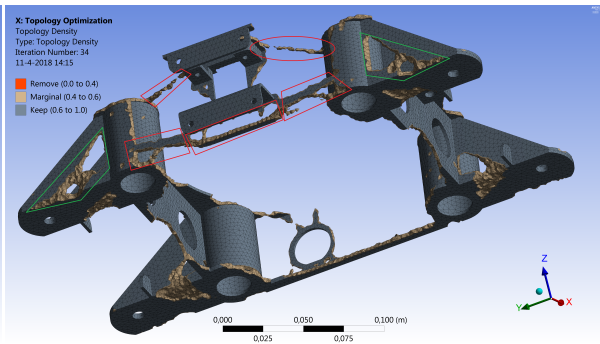
Figure 7.10: Topology Optimization Result of the Load Case Eight

Figure 7.11: Topology Optimization Results of Ariane 5, the HVI and the FS as a *Design* Region

Figure 7.12: Topology Optimization Results of Ariane 5, the HVI as a *Design* Region

Table 7.3: The Initial, Optimized, and Feasible Masses of the Two Optimized *Design* Bodies

Body	Mass [Kg]		
	Initial	Optimized	Feasible
Front shell	0.83619	0.7312	0.8012
HVI	0.95934	0.6891	0.73598
Total	1.7955	1.4202	1.5372

model is redesigned to produce a feasible design and is described in Section 7.2.1. The centre of mass of the initial model and the final feasible design is computed in Section 7.2.2. Finally, in Section 7.2.3 a new design is proposed for the current DOC model.

7.2.1. Final Design

The results of the topology optimization can be too costly to produce or it is simply not possible to manufacture. To address this concerns, a new feasible design based on the topology optimization results and the manufacturing constraints are made in Catia. Then, further simulation analyses are conducted on the new feasible model. To obtain a feasible design, user manuals (*Arcam A2X, setting the standard for additive manufacturing*, 2017; Roy, 2013) of the manufacturing machine, Arcam A2X, were studied. In addition, the experiences Gardi et al. (2016) and Borrelli et al. (2015) had with the Arcam A2X were reviewed to get a better understanding about the application of manufacturing process and the constraints applied by the material properties on the manufacturing machine. The Arcam A2X is used for additive manufacturing for the DOC prototype and will be used for the sequential DOC. The Arcam A2X can produce any configuration by building up layer-by-layer of Ti6AI4V powder melted by a powerful electron beam. Each layer is melted to the exact geometry dictated by the 3D CAD model. Although, the parts can obtain any configuration, some limitations are imposed by the manufacturing on the feasible design. Those are as follows:

Feasible-Design-1 Loose or disjointed bodies/fragments less than 2 mm^2 shall be removed;

Feasible-Design-2 Loose or disjointed bodies/fragments less than 2 mm^2 that are in continues line of other disjointed fragments shall be strengthened by adding mass and thus continuing that part;

Feasible-Design-3 The minimum thickness of all plates shall be 0.5 mm.

Requirement **Feasible-Design-1** imposes that the bodies/parts that are loose or very small should be removed because they are hard to be manufactured. While for the safety and compensation reasons, in requirement **Feasible-Design-2** the same fragments, when they are in a continuous area (meaning that multiple fragments exist in a limited area), are made larger and continuous in the feasible design than the results of the topology optimization. Figure 7.13 visualizes the meaning of the first two feasible design requirements. The blue color here indicates the parts that will be removed and red implies that the parts will be re-designed to be larger in order to make the final model feasible.

In addition to these requirements, the DOC should meet other design requirements too. The back shell is connected to the FS by twelve screws as illustrated in Figure 7.14. Although in Figure 7.1, the optimized FS only has four edges, in the feasible design the FS edge is designed to have twelve edges instead of four. The final design of the FS is illustrated in Figure 7.15.

The final feasible design of the HVI is illustrated in Figure 7.16. Table 7.3 indicates the initial mass, the mass after topology optimization, and the mass of the feasible design of the two *design* regions, the FS and the HVI.

7.2.2. Center of Mass

In order to define the center of gravity of the DOC, a simplified model is assumed. Since the relative shift of center of mass between initial design and the feasible optimized design is important, the lumped masses are not taken into account. Lumped mass locations and their mass will be constant after optimization. To define the center of mass, the following equation is used:

$$\overline{CoM} = \frac{1}{M} \sum_{i=1}^{4} m_i \overline{r_i} \tag{7.1}$$
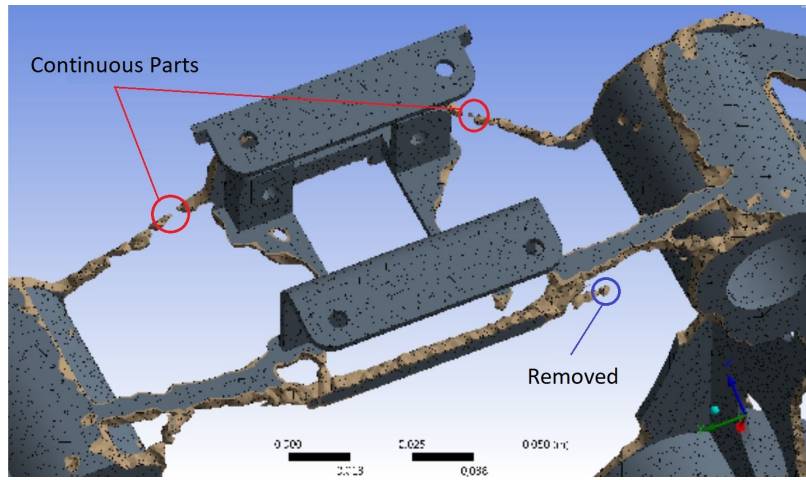
Figure 7.13: Indication of the Two Feasible Design Requirements on the Case Eight Topology Optimization Results
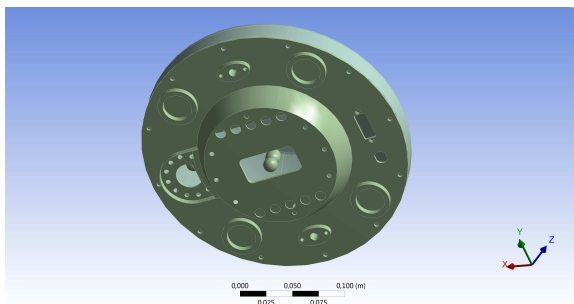
Figure 7.14: Connection Between the Back Shell and the FS Accomplished by Twelve Screws
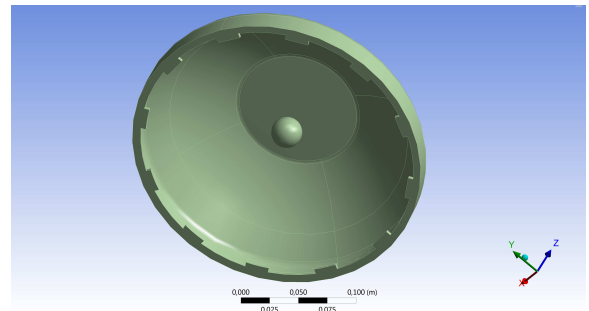
Figure 7.15: Final Feasible Model of the FS with Twelve Edges for Fixation Reasons
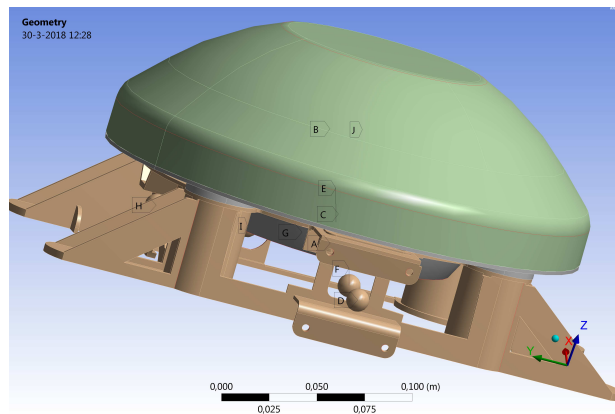
Figure 7.16: Final Feasible Model of the HVI

Table 7.4: Discretized Bodies, Their Masses and Coordinates

Body	Initial Mass [kg]	Coordinates [mm]			Feasible Mass [kg]	Coordinates [mm]		
		x	y	z		x	y	z
Front Shell	0.83618	76.77	0.021804	83.915	0.8012	76.82	0.02215	83.915
Back Shell	0.61234	75.477	0.0333	79.714	0.61234	75.477	0.0333	79.714
HVI	0.95934	73.983	1.0595	77.138	0.73598	73.618	4.405	75.976
Ballast	2.4218	77.86	-0.051802	87.06	2.4218	77.86	-0.051802	87.06

where $\overline{CoM}$ is the coordinates of the center of mass, M is the summation of masses, m_i is the mass of the part with coordinates $\overline{r_i}$.

The mass and coordinates of the four distributed mass bodies are given in Table 7.4. First the properties of the initial model are given, then the properties of the feasible design. The initial center of mass with respect to the DOC geometric reference frame is [77.25 , 0.0067 , 85.22] mm. The center of mass excluding the HVI part is [76.60 , 0.0261 , 83.62] mm. Using Equation 7.1, the current center of mass with respect to the DOC geometric reference frame is [77.26 , 0.0044 , 85.05] mm. The center of mass excluding the HVI part is [76.67 , 0.0034 , 83.59] mm.

To shift the center of gravity to the nose of the DOC, the distance in the z-direction should be reduced. By optimizing the mass of the HVI and the FS, the center of gravity is shifted towards the front by 0.0263% for the four bodies. For the FS, back shell, and ballast, the center of gravity is shifted by 0.1944% to the front.

7.2.3. New Design for Current Case
As explained in Section 1.2, the initial model was not approved by ESA since it was not stable. This means that the center of mass should be shifted towards the nose of the DOC for a more stable vehicle. Any movement of the center of gravity to the nose is considered as a positive result.

It should be noted that the DOC will be ejected from the host vehicle and re-enter the Earth without the HVI part. Therefore, even though the mass of HVI is reduced by 23.3%, this mass reduction will not shift the center of mass. Therefore, the mass reduced by optimizing the HVI is added to the ballast. Hence, the new center of gravity of the DOC is improved by 8.1%. In Figure 7.17, the center of gravity of the initial model, the optimized feasible model, and finally the new model for the current case is shown.
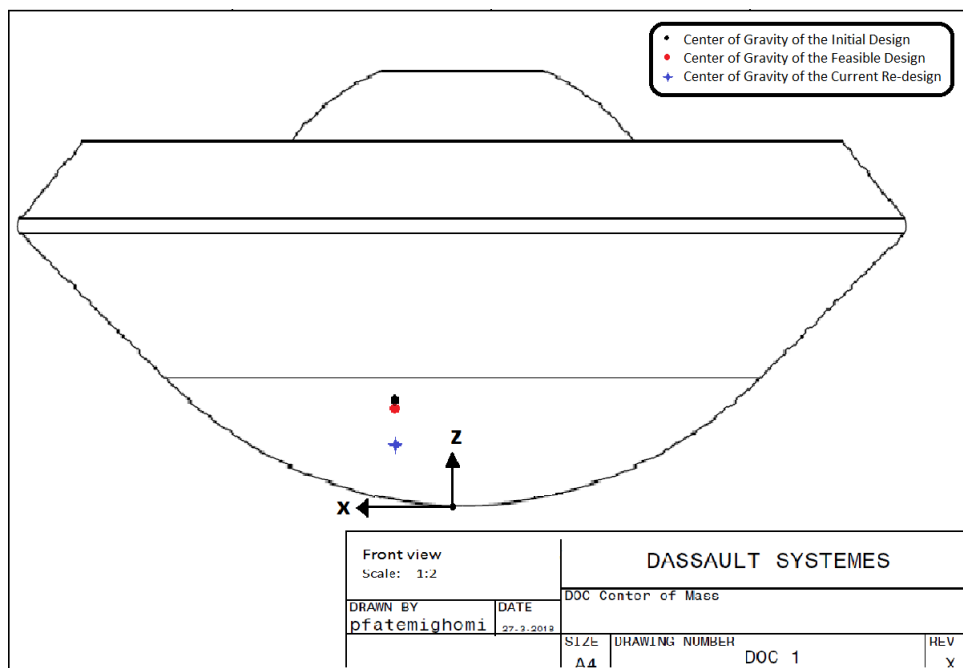
Figure 7.17: Catia Drawing of the DOC Including the Center of Gravities

8
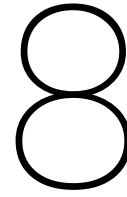
Verification and Validation

Simulation models were used to solve the problems and to aid in the decision making process. The conclusions were made based on these results and it is a concern whether the results are reliable and correct. These concerns are addressed by verifying and validating the model. In each phase of this thesis, a verification analysis is conducted. In this chapter, the MATLAB code of the input loads are verified and described in Section 8.1. Section 8.2 verifies the reproduced model. Section 8.3 validates the final feasible model and checks whether or not the results meet the requirements.

8.1. Verification of MATLAB Codes of the Input Loads
In Chapter 3, the loads were defined per location and converted from sound pressure levels (SPL) to the power spectral density (PSD), the acceleration spectral density (ASD), or were converted from the PSD to the acceleration. The conversion is verified as follows.

ESA-ESTEC (2013) describes the Spann method and explains this method by an example of the acoustic noise spectrum under fairing of the Ariane 5. The MATLAB code, which converts the SPL of the potential stages to the PSD, is verified by using the inputs of this example and comparing the outputs of the code with the example results. The results are identical to that of the example and therefore, the code was verified.

The MATLAB code converting the PSD to the acceleration was verified by comparing the PSD of the Ariane 5 acoustic noise to the acceleration graph result of the Ariane 5 in, *Aerothermodynamics, thermal and structural design, definition and justification file*[1], that was provided by S[&]T. Figure 8.1 shows the plot from this internal file. Figure 8.2 illustrates again the result of converting the SPL to PSD and acceleration obtained in this thesis. Since the final graphs were identical, it was confirmed that the code was verified.

Additionally, the MATLAB code converting the PSD to the ASD was verified by using ANSYS^{TM}. Two random vibration analyses were carried out in ANSYS^{TM}: one with the PSD of Ariane 5 as the input load and the other one with the ASD of Ariane 5 as the input load. The input ASD result was obtained from the MATLAB code converted from the PSD. The stress distribution maps of both random vibration analyses were identical, therefore, the MATLAB code was verified to be functioning properly.

8.2. Verification of the Input Model
As explained before in Section 5.1, the Catia geometry model was given by S[&]T in a (.CATPart) file which was converted to an (.agdb) file to be able to import into the ANSYS^{TM}. Then, the model was simulated as explained in Chapter 4.

The current model of the DOC was already simulated for the Ariane 5 launcher by the S[&]T experts and the results are presented in *Aerothermodynamics, thermal and structural design, definition and justification*

---

[1]Aerothermodynamics, thermal and structural design, definition and justification file, Issue date: Augustus 8, 2017. This is a classified document and only available through S[&]T
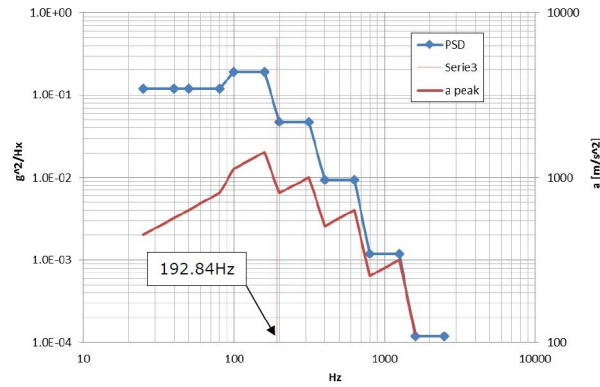
Figure 8.1: S[&]T Internal File Result of Converting SPL to PSD and Acceleration of Ariane 5
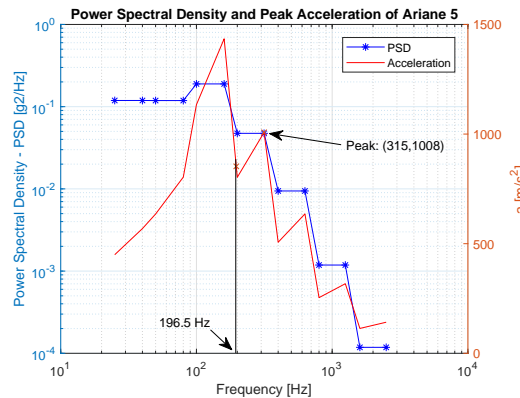
Figure 8.2: This Research Result of Converting SPL to PSD and Acceleration of Ariane 5

file. This file reported the results of the maximum deformation of the static structural analysis and the natural frequency of the modal analysis. The reproduced model was compared to these results. Figure 8.3 illustrates the maximum deformation in the - x-, x-, and z-directions of the static structure analysis. Figure 8.4 indicates the natural frequency of the first six modes of the modal analysis. In these figures, the results of the company were called *given model* and the results of this thesis model were called *reproduced model*.

Comparison of the results of the given model and the reproduced model, shows that there is small deviation when the model is reproduced. The largest anomaly was by 3.27% in the maximum deformation in the - x-direction of static structural analysis. This small deviation may be due to the number of elements when conducting the finite element analysis. In S[&]T's file, 107950 elements were selected, while in this thesis more than two times as many elements, 235454 elements, were selected. Therefore, the deviation can be due to the fact that this thesis's results are more accurate. In a conversation with the experts at S[&]T, it was decided that this was not an issue and hence the reproduced model was concluded to be verified.

8.3. Validation of the Topology Optimization Results

In this section, the optimized feasible model described in Section 7.2.1 is validated. The feasible geometry in Catia was converted to an (.agdb) file, then it was imported into ANSYS^{TM}. The model was simulated as it was described in Chapter 4, without the topology optimization simplifications described in Section 6.3.2. For all six load cases, the feasible model was set up as in the Appendix A.5, for the static structural, modal, and random vibration analyses. The results of the modal, static structural, and random vibration analyses are described in Sections 8.3.1, 8.3.2, and 8.3.3, respectively.

8.3.1. Modal Analysis

A modal analysis has been carried out to validate the feasible model. The Requirements **Analysis-1-a** to **Analysis-1-c**, and the Requirement **Analysis-2** explained in Section 5.2 should be met by the new design too.
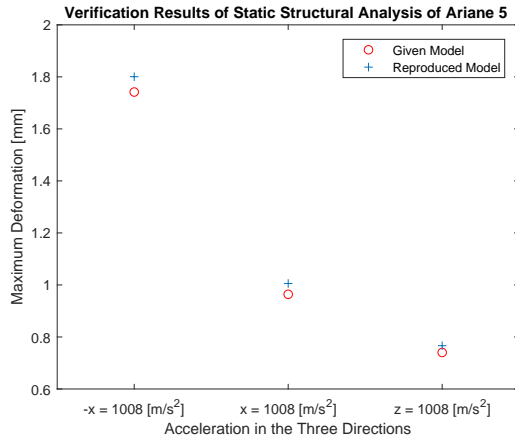
Figure 8.3: Verification Results of the Static Structural Analysis
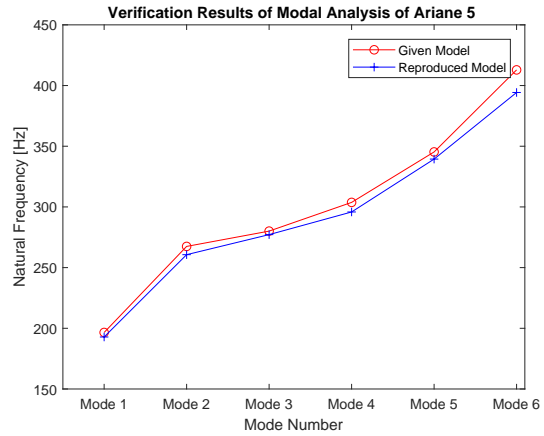
Figure 8.4: Verification Results of the Modal Analysis

Table 8.1: Natural Frequencies of the Feasible DOC at the First Six Modes

Mode	1st	2nd	3rd	4th	5th	6th
Frequency [Hz]	159.26	205.76	243.22	267.74	307.99	322.12

The first six modes of the feasible DOC are illustrated in Figures 8.5 to 8.10. These plots were compared with the plots in Figures 5.1 to 5.6. The first modes plots are similar. Both are the results of quasi rigid rotation of the capsule about the x-direction. The plots of the second mode are also similar, since the maximum deformation occurs at the same point on the back shell. The first difference starts at the third mode. It seems that mode three and four of the new results are the opposite to the previous results. Furthermore, in the initial model, the fifth mode was a global mode, while in the new model it is a local mode. The plots of the sixth mode are relatively close to each other, both are global modes.

Table 8.1 indicates the frequencies of the first six natural modes of the feasible DOC. The first mode occurs at 159.26 Hz, while in the initial model this value was 196.49 Hz. The first natural frequency is reduced by 18.9%, however the Requirements **Analysis-1-a** to **Analysis-1-c** are still met. This small reduction was expected, since by reducing the mass, the model gets less stiff than the initial model and therefore the natural frequency will be reduced.

Additionally, the Requirement **Analysis-2** imposed that the first global mode of the DOC shall be lower than its first local mode. Investigation of the first six modes shows that the first global mode occurs at 159.26 Hz, while the first local mode occurs after that at 205.76 Hz. Therefore, the results confirm that the Requirement **Analysis-2** is met.

To sum up, the results of the feasible model deliver the evidence that the model meets all the frequency requirements and therefore the feasible model is valid.

8.3.2. Static Analysis
The static structural analyses of the feasible DOC mounted on all six locations is carried out at the sizing equivalent acceleration level and described in this section. The Von Mises stress and deformation results of the static structural analyses in the - x-, x-, and z-directions are computed and described here.

The equivalent stress distribution maps show that in all six load cases, the whole structure is below the ultimate strength of the titanium alloy of 0.764 GPa. Figure 8.11 shows the stress distribution of the feasible DOC on the AVUM in the - x-direction. This confirms that the feasible model still is valid.

The maximum deformation of the initial model and the feasible model as a result of static structural analysis are illustrated in Table 8.2. This is shown for all six load cases, in the three aforementioned directions. It
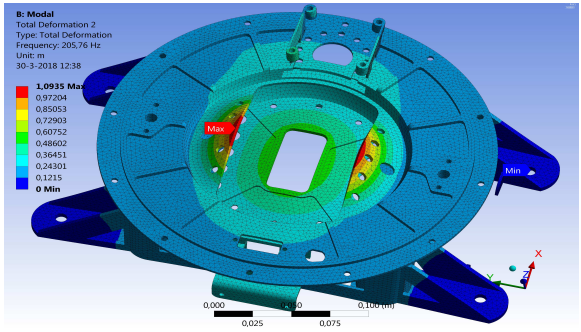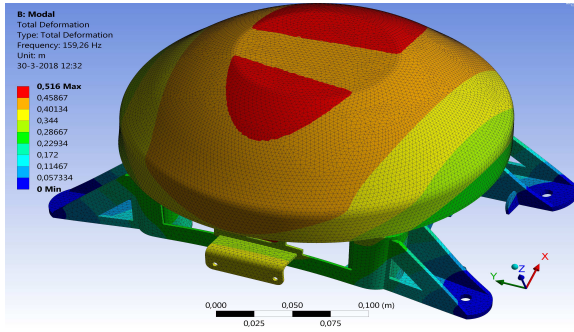
Figure 8.5: The First Mode of Modal Analysis of the Feasible DOC

Figure 8.6: The Second Mode of Modal Analysis of the Feasible DOC
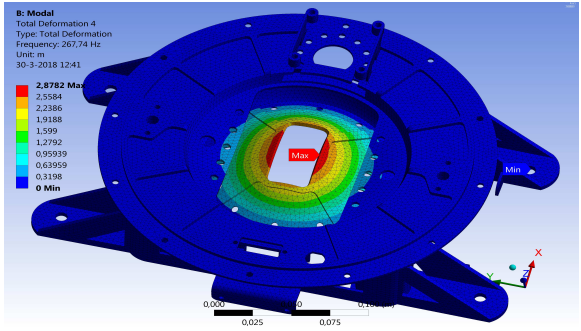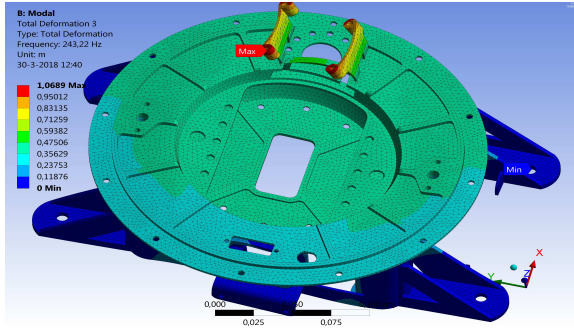
Figure 8.7: The Third Mode of Modal Analysis of the Feasible DOC

Figure 8.8: The Fourth Mode of Modal Analysis of the Feasible DOC
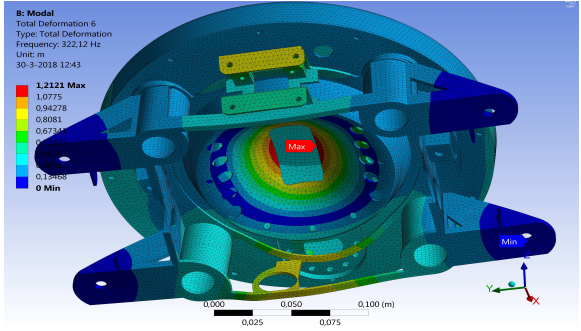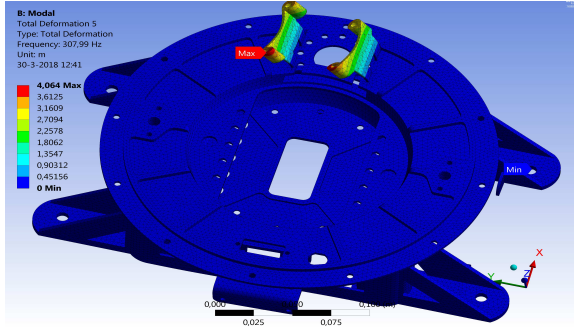
Figure 8.9: The Fifth Mode of Modal Analysis of the Feasible DOC

Figure 8.10: The Sixth Mode of Modal Analysis of the Feasible DOC

Table 8.2: Total Deformations and Force Reactions Results of Static Structural Analysis

Location	Axis	Deformation [mm]	
		Initial Model	Feasible Model
Ariane 5	-x-	1.749	2.837
	x-	0.9657	1.657
	z-	0.8863	1.487
AVUM	-x-	10.67	16.93
	x-	5.9011	9.612
	z-	5.4678	8.780
PLA	-x-	1.2158	1.980
	x-	0.67048	1.155
	z-	0.61552	1.033
VESPA	-x-	5.272	8.434
	x-	2.9155	4.875
	z-	2.6882	4.423
Zefiro 9	-x-	5.4947	8.796
	x-	3.0466	5.079
	z-	2.3495	4.609
Soyuz	-x-	1.013	1.653
	x-	5.585	0.9634
	z-	0.5127	0.8604

is clear that the deformation has increased. The largest deformation appears when the DOC is mounted on the AVUM. Therefore, only this case will be discussed in more detail.

Figures 8.12 to 8.17 visualize the deformation in static structural analyses in the - x-, x-, and z-directions while the DOC is mounted on the AVUM for both initial and feasible DOC configurations. In the - x-direction, the deformation map is very similar. The back shell is disconnected from the HVI on two sides. In the x-direction, the same conclusion is drawn. The feasible model in the z-direction shows buckling in the HVI, while in the initial model this was not the case. However, in the - x-direction a larger deformation was revealed and therefore, it is decided that the deformation in the z-direction is not critical.

It was presumed that the deformation in all initial and feasible models is due the disconnection of the HVI and the back shell. To investigate this, the disconnection of the HVI and the back shell in the z-direction is analysed. The four frictionless contacts between the HVI and the back shell are replaced by the bonded contacts. The deformation results in the z-direction when the DOC is placed on the AVUM are illustrated in Figure 8.18. The maximum deformation is 5.351 mm and the HVI does not experience buckling. This shows that the deformation in the initial and the feasible model is mainly due to the disconnection of the HVI and the back shell.

Additionally, as explained in Section 5.4, the vibration can move the HVI and the back shell far away and the Harwin M90-6061645 connector can get temporary disconnected. This connector has a strip length of 8 mm and the maximum deformation between the HVI and the back shell (at the point where the connector is located) should be less than the strip length. The deformations are with respect to the HVI reference frame and showed that in the - x-direction the maximum deformation over time is 10.6 mm, while in the x-direction is 5.9 mm. In the z-direction, this deformation was 3.2 mm. Comparing the deformation results at the connector point, shows that the deformation of the feasible DOC is almost two time larger than the initial DOC. The maximum deformation over time in the - x-direction of the feasible DOC is larger than allowed. The connector will experience disconnection. However, when an extra fixation is added between the HVI and the back shell, this value will be decreased to 6.7 mm. Since already in Section 5.4 was concluded that at least an additional fixation between the HVI and the back shell is required to mount the DOC on the AVUM, hence, it can be concluded that the feasible model is still valid.
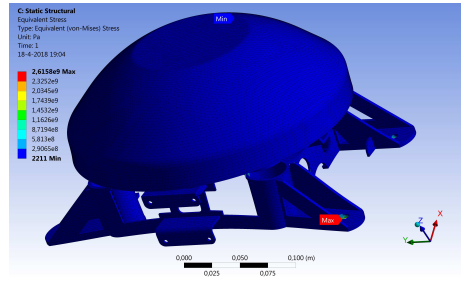
Figure 8.11: The Feasible DOC Stress Distribution of the Static Structural Analysis on the AVUM in the - x-direction
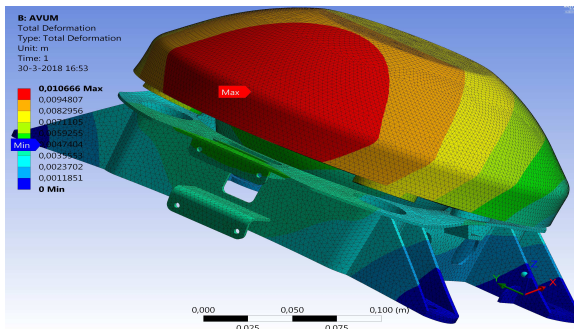
Figure 8.12: The Initial DOC Deformation Results of the Static Structural Analysis on the AVUM, Acceleration -x = 6226.9 m/s^2
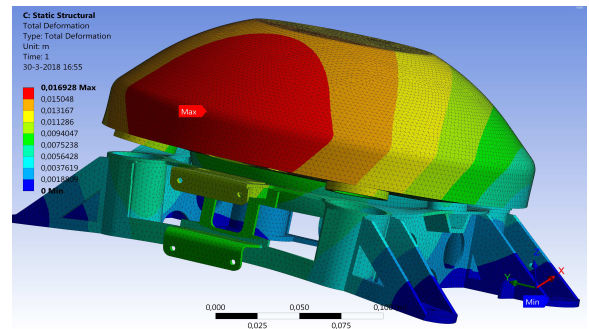
Figure 8.13: The Feasible DOC Deformation Results of the Static Structural Analysis on the AVUM, Acceleration -x = 6226.9 m/s^2
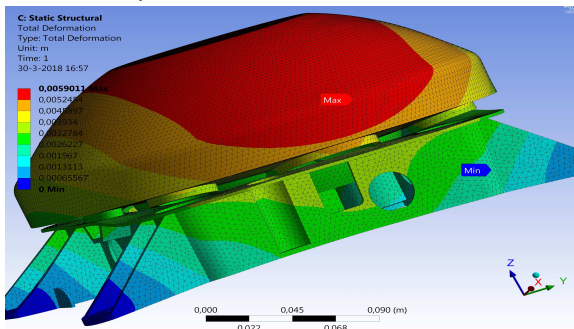
Figure 8.14: The Initial DOC Deformation Results of the Static Structural Analysis on the AVUM, Acceleration x = 6226.9 m/s^2
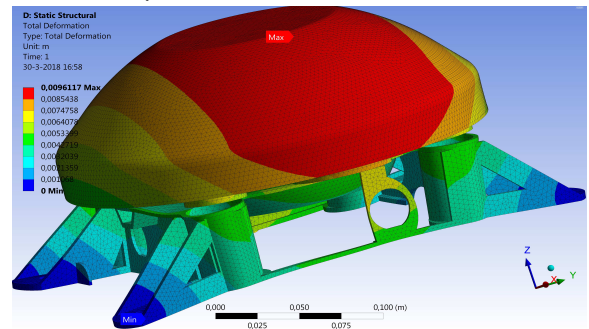
Figure 8.15: The Feasible DOC Deformation Results of the Static Structural Analysis on the AVUM, Acceleration x = 6226.9 m/s^2
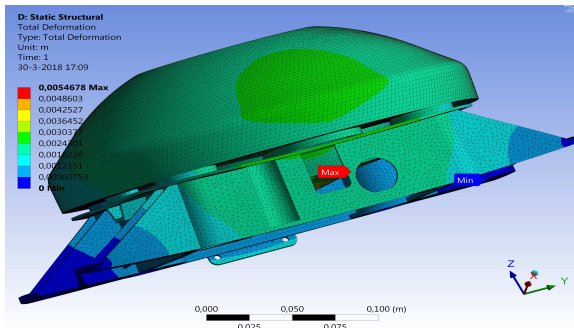
Figure 8.16: The Initial DOC Deformation Results of the Static Structural Analysis on the AVUM, Acceleration z = 6226.9 m/s^2
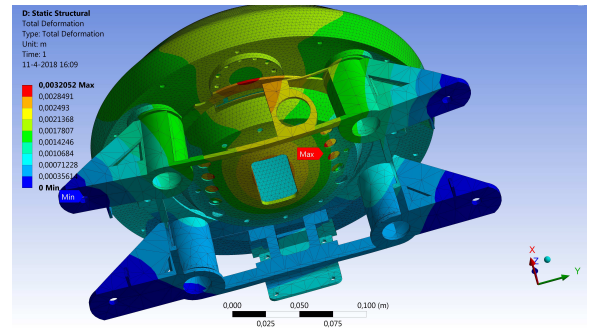
Figure 8.17: The Feasible DOC Deformation Results of the Static Structural Analysis on the AVUM, Acceleration z = 6226.9 m/s^2
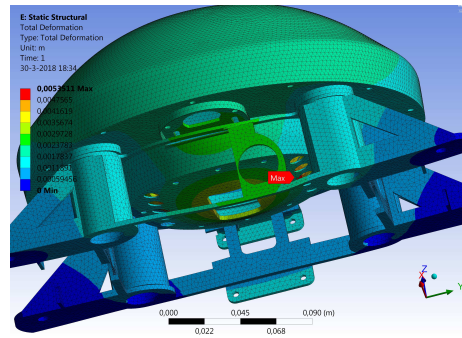
Figure 8.18: The Feasible DOC Deformation Results of the Static Structural Analysis on the AVUM When the Frictionless Is Replaced by Bonded Contacts, Acceleration z = 6226.9 m/s^2

8.3.3. Random Vibration Analysis

In this section, the 1-σ stress distribution results of the random vibration analysis are discussed. In this analysis, ANSYS^{TM} uses ASD directly and produces a stress distribution. Equivalent stress distribution maps of the feasible model show that the whole structure is well below the ultimate strength of titanium alloy, 0.764 GPa. The allowable stress is only exceeded in correspondence to the four holes of the screws that connect the HVI to the launch vehicle. These results are in line with the previous results in Section 5.5. Since all three analyses met the requirements, it was concluded that the feasible model is valid.

9

Sensitivity Analysis

After optimizing the structure, the design variables and their importance should be evaluated. By determining a cause-effect relationship between the objective and the design variable, the design variables can be prioritized, and the model can be checked and explored. To establish that, the objective function is differentiated with respect to the design variables. The procedure to achieve these derivatives is called sensitivity analysis. A sensitivity analysis is conducted on input loads, model simplifications, input model, and assumptions to define their uncertainty and robustness on the final mass (Campolongo et al., 2007).

The sensitivity analysis can be conducted either numerically or analytically. Numerical methods give an approximated solution while the analytical approaches are exact. Although, the numerical methods can be inaccurate, they are very easy to implement. Due to its ease of implementation, numerical analysis was used (Saltelli et al., 2004).

This chapter describes the sensitivity analysis of the Demise Observation Capsule (DOC). To determine the most influential factors in optimizing the DOC, the sensitivity of the input loads are obtained in Section 9.1. Next, the sensitivity analysis is applied to the simplification decisions during the analysis in Section 9.2. Finally, Section 9.3 investigates the sensitivity of the input model.

9.1. Input Loads

In this section, the sensitivity of the applied loads on the final mass is explored. The loads applied on the DOC when it is mounted on the launchers is presented as accelerations to be able to perform the topology optimization. There are two possible approaches to perform numerical sensitivity analysis, a forward difference and a central difference. While the forward difference method is an easier approach, the central difference approach is more accurate but also more costly (Christensen and Klarbring, 2009a). Due to the ease of the forward difference approach implementation, this method was selected. Recall the structural topology optimization in Equation 6.7. The forward difference of the approximation is:

$$\frac{\partial M(\mathbf{x})}{\partial a} = \frac{M(x+h) - M(x)}{h} \tag{9.1}$$

where h is the step size, a stands for acceleration, $\mathbf{x}$ are the design variables, and M is the mass. A too large h may show the truncation error and a too small h may increase the result of the Equation 9.1 dramatically, due to cancellation of h and give a numerical error.

The applied acceleration varies between 583 m/s^2 to 6226.9 m/s^2 due to the locations on the potential launchers. When h was assumed to be 4% of an initial load, the final optimized mass (the topology optimization objective) was not sensitive to it at all. Therefore, the step size is increased. Once the acceleration increased by 20%, the objective changed by 0.026%. The results lead to the conclusion that the optimized mass is not that sensitive to the applied loads.

Table 9.1: Deformation and Stress Results of Static Structural Analyses in the Y-direction

Case	1	2	3	4	5	6
Deformation [mm]	0.7939	4.863	0.5513	2.399	2.504	0.4591
Stress [Gpa]	4.376	27.008	3.039	13.27	13.85	2.531

9.2. Model Simplifications

In Section 5.2, it was concluded that the DOC is much stiffer in the y-direction than in the other two directions. This simplification was already assumed in the initial design of the DOC by S[&]T experts. The sensitivity of the final results due to this simplification will be explored here. To perform the sensitivity, the initial model is analysed in the y-direction.

Static structural analysis is performed for all six load cases, in the y-direction. The maximum deformation and stress results per load case is presented in Table 9.1. The deformation is the largest with AVUM and the smallest with Soyuz. This was expected since the load applied in the AVUM is the highest and the load applied by the Soyuz launcher is the lowest. The deformations of all cases were similar, therefore only the deformation result of the Ariane 5 is illustrated in Figure 9.2. The figure shows that the loads in the y-direction are not negligible. The two frictionless contacts between the HVI and the back shell are detached, however the bonded contact still holds these two parts together. Looking at the equivalent stress results in the y-direction illustrated in Figure 9.3, the equivalent stress distribution maps show that, in contrary to the stress distribution in the - x-, x-, z-direction, higher stresses are not only in the holes that fix the HVI to the host vehicle but also appears in the HVI. The results in the y-direction should be explored more. It was expected that the final optimized mass will be sensitive to this simplification.

Random vibration in the y-direction was also analysed and illustrated in Figure 9.4. The stress distribution of the whole structure is below the ultimate strength of titanium alloy and is therefore not of interest to explore further.

Looking at the topology optimization result of the Ariane 5 including the y-direction, major differences were found. Figure 9.1 shows the result. The differences are indicated by red.

Finally, the initial model was optimized for all six load cases including the static structural analyses in the y-direction to explore the robustness of the optimized final mass to this simplification. Both, the HVI and the front shell were indicated as *design* regions and in total, 163 surface were excluded. In other words, in case eight branch case B was optimized to include the loads in the y-directions. The final mass was found to be 1.4204 kg. The initial final mass of the topology optimization simplifying the loads in the y-direction was 1.4212 kg. This means that the final mass is sensitive to the y-direction loads by 0.0563%. Figure 9.5 shows the result of the topology optimization of the case eight and Figure 9.6 illustrates the topology optimization result of the case eight inclusive the loads in the y-direction. The red circles indicate the differences. At the lower part of the HVI, more mass is required when the y-direction loads are included.

9.3. Input Model

The input model was given by the S[&]T experts. Here, the sensitivity of the input model is analysed. It was already found that the HVI disconnects with the back shell at the four frictionless contacts. The model with frictionless contacts cannot be carried out in topology optimization in the software. Therefore, its effect on the final optimized mass can not be explored. However, in Section 6.3.2, modal and static structural analyses have been conducted on the model with either six bonded contacts between the HVI and the back shell or two bonded and four frictionless contacts. The model shows a lower deformation in the static structural analyses.

Additionally, the feasible model of the DOC when it is mounted on the AVUM was modelled by four frictionless and two bonded contacts, and the deformation result of the static structural analysis was shown in Figure 8.17. Figure 8.18 illustrates that there was no disconnection between the HVI and the back shell, once the four frictionless contacts were replaced by bonded contacts.
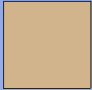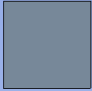
I: Topology Optimization y
Topology Density
Type: Topology Density
Iteration Number: 42
18-4-2018 20:01

Remove (0.0 to 0.4)

Marginal (0.4 to 0.6)

Keep (0.6 to 1.0)
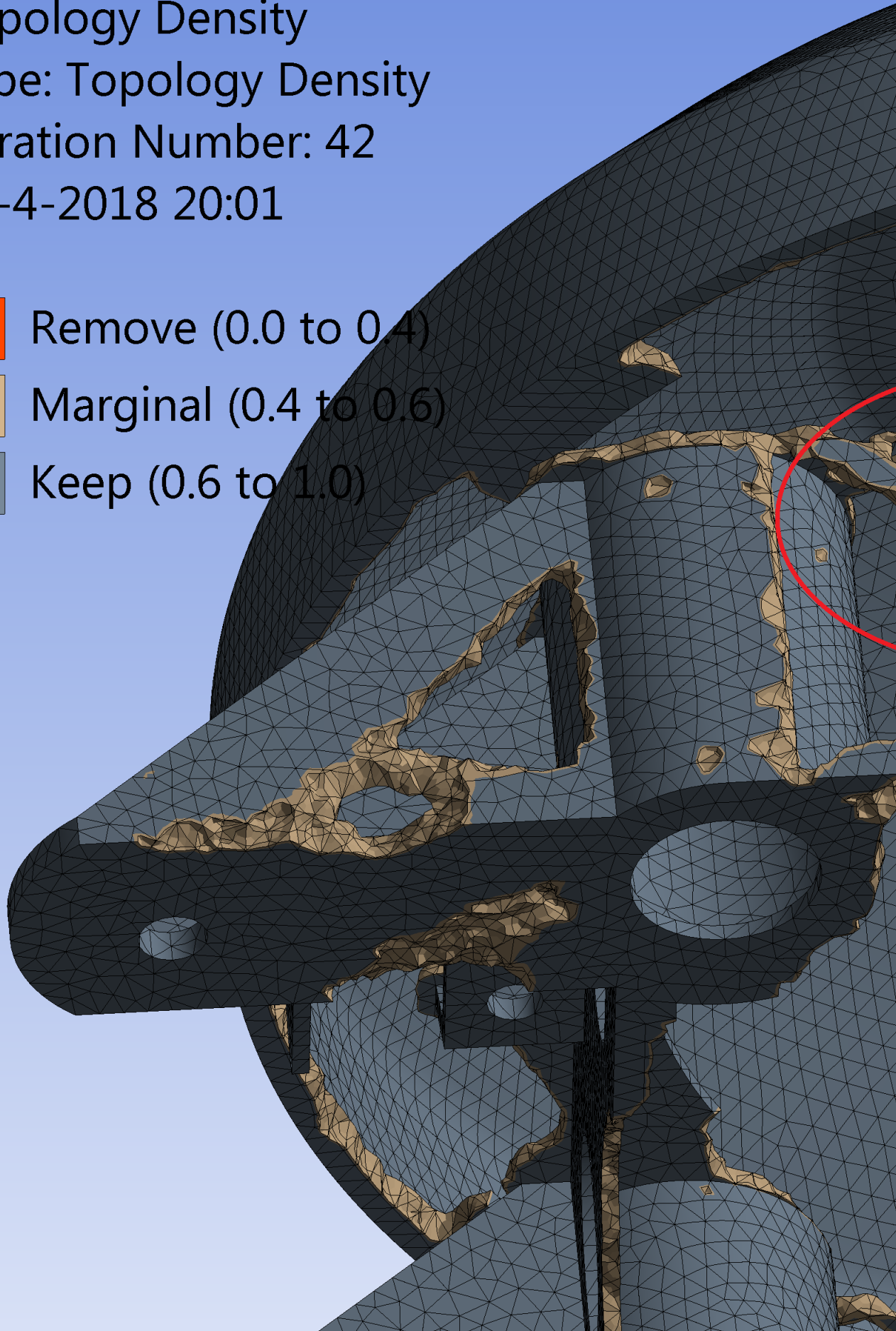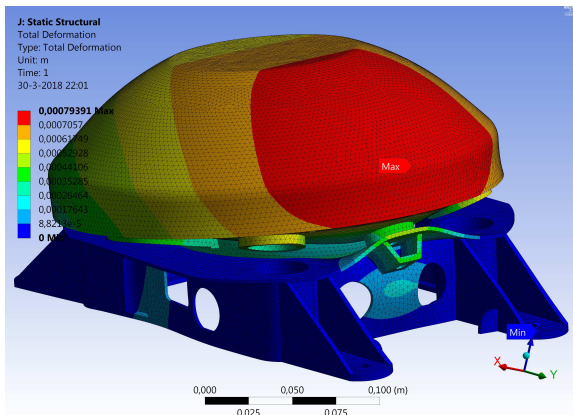
Figure 9.2: Deformation Result of Static Structural Analysis of the Ariane 5 in the Y-direction
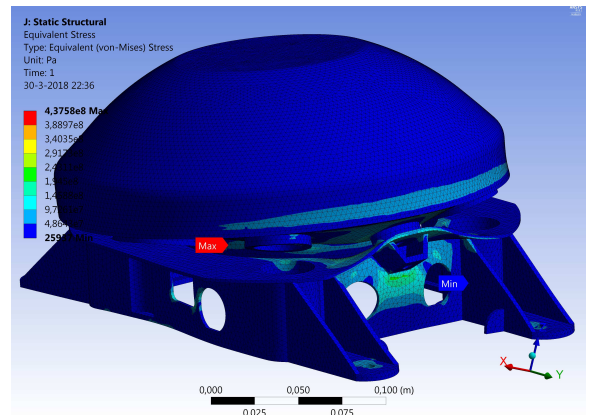
Figure 9.3: Equivalent Stress Result of Static Structural Analysis of the Ariane 5 in the Y-direction
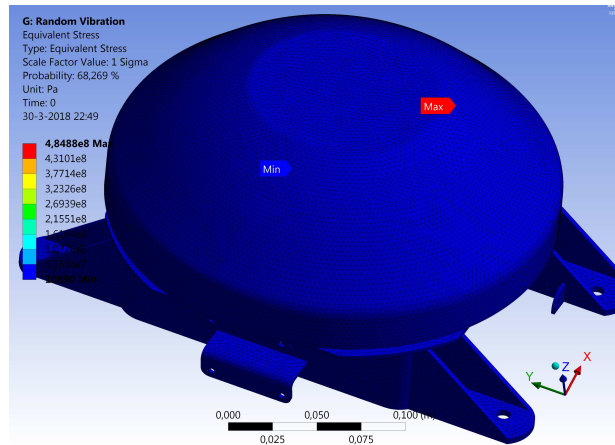
Figure 9.4: Equivalent Stress Result of Random Vibration Analysis of the Ariane 5 in the Y-direction
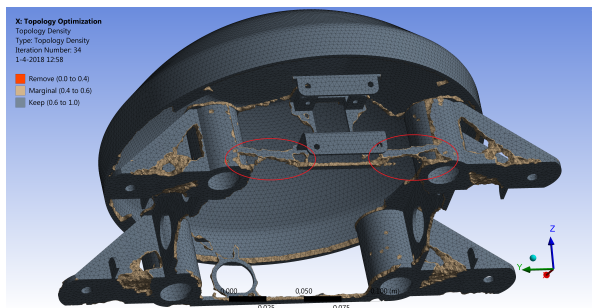
Figure 9.5: Topology Optimization Result of of Case Eight Excluding the Y-direction Load Analyses
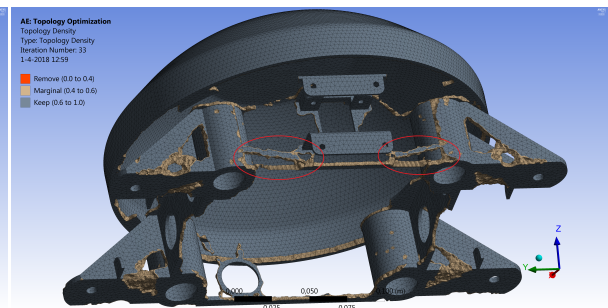
Figure 9.6: Topology Optimization Result of of Case Eight Including the Y-direction Load Analyses

It was concluded that the results are very sensitive to the connections between the HVI and the back shell. However, this is not due to the modelling decisions but due to the design decisions during the initial detail phase. Since the initial model was given, the simulation can not be improved. The only possible solution is to redesign the connection between these the HVI and the back shell by, for example, adding two bonded contacts to the other sides.

10

Conclusion and Recommendation

10.1. Conclusion

The conclusion of this thesis is divided into nine parts. The eight sub-questions followed by the main research question of Section 1.3 are answered here. This section confirmed the fact that all research questions are answered in this thesis report.

The Demise Observation Capsule (DOC) can be placed on the main cryogenic stage (EPC) and upper composite (UC) of the Ariane 5; the Zefiro 9, and Attitude and Vernier Upper Module (AVUM) of the Vega launcher and finally on the third stage and Fregat of the Soyuz launcher.

Due to the small dimensions of the DOC, its transport to the launch location is considered easy and by sufficient packaging, the loads applied during the transport will be lower than the loads applied during the ascent and re-entry phase. The loads during the re-entry phase are due to the dynamic pressure and the related deceleration, which are lower than that of the ascent phase. Therefore, the ascent loads are the largest loads applied on the DOC. When the DOC is placed on the Ariane 5, the acoustic load during the firing of the engines is the highest. The acoustic pressure fluctuations during lift-off of the Vega are critical when the DOC is mounted on the Payload Adapter (PLA), the shock loads due to stage separation are highest when it is placed on the Vega Secondary Payload Adapter (VESPA) and AVUM. When the DOC is placed on the Zefiro 9, the DOC is exposed to high random vibrations due to a unknown source. When the DOC is mounted on the Soyuz, the random vibration is the most critical load applied on the DOC. Additionally, the current model (the initial model by S[&]T) of the DOC was designed for these four locations; on the Ariane 5, PLA, Zefiro 9, and Soyuz. In the current design, the Zefiro 9 was defined as the worst case scenario, while in this thesis the AVUM applies the largest loads on the DOC.

The DOC was simulated in ANSYS^{TM}, by modelling the four load carrying parts: the front shell, back shell, ballast, and host vehicle interface (HVI), as discretized volumes. The other subsystems, which are mainly used to protect the DOC against the heat or are there to perform its mission objective such as cameras, etc., were modelled as lumped masses. The ballast was connected by bonded connection to the front shell, the front shell was connected to the back shell by the same connection. The back shell was connected by two bonded contacts and four frictionless contacts to the HVI. Finally, the HVI was fixed to the host vehicle by four screws. Modal, static structural, and random vibration analyses were conducted on the model. The stress distribution shows that the whole structures is well below the ultimate strength of the titanium alloy except on the fixation holes between the HVI and the host vehicle due the numerical singularity. Additionally, static structural analyses conclude that the DOC needs additional fixations between the HVI and the host vehicle when it is mounted on the AVUM, VESPA, and Zefiro 9. Furthermore, the HVI and the back shell should be connected by an additional fixation when DOC is located on the AVUM. In order to mount the DOC on these six locations, the two mentioned problems should be solved.

The structure was optimized by the topology optimization approach using a density based method called Solid Isotropic Material with Penalization (SIMP) method. The model was simplified to be able to carry on

the topology optimization in ANSYS^{TM}. The applied loads were converted to forces and were applied to the closest point to the center of mass, on the back part of the ballast. The four frictionless contacts between the HVI and the back shell were replaced by the bonded contacts. The HVI and the front shell were indicated as *design* regions and in total, 163 surfaces of these two bodies were excluded from optimization. The structural mass reduction was the objective of the optimization and it was decided to exclude the aerodynamic and thermal protection discipline areas.

The optimized final mass of the DOC varied by 0.01% per location. The final mass of the generalized case (load case eight) was higher than the highest load case (load case two, when the DOC is mounted on the AVUM) by 0.05%. Although, load case eight has a higher final mass than load case two, load case eight is selected as the suitable final model. The mass difference is very small, however the load case eight assures an optimized configuration for all locations. Therefore, it is feasible to have a generalized model for all six locations on the launchers. This generalized DOC still meets Requirements **Design-Space-1** to **Design-Space-5** defined in Section 1.2.

The final masses and the visual results found clear support that having a generalized model is possible, since the differences are insignificant. Producing the optimized DOC per location will cost a lot of effort while a generalized DOC will allow a mass production process. Mass production results in lower labor costs, test, and production costs. Additionally, it was concluded that the final mass results of the highest load case is not the same as the generalized model.

The main purpose of this study was to investigate the behaviour of the DOC under different load cases. It was found that the total deformation of the DOC was not that sensitive to the loads but the most delicate part was the connection between the HVI and back shell. After that, the loads applied in the y-direction were neglected because the DOC was stiffer in the y-direction. This neglection in the y-direction was found to be sensitive to the final mass result. At least, the final topology optimization mass was sensitive to the applied loads.

For the current DOC design, four locations were considered: the Ariane 5, Vega, Soyuz, and Zefiro 9. The DOC model was redesigned by adding the reduced HVI mass to the ballast. The center of gravity of the DOC will be shifted by 8.1% in the z-direction towards its nose. Therefore, the DOC is made more aerodynamically stable.

The final mass was reduced by 2.7420% compared to the initial model. Finally, it can be concluded that having a generalized DOC concept, so that it will fit on every European Space Agency (ESA) launcher and stage and meet the predefined requirements and will withstand environmental loads while general operability of the DOC is guaranteed, is indeed feasible.

10.2. Recommendation

Although this thesis contributes to the next generation of DOCs, there are numerous challenges to consider for future research. These recommendations are as follows:

- Take the loads applied in the y-direction into account;

- An additional research can be done to explore the loads on the structures come from the dynamic pressure of re-entry and associated deceleration into account. Also, the loads applied on the DOC when it crashed the Earth can explored to find out what happen to the DOC after the crash;

- The exclusion of thermal and aerodynamic disciplines were beyond the scope of this thesis. Therefore, it is recommended to check the new feasible DOC with respect to these two fields;

- Investigate the connection between the back shell and HVI, and redesign the connection between these parts. For example, add at least one more bonded connection between the HVI and back shell and analyse the model again.

Bibliography

Allaire, G., Jouve, F. and Toader, A. (2002), 'A level-set method for shape optimization', *Comptes Rendus Mathematique* **334**(1-2), 1125–1130.

ANSYS (2010), 'Ansys mechanical structural nonlinearities', *ANSYS customer training material, Lecture 3: Introduction to contact* .

ANSYS workbench user's guide (2009), Technical report, Canonsburg, PA 15317.

Arcam A2X, setting the standard for additive manufacturing (2017), `http://www.arcam.com/wp-content/uploads/arcam-a2x.pdf`. Access: 25-03-2018.

Atani, K., Makrizi, A. and Radi, B. (2016), 'Topology optimization of 3d structure using ansys and matlab', *Mathematics* **12**(6), 63–69.

Bankoti, S., Jain, N. and Misra, A. (2015), 'Topological optimization of 3d structures by optimality criteria using ansys', *Research in Emerging Science and Technology* **2**(2), 30–35.

Bendsøe, M. P. and Kikuchi, N. (1988), Generating optimal topologies in structural design using a homogenization method, *in* 'Computer Methods in Applied Mechanics and Engineering', Vol. 71, Science Direct, p. 197 – 224.

Bendsøe, M. and Sigmund, O. (2003), *Topology optimization: theory, methods and applications*, Springer.

Bendsøe, M. (1989), 'Optimal shape design as a material distribution problem', *Structural Optimization* **202**, 193–202.

Bolognese, J. and Simmons, R. (2009), *Finite element modeling continuous improvement*, NASA. Chapter: Miles' equation.

Bolton, H. P. J. (2000), The effect of global and local modes, Master's thesis, University of Pretoria. Chapter 5.

Bonnal, C., Gigou, J. and Aubin, D. (2009), 'Space debris mitigation measures applied to european launchers', *Acta Astronautica* **65**(11-12), 1679–1688.

Borrelli, R., Franchitti, S., Pirozzi, C. and Paletta, N. (2015), Mechanical and microstructural characterization of electron beam melted ti-6al-4v speimens, *in* '23rd Conference of the Italian Association of Aeronautics and Astronautics', Torino.

Campolongo, F., Cariboni, J. and Saltelli, A. (2007), 'An effective screening design for sensitivity analysis of large models', *Environmental modelling and software* **22**(10), 1509–1518.

Christensen, P. and Klarbring, A. (2009*a*), *An introduction to structural optimization*, Vol. 153, Springer, Sweden. ISBN 978-1-4020-8665-6.

Christensen, P. W. and Klarbring, A. (2009*b*), *An introduction to structural optimization*, Vol. 153, Springer, Dordrecht.

Cicalo, S., Beck, J. and Minisci, E. (2017), Benchmarking re-entry prediction uncertainties, Final Report ESA Contract No. 4000115171/15/F/MOS, ESA.

Deaton, J. D. and Grandhi, R. V. (2014), 'A survey of structural and multidisciplinary continuum topology optimization: post 2000', *Structural and Multidisciplinary Optimization* **49**, 1–38.

ESA (2017), 'New technologies space transportation', `http://www.esa.int/Our-Activities/Space-Transportation/New-Technologies/FLPP-preparing-for-Europe-s-next-generation-launcher`. Access: 01-09-2017.

ESA, E. S. A. (2018), 'Ariane 5 es', `https://www.esa.int/Our_Activities/Space_Transportation/Launch_vehicles/Ariane_5_ES`. Access: 25-08-2017.

ESA-ESTEC (2013), *ECSS-E-HB-32-26A Spacecraft mechanical loads analysis handbook*, ECSS Secretariat ESA-ESTEC.

Gardi, R., Pezzella, G., Vecchio, A. D. and Quaranta, V. (2016), 'Additive layer manufactoring for the demise observation capsule realization', *67th International Astronautical Congress* (IAC-16,C2,9,2,x35846).

Giglio, M., Manes, A. and Vigano, F. (2012), 'Ductile fracture locus of ti-6ai-4v titanium alloy', *International Journal of Mechanical Sciences* **54**(1), 121–135.

Girard, A., Imbert, J. and Moreau, D. (1989), 'Derivation of european satellite equipment test specifications from vibro-acoustic test data', *Acta Astronautica* **19**(10), 797–803.

Hammond, W. (2001), *Design methodologies for space transportation systems*, American Institute of Aeronautics and Astronautics.

Harris, T. (2015), 'Taking nastran input files into ansys mechanical via external model in ansys 16.0', `http://www.padtinc.com/blog/the-focus/taking-nastran-input-files-into-ansys-mechanical-via-external-model-in-ansys-16-0`. Access: 06-08-2017.

Heinrich, S., Leglise, F., Harrison, L. and F. Renard, O. N. (2015), Trade-off atmospheric re-entry: design for demise vs cntrolled re-entry, *in* T. Sgobba and I. Rongier, eds, 'Space safety is no accident', Springer, Cham, pp. 423–435.

Hollauer, C. (2007), Modeling of thermal oxidation and stress effects, PhD thesis, Wien university of technology, Osterreich.

Kasper, J., Behar-Lafenetre, S., G., G. L., Laine, B. and Thamm, H. (1989), 'Derivation of satellite equipment design and test specifications from random vibration environments', *Spacecraft Structures, Material en Mechanical Testing* **19**(10), 797–803.

Lagier, R. (2016), Ariane 5 user's manual, Technical report, Issued and approved by Arianespace.

Lammens, S., van der Linden, S., Watts, T., Visser, L., Maraffa, L. and Dussy, S. (2018), A black box for launchers - the demise observation capsule, Technical report, Science and Technology. NVR Ruimtevaart 2018-1.

Ley, W., Wittmann, K. and Hallmann, W. (2009), *Handbook of space technology*, John Wiley and Sons, UK.

Miles, J. (1954), 'On structural fatigue under random loading', *Aeronautical Sciences* p. 753.

Miller, E. (2010*a*), 'Finite element modeler part 1: Translating meshes with ansys fe modeler', `http://www.padtinc.com/blog/the-focus/fe-modeler-part-1-translating-meshes-with-ansys-fe-modeler`. Access: 06-01-2018.

Miller, E. (2010*b*), 'Harwin connector catalog', `http://www.farnell.com/datasheets/1704512.pdf_ga=2.62957351.904266505.1523538395-31402060.1523538395`. Access: 12-04-2018.

Mlejnek, H. P. (1992), 'Some aspects of the genesis of structures', *Structural Optimization* **5**, 64–69.

Morgan, R. G. and Stewart, B. S. (1998), The aerodynamic stability of superorbital re-entry craft, *in* '13th Australasian fluid mechanics conference', pp. 571–574.

Mulder, J., Staveren, W., van der Vaart, J. and de Weerdt, E. (2013), *Flight dynamics lecture notes*, Addison-Wesley, Delft University of Technology.

Muylaert, J., Kordulla, W., Giodano, D., Marraffa, L. and Schawane, R. (2001), Aerothermodynamic analysis of space vehicle phanomena, Technical report, European Space Egency, ESA Directorate of Technical and Operational Support, ESTEC, Noordwijk, The Netherlands.

Osher, S. and Sethian, J. (1988), 'Front propagating with curvature dependent speed: algorithms based on hamilton-jacobi formulations', *Computational Physics* **79**, 12–49.

Perez, E. (2012), Soyuz user's manual, Technical report, Issued and approved by Arianespace.

Perez, E. (2014), Vega user's manual, Technical report, Issued and approved by Arianespace.

Popov, V. L. (2010), *Contact mechanics and friction, physical principles and applications*, first edn, Springer.

Roy (2013), *Additive manufacturing: opportunities and constraints.* ISBN: 978-1-909327-05-4.

Saltelli, A., Tarantola, S., Campolongo, F. and Ratto, M. (2004), *Sensitivity analysis in practice: A guide to assessing scientific models*, John Wiley and Sons. ISBN:9780470870952.

Schaefer, E. (1997), Evaluating the vibro-acoustic response of honeycomb panels, *in* J. Stecher, ed., '19th, Space simulation conference: Cost effective testing for the 21st Century', Vol. 3341, National Aeronautics and Space Administration, NASA CP 3341, pp. 195–204.

Science and Technology (2017), Demise observation capsule (doc) for re-entry science and safety, Technical report, Science and Technology.

Shenyan, C., Yanwu, Z. and Yanjie, L. (2018), 'Structural optimization with an automatic mode identification method for tracking the local vibration mode', *Engineering optimization* **1**.

Sigmund, O. and Maute, K. (2013), 'Topology optimization approaches: A comparative review', *Structural and Multidisciplinary Optimization* **48**(6), 1031–1055.

Simon, H. L. (2010), Technical data: Proper bolt axial tightening force and proper tightening torque, Technical report, Misumi USA.

Spann, F. and Patt, P. (1984), 'Component vibration environment predictor', *Environmental Sciences* **27**(5), 19–24.

Suresh, B. and Sivan, K. (2015), *Integrated design for space transportation system*, Springer, India.

Varnes, D. J. (1962), 'Analysis of plastic deformation according to von mises' theory', **57**(378).

Wang, M., Wang, X. and Guo, D. (2003), 'A level set method for structural topology optimization', *Computer Methods in Applied Mechanics and Engineering* **192**(1-2), 227–246.

Wertz, J. and Larson, W., eds (1999), *Space mission analysis and design*, third edn, Microcos Press.

Wijker, J. (2008), *Spacecraft structures*, Springer, Dutch Space BV, NL-2303 DB Leiden, The Netherlands. ISBN 978-3-540-75552-4.

Wijker, J. (2009), *Random vibrations in spacecraft structures design, theory and applications*, Vol. 165, Springer, Dutch Space BV.

Xie, Y. M. and Steven, G. P. (1993), 'A simple evolutionary procedure for structural optimization', *Computers and structures* **49**(5), 885–896.

Zhou, M. and Rozvany, G. (1991), 'The coc algorithm, part ii: topological, geometry and generalized shape optimization', *Computer Methods in Applied Mechanics and Engineering* **89**(1–3), 309–336.

A
Appendix

A.1. Overview of Future Missions

In this section, an overview of future missions of ESA conducted during the literature study is presented in Table A.1.[1 2 3 4 5 6 7 8 9 10 11]

Table A.1: Overview of ESA Missions (ESA, 2017)

Mission	Launch Date	Launch Vehicle	Purpose	Description
Aeolus	2018	Vega	Mapping Earth's global wind fields	Altitude: 320 km; Inclination: 97°
BepiColombo	2018	Ariane 5	Planetary science	Europe's first mission to the Mercury
Cheops	2018	Soyuz	Studying the exoplanets	Altitude: 800 km; Sun-synchronous
Earthcare	2019	Soyuz	Studying the roles of clouds and aerosols in climate change	Altitude: 393.14 km; Inclination: 97.05° ; Sun-synchronous
Biomass	2020	Vega	Measuring forest biomass	Altitude: ~ 660 km ; Orbit: Sun-synchronous
Euclid	2020	Soyuz ST 2-1b	Map the geometry of the dark universe	Halo orbit around the second Sun-Earth Lagrange point, L2
Smile	2021	Soyuz including Fregat, back-up Vega	Measuring Earth's global system responses to solar wind and geomagnetic variations	A highly inclined, elliptical orbit; Molniya orbit; Prigee altitude:12742 km; Apogee altitude: 127420; Inclination: 63.4°
MetOp-SG-A	2021	Soyuz/ST including Fregat	To provide operational observations and measurements from polar orbit for numerical weather prediction	Altitude: 831 km; Polar orbit
MetOp-SG-B	2022	Soyuz/ST including Fregat	To provide operational observations and measurements from polar orbit for numerical weather prediction	Altitude: 831 km; Polar orbit
Flex	2022	Vega	Map global vegetation health	Altitude: 815 km; Orbit: Sun-synchronous
Juice	2022	Ariane 5 ECA	Planetary science	Exploring the Jupiter system
Plato	2024	Soyuz/ST including Fregat	Discover extra solar planetary systems and terrestrial planets	Rocket for injection into a Lissajous orbit around the Sun-Earth Lagrangian point, L2

---

[1] ESA, Aeolus http://www.esa.int/Our-Activities/Observing-the-Earth/Aeolus/Introducing-Aeolus, Date of used:[Augustus 20, 2018]

[2] ESA, BepiColombo ,http://sci.esa.int/bepicolombo/, Date of used: [Augustus 20, 2018]

[3] ESA, Cheops, http://sci.esa.int/cheops/, Date of used:[Augustus 20, 2018]

[4] ESA, Earthcare, https://earth.esa.int/web/guest/missions/esa-future-missions/earthcare, Date of used: [Augustus 20, 2018]

[5] ESA, Biomass,https://earth.esa.int/web/guest/missions/esa-future-missions/biomass, Date of used:[Augustus 20, 2018]

[6] ESA, Euclid,http://sci.esa.int/euclid/, Date of used: [Augustus 20, 2018]

[7] ESA, Smile, http://sci.esa.int/smile/59312-science-with-smile/, Date of used:[Augustus 20, 2018]

[8] ESA, MetOp-SG ,https://directory.eoportal.org/web/eoportal/satellite-missions/m/metop-sg, Date of used:[Augustus 20, 2018]

[9] ESA, Flex, http://www.esa.int/Our-Activities/Observing-the-Earth/New-satellite-to-measure-plant-health, Date of used:[Augustus 20, 2018]

[10] ESA, Juice, http://sci.esa.int/juice/, Date of used:[Augustus 20, 2018]

[11] ESA, Plato,http://sci.esa.int/plato/, Date of used:[Augustus 20, 2018]

A.2. Reference Frames

The position and the orientation (velocity and acceleration) of the DOC needs be identified with respect to a reference frame. It is presented by three orthogonal axis through the origin of this reference frame. Here, all reference frames are following the right-handed rule. In this section, first the definition of reference frames will be defined using the theory propounded in (Mulder et al., 2013).

Earth-Centered Inertial Reference Frame, Index F_I:

The Earth-Centered Inertial reference frame (ECI) is a Earth-fixed non-rotating frame, which is fixed in time and represents a unique standard for all bodies in the system. This reference frame is required to express the launcher/stage's position and velocity in the ascent phase. This reference frame is used by the launcher authorities to present the results in Section 2.1. This reference frame is shown in Figure A.1 and is as follows:

- The origin is at the center of mass of the Earth;

- The Z_I-axis is pointed to the north through the pole of the Earth;

- The X_I-axis goes through the equator towards the vernal equinox;

- The Y_I-axis passes through the equatorial plane and is perpendicular to X_I- and Z_I-axis.

Geometric Reference Frame, Index F_g:

The geometric reference frame is located at a particular point on the structures of the spacecraft; it is following the right-handed rule with an arbitrary pointing direction. This reference frame can be used to present the relative position of the subsystems or forces to the center of mass. The direction of the axes are arbitrary and can be selected in such way that it is convenient to describe the relative position of forces or points on the body.

Launcher and Stage Geometric Reference Frame

Geometric reference frame will be apply on the launcher as well as on the host vehicle, where DOC is embarked on. Launcher geometric reference frame is fixed to the launcher and its characteristics are:

- The origin is located at the bottom of the launcher and on the center of symmetrical line of cross section;

- The X_b-axis is pointing forward along the symmetry line;

- The Y_b-axis is directed to the right;

- The Z_b-axis is pointing to complete the reference frame.

The same manner is applicable to the host vehicle. Figure A.2 indicates the geometric reference frame on the Vega launcher.
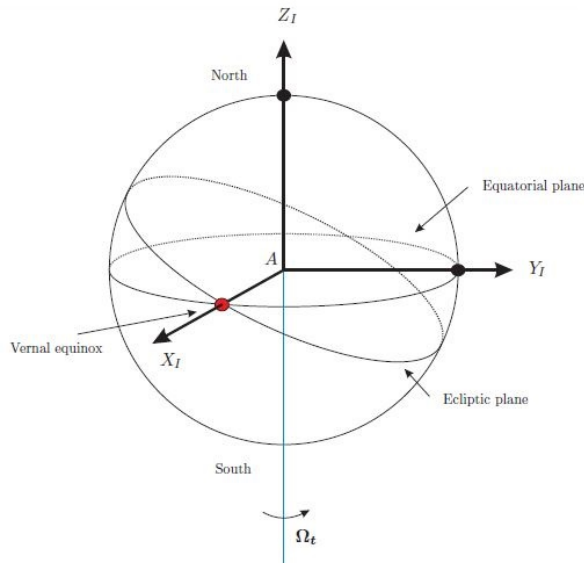
Figure A.1: Earth-Centered Inertial Reference Frame (Mulder et al., 2013)
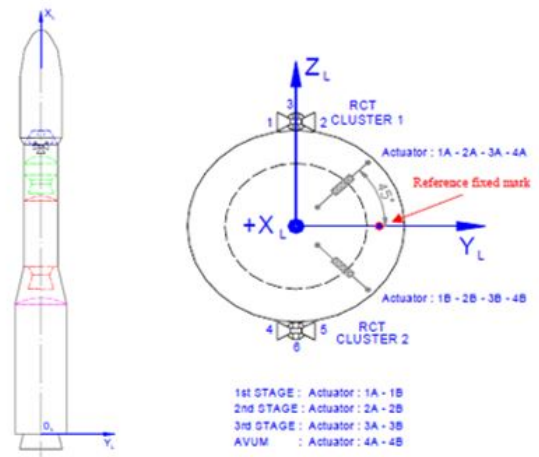
Figure A.2: Launcher Geometric Reference Frame (S[&]T Internal Report)

A.3. Connection

The external connections are modelled as fixed support and are shown in Figure A.3.
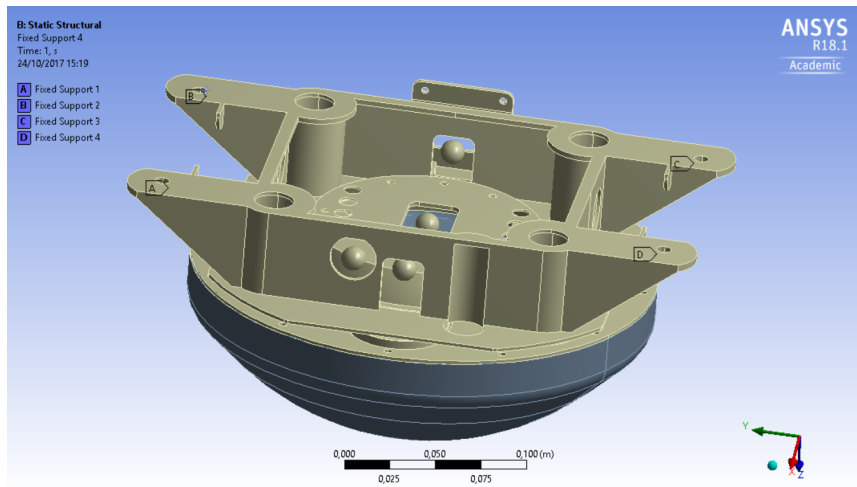
Figure A.3: Fixed Support of the External Constraint

A.4. Mesh Convergence Analysis

In this section, the additional results of the mesh convergence analysis are illustrated. Here, deformation results of mesh convergence analysis of static analysis of Ariane 5 is presented in Table A.2 and only the plots of the mesh convergence analysis of Vega, Zefiro 9 and Soyuz are shown. Since the results show the same conclusion, the last two locations simulations have not been conducted.

Table A.2: Deformation Results of Mesh Convergence Analysis of Static Analysis of Ariane 5

Mesh Size [mm]	Element Number	Deflection [mm]		
		-x Acceleration	x Acceleration	z Acceleration
10	28164	1.5286	0.8530	0.6145
5	82636	1.7067	0.92727	0.7141
4	130692	1.7352	0.94774	0.7275
3	235454	1.7482	0.96984	0.7412
2	667882	1.7622	0.97894	0.7574

Figure A.4: Mesh Convergence Analysis of Vega in Static Analysis   Figure A.5: Mesh Convergence Analysis of Zefiro 9 in Static Analysis

Figure A.6: Mesh Convergence Analysis of Soyuz in Static Analysis

A.5. Set Up of Numerical Analysis
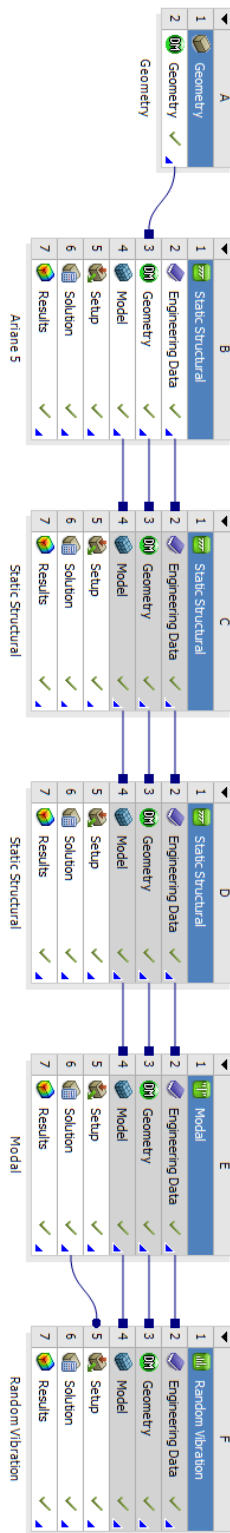
Figure A.7: Numerical Set Up of Analysis of Ariane 5

A.6. Static Analysis

The stress and deformation results of static analysis are illustrated here.

A.6.1. Ariane 5
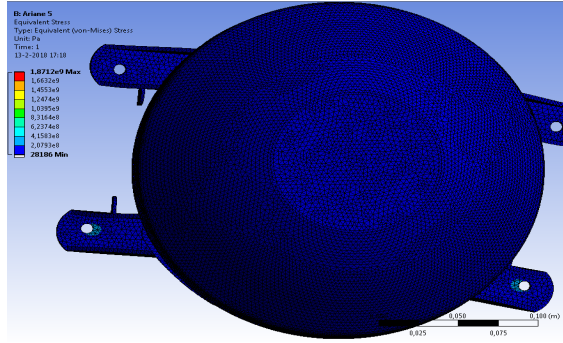
Figure A.8: Stress Due to Ariane 5, Acceleration -x = 1008 m/s^2
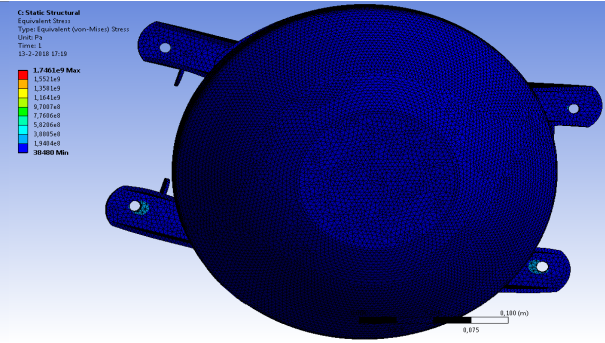
Figure A.9: Stress Due to Ariane 5, Acceleration x = 1008 m/s^2
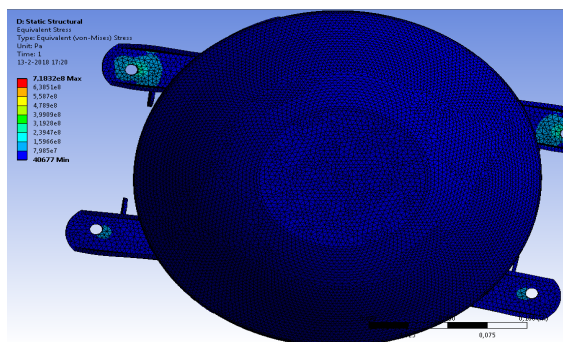
Figure A.10: Stress Due to Ariane 5, Acceleration z = 1008 m/s^2
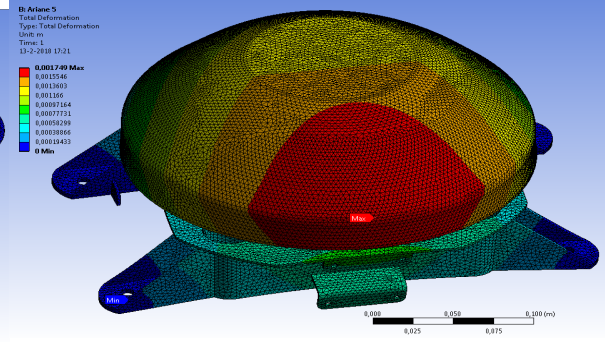
Figure A.11: Deformation Due to Ariane 5, Acceleration -x = 1008 m/s^2
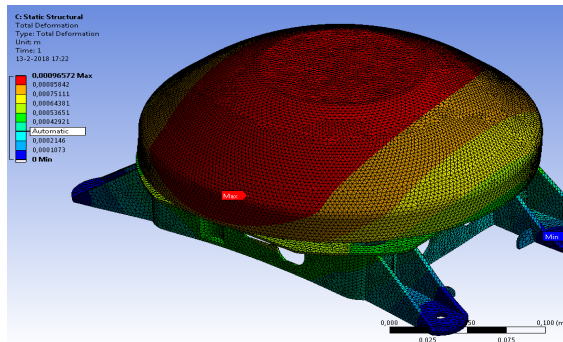
Figure A.12: Deformation Due to Ariane 5, Acceleration x = 1008 m/s^2
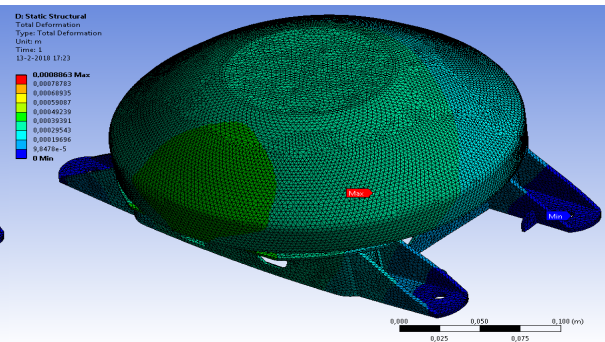
Figure A.13: Deformation Due to Ariane 5, Acceleration z = 1008 m/s^2

A.6.2. AVUM
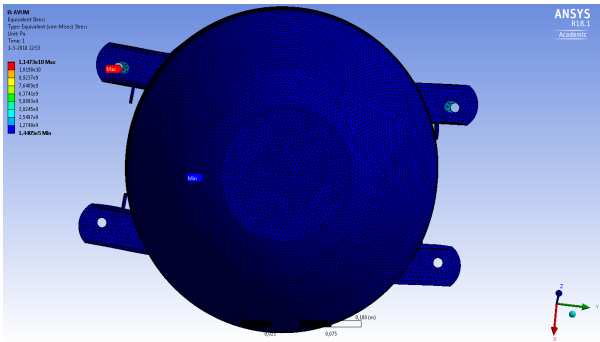
Figure A.14: Stress Due to AVUM, Acceleration -x = 6226.9 m/s^2
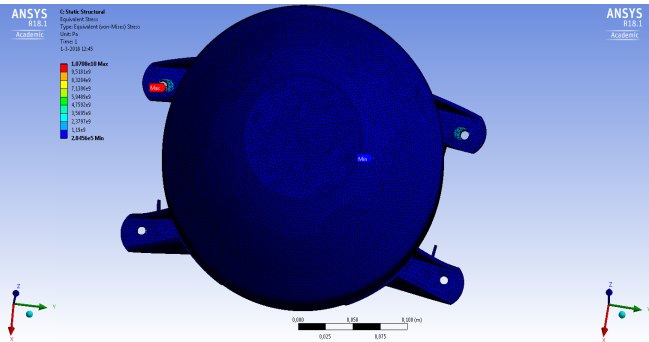
Figure A.15: Stress Due to AVUM, Acceleration x = 6226.9 m/s^2
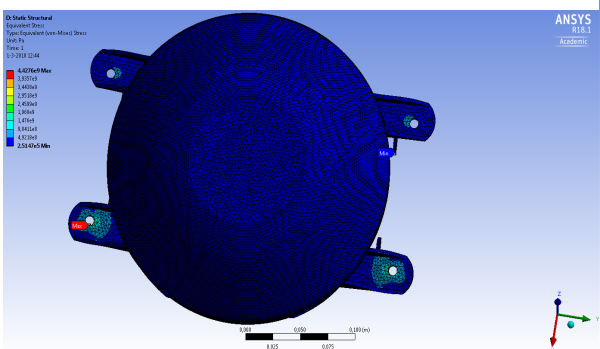
Figure A.16: Stress Due to AVUM, Acceleration z = 6226.9 m/s^2
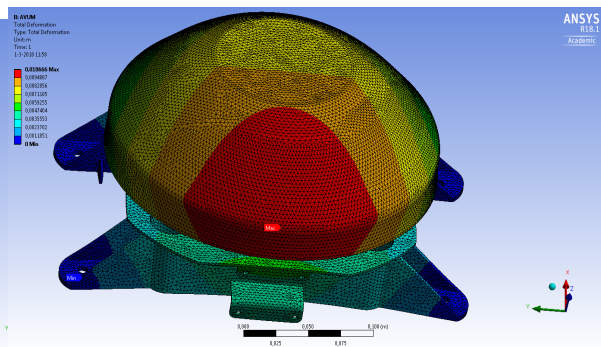
Figure A.17: Deformation Due to AVUM, Acceleration -x = 6226.9 m/s^2
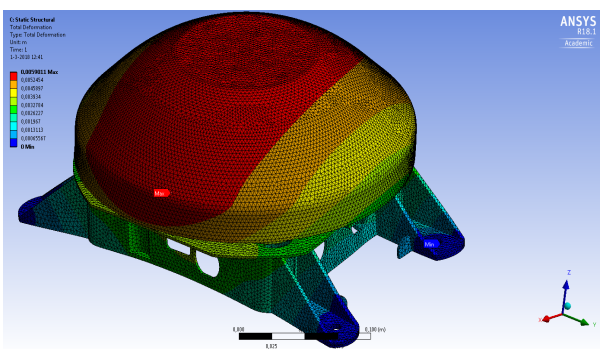
Figure A.18: Deformation Due to AVUM, Acceleration x = 6226.9 m/s^2
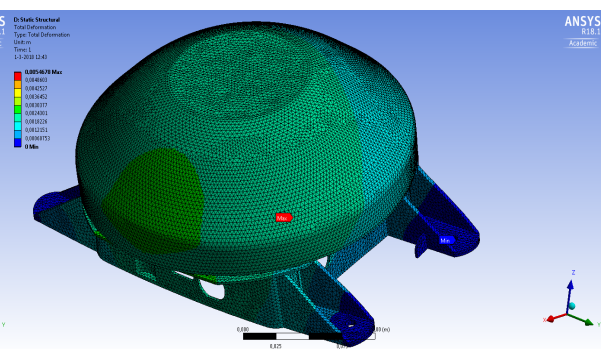
Figure A.19: Deformation Due to AVUM, Acceleration z = 6226.9 m/s^2

A.6.3. Vega PLA
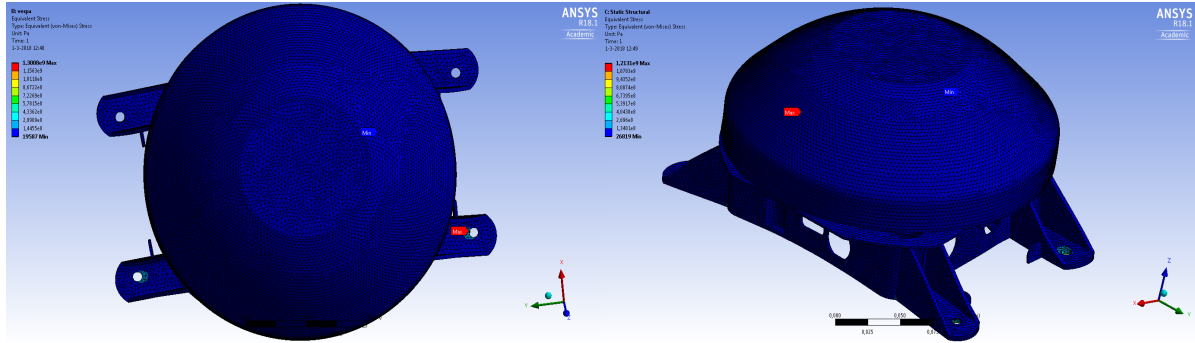
Figure A.20: Stress Due to Vega (PLA), Acceleration -x = 700 m/s^2

Figure A.21: Stress Due to Vega (PLA), Acceleration x = 700 m/s^2
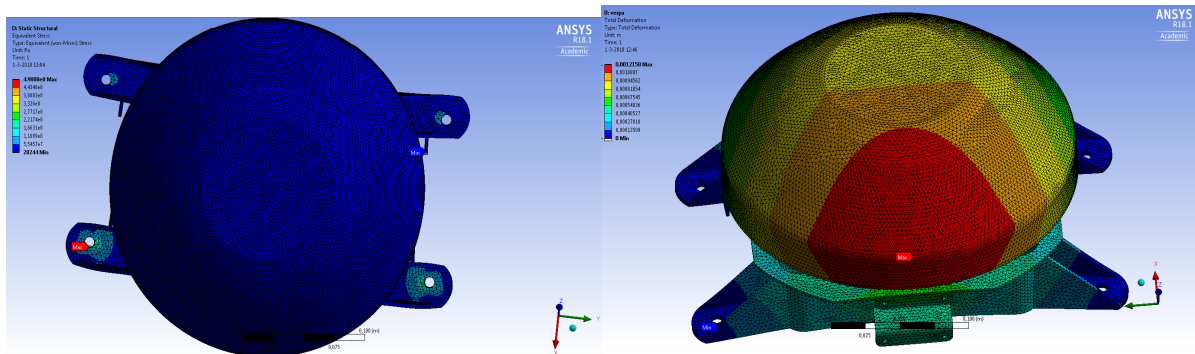
Figure A.22: Stress Due to Vega (PLA) , Acceleration z = 700 m/s^2

Figure A.23: Deformation Due to Vega (PLA), Acceleration -x = 700 m/s^2
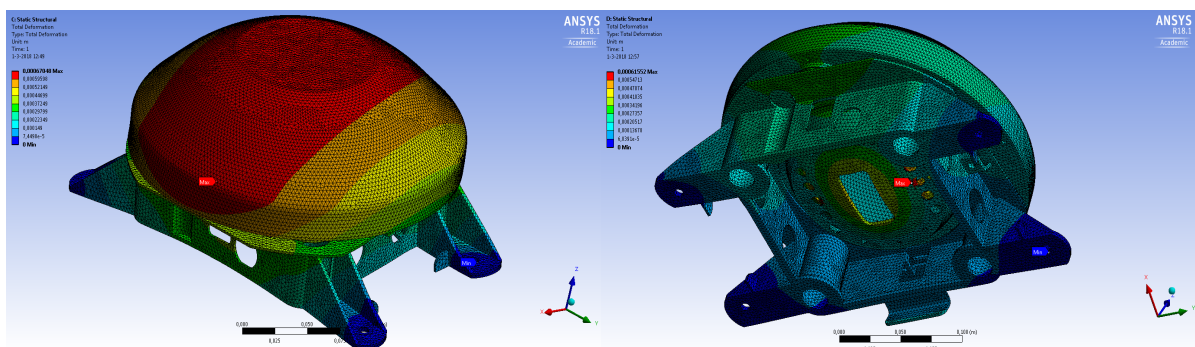
Figure A.24: Deformation Due to Vega (PLA), Acceleration x = 700 m/s^2

Figure A.25: Deformation Due to Vega (PLA), Acceleration z = 700 m/s^2

A.6.4. VESPA
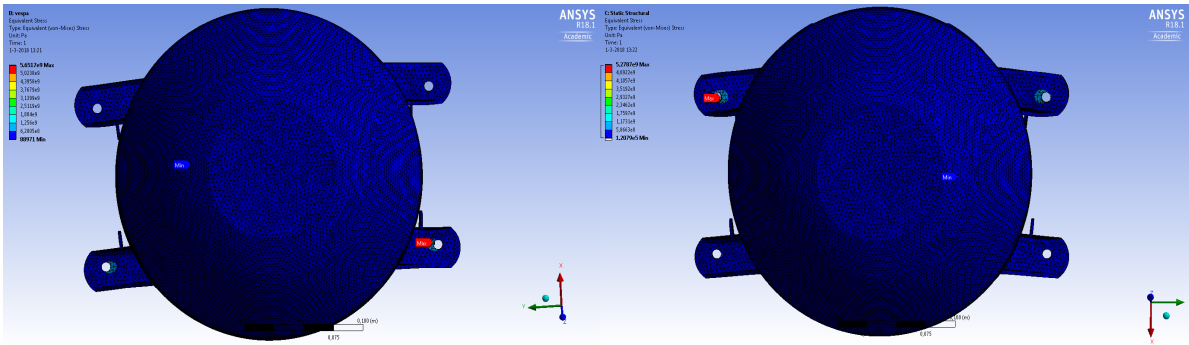
Figure A.26: Stress Due to VESPA, Acceleration -x = 3058.9 m/s^2

Figure A.27: Stress Due to VESPA, Acceleration x = 3058.9 m/s^2
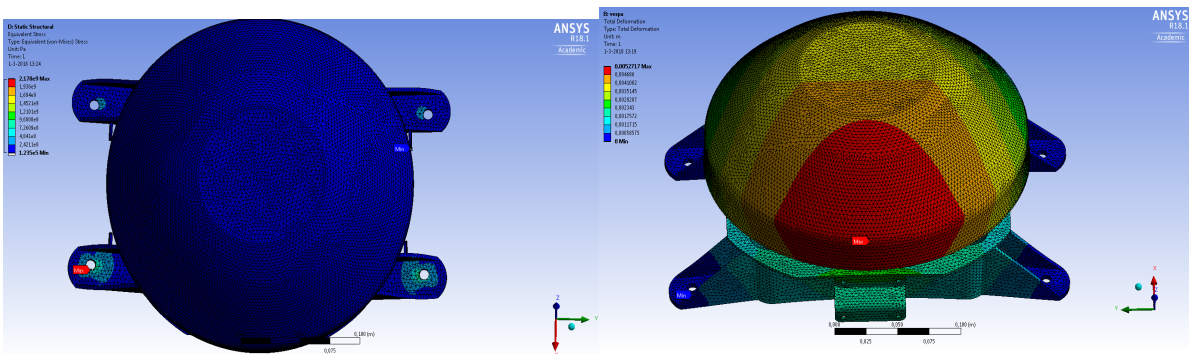
Figure A.28: Stress Due to VESPA, Acceleration z = 3058.9 m/s^2

Figure A.29: Deformation Due to VESPA, Acceleration -x = 3058.9 m/s^2
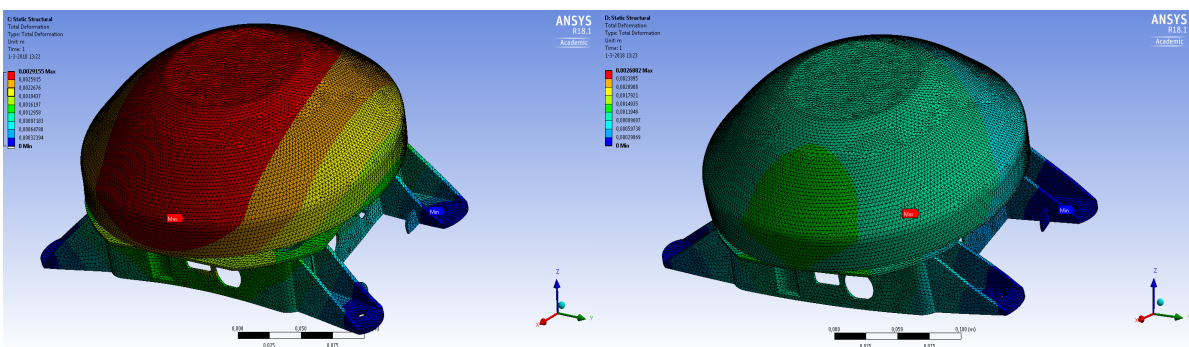
Figure A.30: Deformation Due to VESPA, Acceleration x = 3058.9 m/s^2

Figure A.31: Deformation Due to VESPA, Acceleration z = 3058.9 m/s^2

A.6.5. Zefiro 9
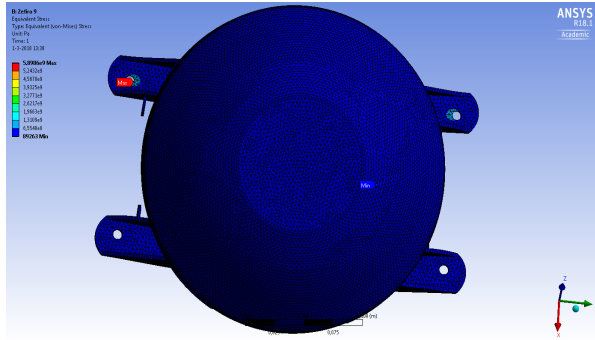
Figure A.32: Stress Due to Zefiro 9, Acceleration -x = 3193.1 m/s^2
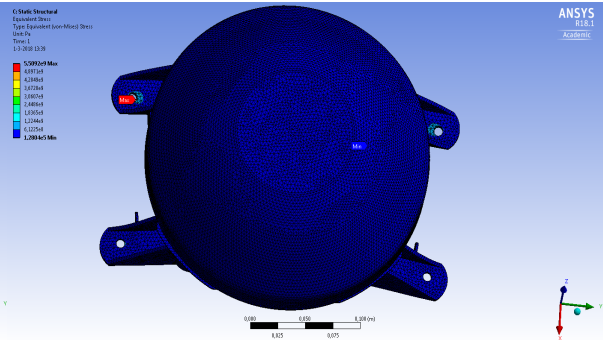
Figure A.33: Stress Due to Zefiro 9, Acceleration x = 3193.1 m/s^2
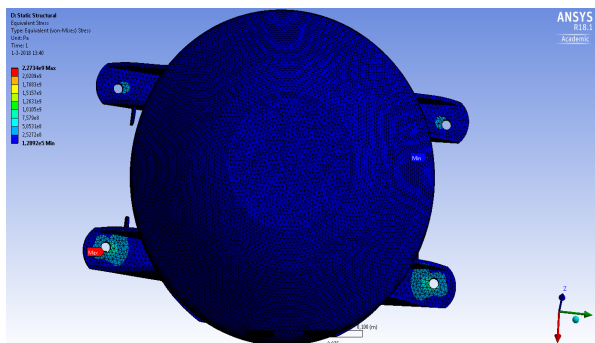
Figure A.34: Stress Due to Zefiro 9, Acceleration z = 3193.1 m/s^2
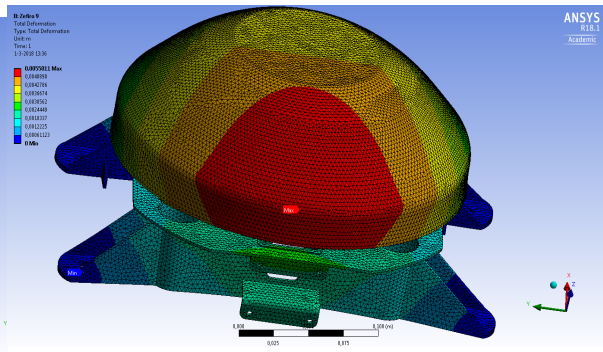
Figure A.35: Deformation Due to Zefiro 9, Acceleration -x = 3193.1 m/s^2
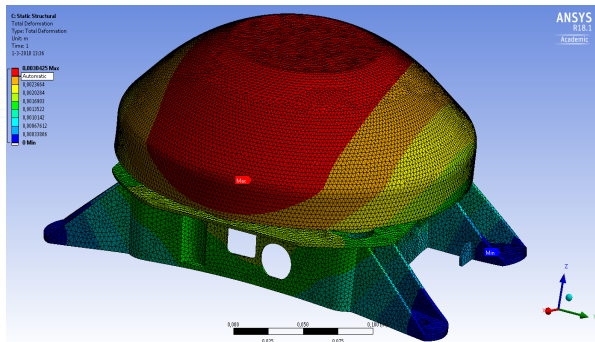
Figure A.36: Deformation Due to Zefiro 9, Acceleration x = 3193.1 m/s^2
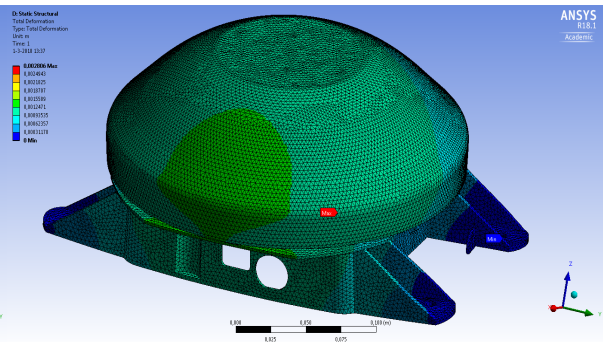
Figure A.37: Deformation Due to Zefiro 9, Acceleration z = 3193.1 m/s^2

A.6.6. Soyuz
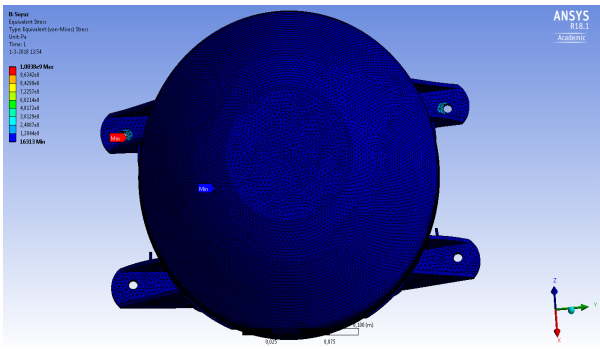
Figure A.38: Stress Due to Soyuz, Acceleration -x = 583 m/s^2
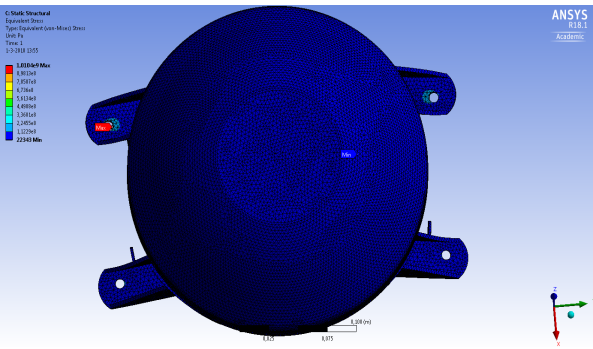
Figure A.39: Stress Due to Soyuz, Acceleration x = 583 m/s^2
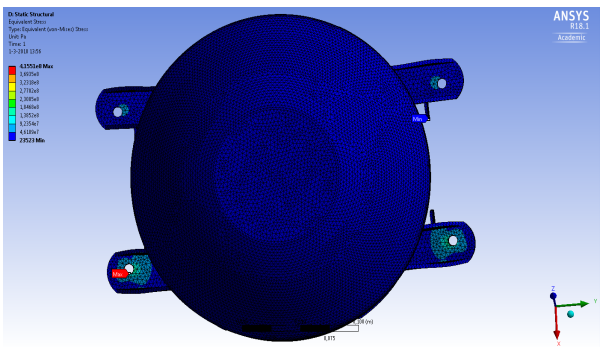
Figure A.40: Stress Due to Soyuz, Acceleration z = 583 m/s^2
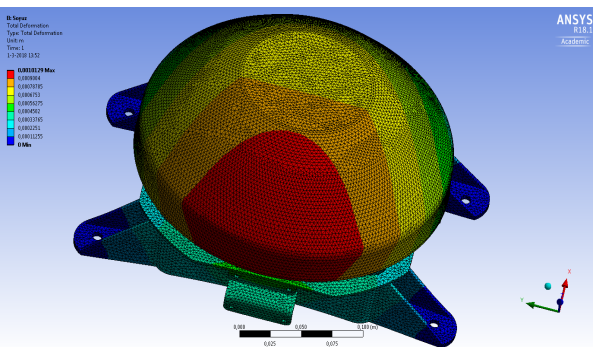
Figure A.41: Deformation Due to Soyuz, Acceleration -x = 583 m/s^2
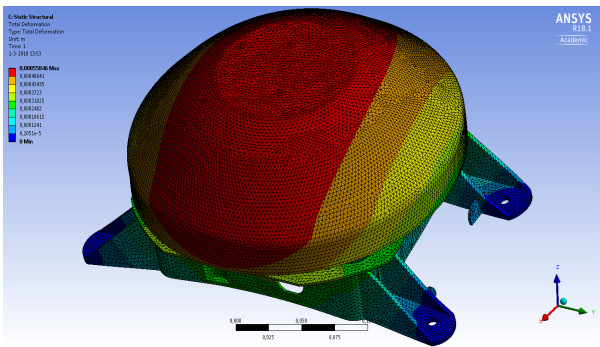
Figure A.42: Deformation Due to Soyuz, Acceleration x = 583 m/s^2
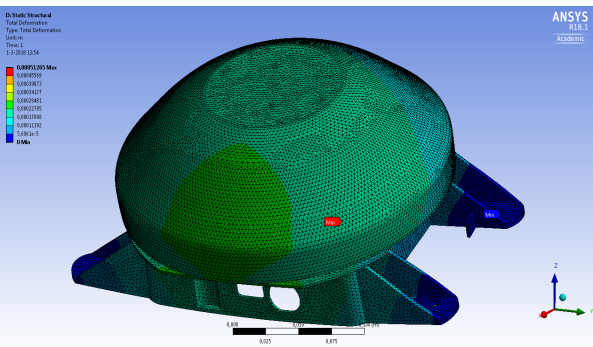
Figure A.43: Deformation Due to Soyuz, Acceleration z = 583 m/s^2

A.7. Random Vibration Analysis

The 1-σ and 3-σ stress distribution results of random vibration analysis are illustrated here.

A.7.1. Ariane 5
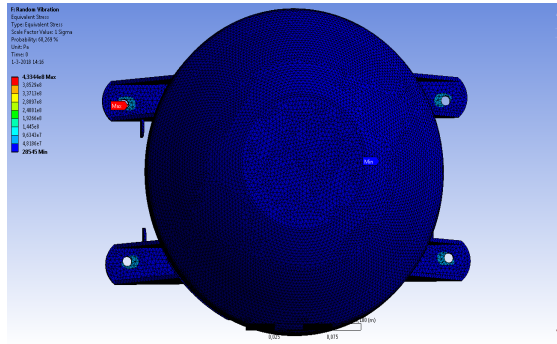
Figure A.44: The 1-σ Stress Distribution Results of Random Vibration Analysis
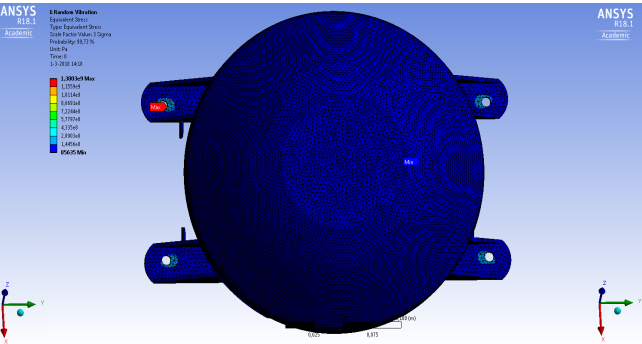
Figure A.45: The 3-σ Stress Distribution Results of Random Vibration Analysis

A.7.2. AVUM
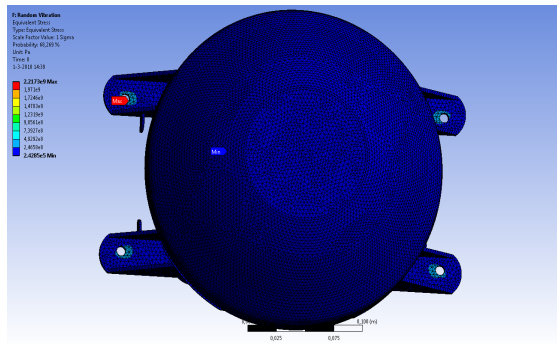
Figure A.46: The 1-σ Stress Distribution Results of Random Vibration Analysis
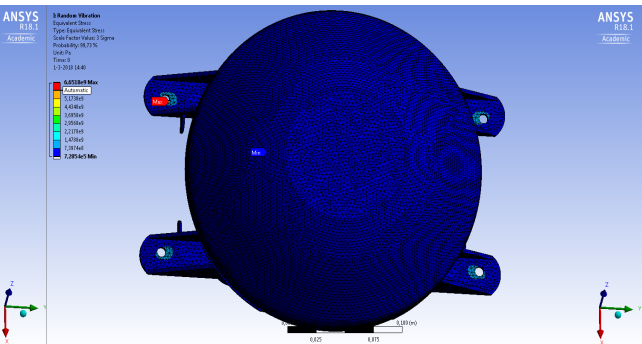
Figure A.47: The 3-σ Stress Distribution Results of Random Vibration Analysis

A.7.3. Vega
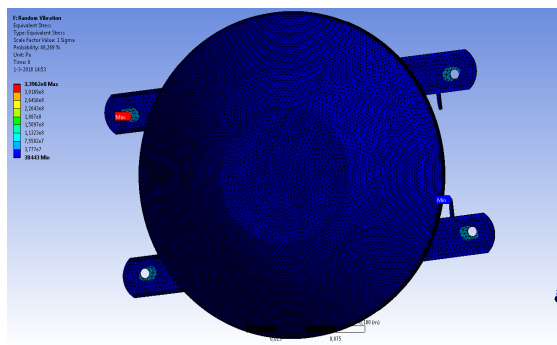
Figure A.48: The 1-σ Stress Distribution Results of Random Vibration Analysis
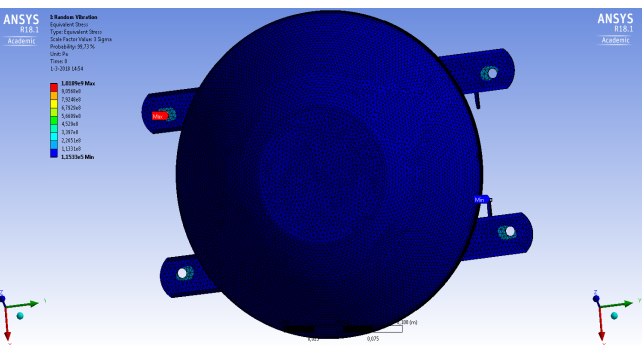
Figure A.49: The 3-σ Stress Distribution Results of Random Vibration Analysis

A.7.4. VESPA
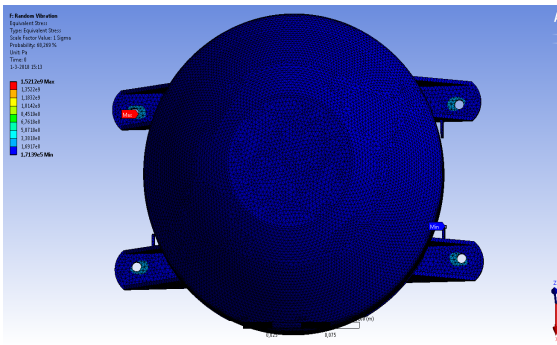
Figure A.50: The 1-σ Stress Distribution Results of Random Vibration Analysis
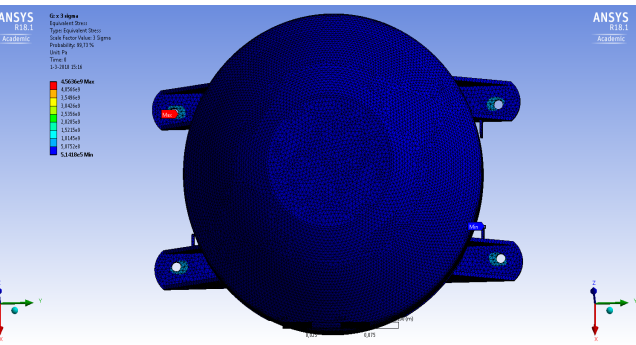
Figure A.51: The 3-σ Stress Distribution Results of Random Vibration Analysis

A.7.5. Zefiro 9
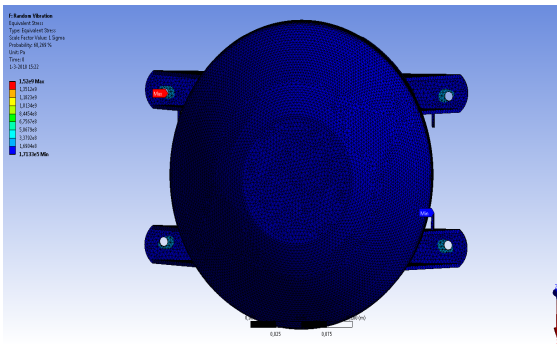
Figure A.52: The 1-σ Stress Distribution Results of Random Vibration Analysis
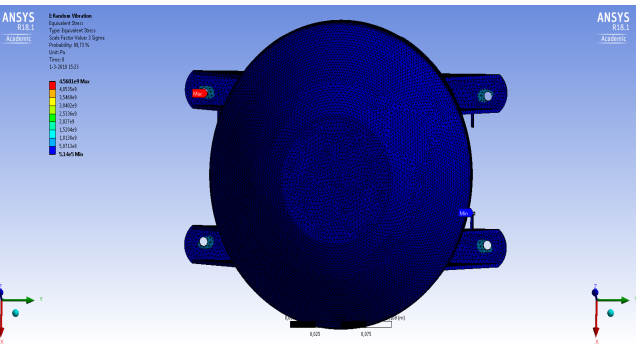
Figure A.53: The 3-σ Stress Distribution Results of Random Vibration Analysis

A.7.6. Soyuz
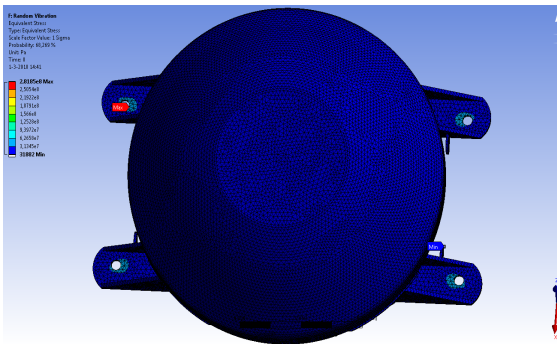
Figure A.54: The 1-σ Stress Distribution Results of Random Vibration Analysis
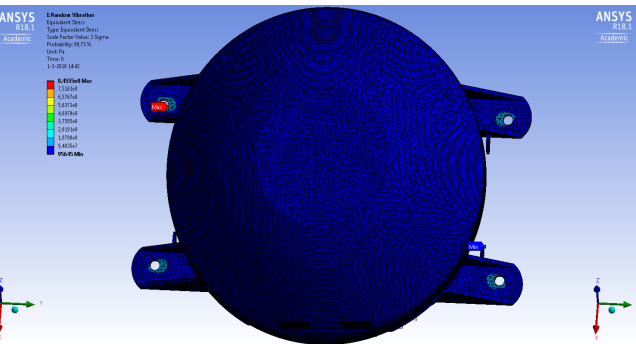
Figure A.55: The 3-σ Stress Distribution Results of Random Vibration Analysis

A.8. Set Up of Topology Optimization
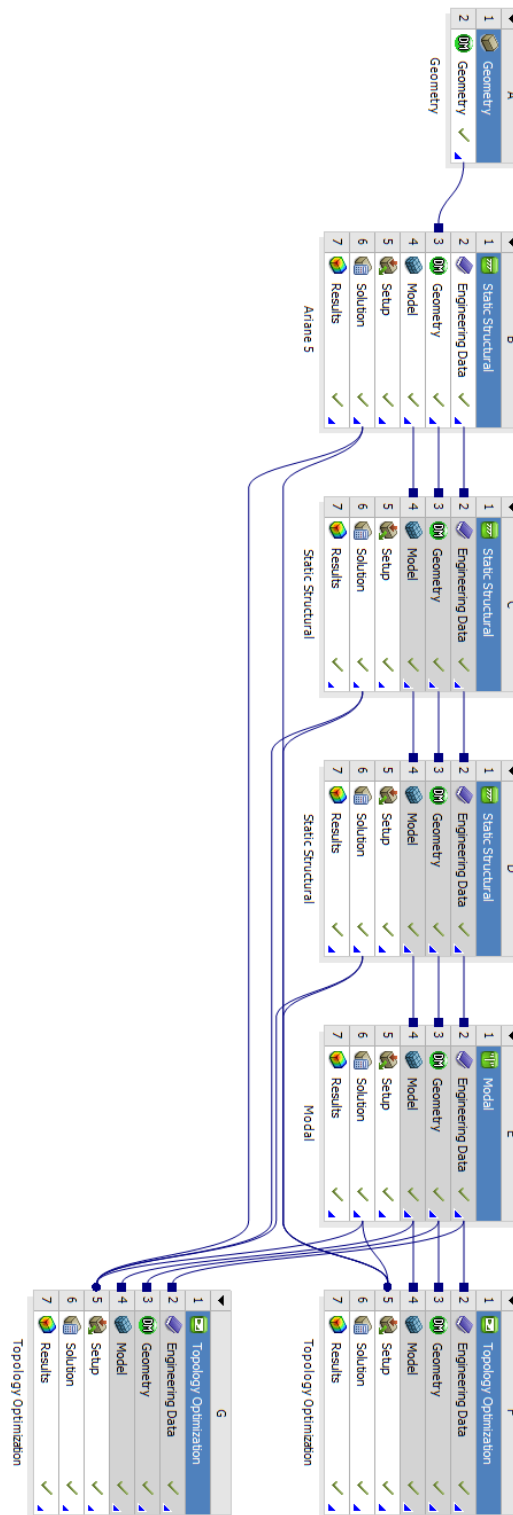
Figure A.56: Numerical Set Up of Optimization of Ariane 5

A.9. Topology Optimization Results
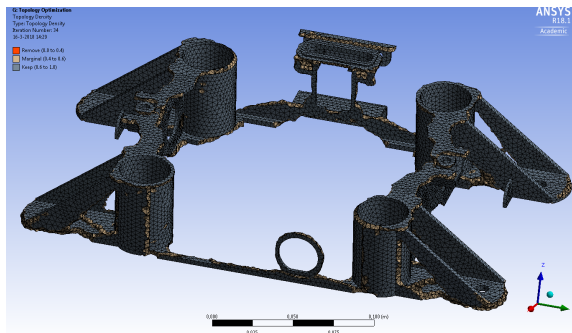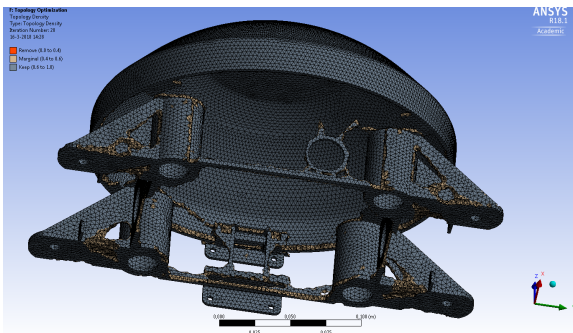
Figure A.57: Topology Optimization Results of Ariane 5, the HVI and the FS as *Design* Region

Figure A.58: Topology Optimization Results of Ariane 5, the HVI as *Design* Region
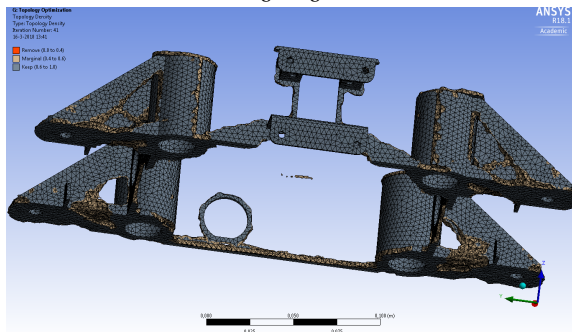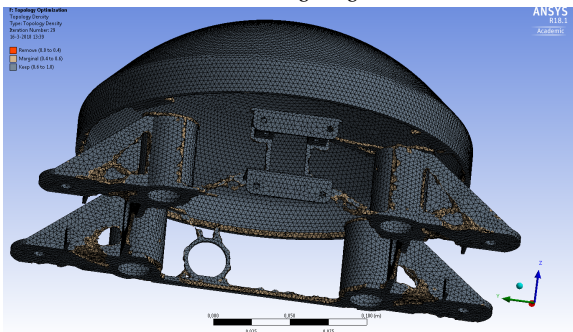
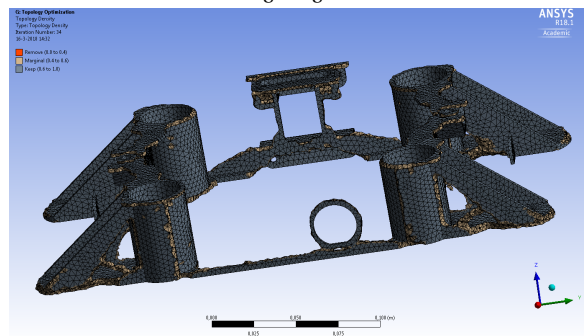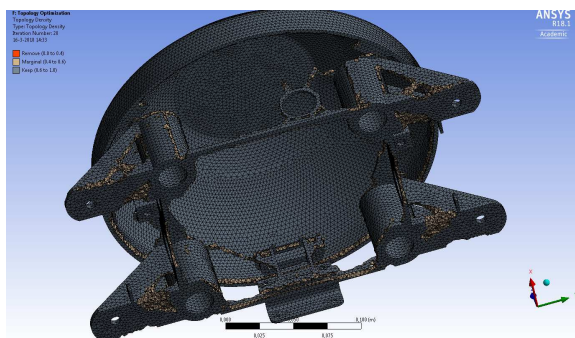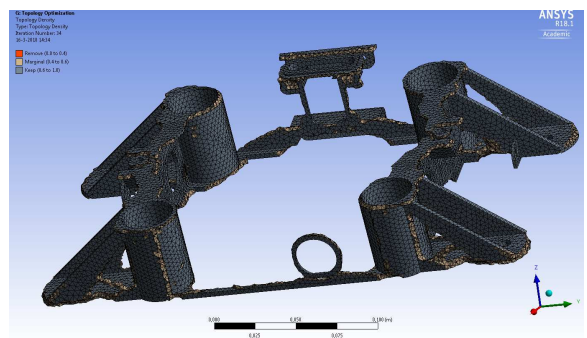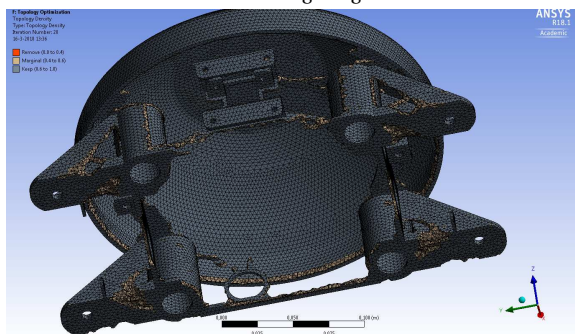Figure A.59: Topology Optimization Results of AVUM, the HVI and the FS as *Design* Region

Figure A.60: Topology Optimization Results of AVUM, the HVI as *Design* Region
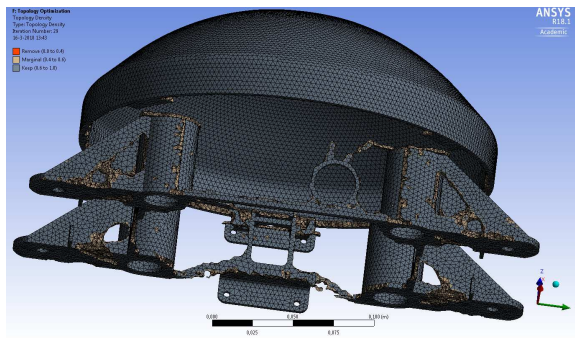
Figure A.61: Topology Optimization Results of Vega, the HVI and the FS as *Design* Region
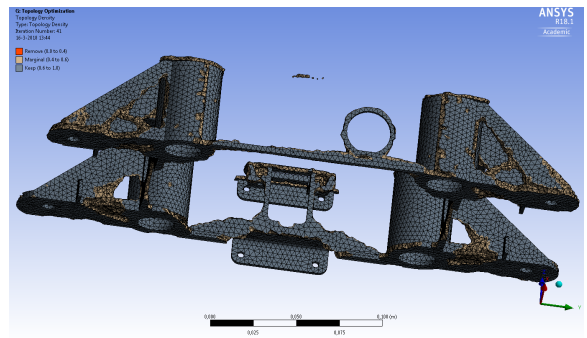
Figure A.62: Topology Optimization Results of Vega, the HVI as *Design* Region
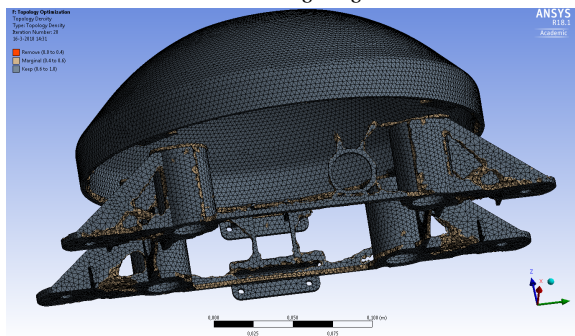
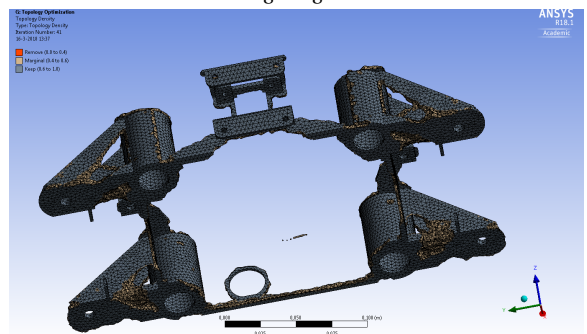Figure A.63: Topology Optimization Results of VESPA, the HVI and the FS as *Design* Region

Figure A.64: Topology Optimization Results of VESPA, the HVI as *Design* Region

Figure A.65: Topology Optimization Results of Zefiro 9, the HVI and the FS as *Design* Region

Figure A.66: Topology Optimization Results of Zefiro 9, the HVI as *Design* Region

Figure A.67: Topology Optimization Results of Soyuz, the HVI and the FS as *Design* Region

Figure A.68: Topology Optimization Results of Soyuz, the HVI as *Design* Region
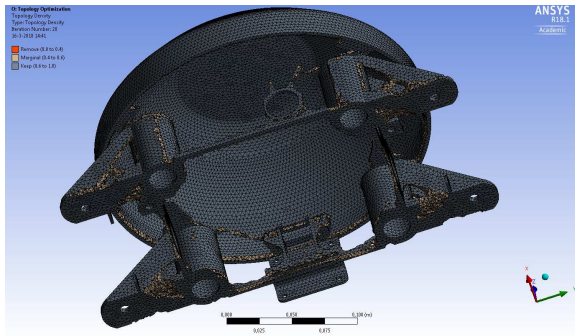
Figure A.69: Topology Optimization Results of the Current DOC Load Case, the HVI and the FS as *Design* Region
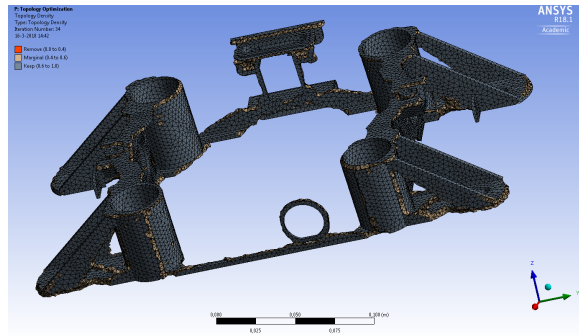

Figure A.70: Topology Optimization Results of the Current DOC Load Case, the HVI as *Design* Region
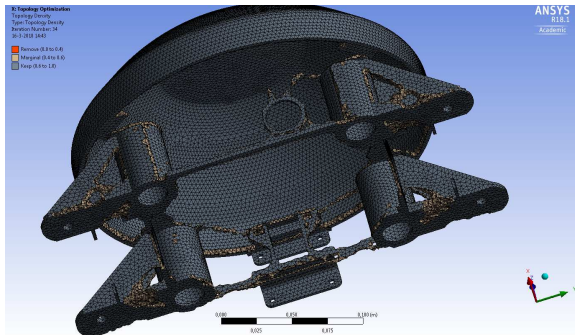

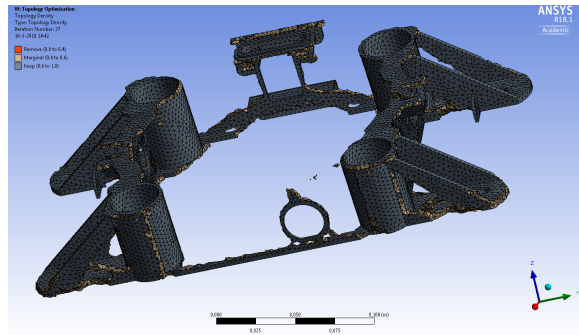Figure A.71: Topology Optimization Results of All Locations, the HVI and the FS as *Design* Region

Figure A.72: Topology Optimization Results of All Locations, the HVI and the FS as *Design* Region